2020

EFFECTS OF WATERSHED DISTURBANCES AND RIVER-TRIBUTARY CONFLUENCES ON SEDIMENTATION DYNAMICS IN THE UPPER OHIO RIVER BASIN

Ciara Pickering
University of Kentucky, cepi229@uky.edu
Author ORCID Identifier:
https://orcid.org/0000-0002-8855-7799
Digital Object Identifier: https://doi.org/10.13023/etd.2020.360

STUDENT AGREEMENT:

I represent that my thesis or dissertation and abstract are my original work. Proper attribution has been given to all outside sources. I understand that I am solely responsible for obtaining any needed copyright permissions. I have obtained needed written permission statement(s) from the owner(s) of each third-party copyrighted matter to be included in my work, allowing electronic distribution (if such use is not permitted by the fair use doctrine) which will be submitted to UKnowledge as Additional File.

I hereby grant to The University of Kentucky and its agents the irrevocable, non-exclusive, and royalty-free license to archive and make accessible my work in whole or in part in all forms of media, now or hereafter known. I agree that the document mentioned above may be made available immediately for worldwide access unless an embargo applies.

I retain all other ownership rights to the copyright of my work. I also retain the right to use in future works (such as articles or books) all or part of my work. I understand that I am free to register the copyright to my work.

REVIEW, APPROVAL AND ACCEPTANCE

The document mentioned above has been reviewed and accepted by the student's advisor, on behalf of the advisory committee, and by the Director of Graduate Studies (DGS), on behalf of the program; we verify that this is the final, approved version of the student's thesis including all changes required by the advisory committee. The undersigned agree to abide by the statements above.

Ciara Pickering, Student

Dr. William Ford, Major Professor

Dr. Donald Colliver, Director of Graduate Studies

EFFECTS OF WATERSHED DISTURBANCES AND RIVER-TRIBUTARY CONFLUENCES ON SEDIMENTATION DYNAMICS IN THE UPPER OHIO RIVER BASIN

THESIS

A thesis submitted in partial fulfillment of the
requirements for the degree of Master of Science in Biosystems and Agricultural Engineering in the Colleges of Agriculture and Engineering at the University of Kentucky

By

Ciara Pickering

Lexington, Kentucky

Director: Dr. William Ford, Professor of Biosystems and Agricultural Engineering

Lexington, Kentucky

2020

https://orcid.org/0000-0002-8855-7799

ABSTRACT OF THESIS

EFFECTS OF WATERSHED DISTURBANCES AND RIVER-TRIBUTARY CONFLUENCES ON SEDIMENTATION DYNAMICS IN THE UPPER OHIO RIVER BASIN

Harmful algal blooms (HABs) are of increasing concern in the Ohio River Basin. Fine sediment dynamics in riverine environments are increasingly recognized to play important roles in proliferation and toxicity of Microcystis blooms. Further, the fate of sediment at confluences of tributaries and the main river system are important zones for sediment retention and transient storage. The objective of this study was to improve understanding of watershed sediment loading dynamics and backwater inundation influencing sedimentation within confluence watersheds. The study site is the Fourpole Creek watershed in Huntington, WV which is a disturbed forested watershed impacted by a backwater confluence wetland at the junction of Fourpole Creek and the Ohio River. 16 months of high frequency turbidity data was collected at upstream and downstream nodes of the backwater influenced confluence feature near the watershed outlet. Governing hydraulic and sediment transport equations were used to develop a data driven model to estimate sediment fluxes within the confluence floodplain wetland. The continuous sediment yield model estimated an annual yield of 151 t/mi^2. A modified sediment rating curve method estimated an annual suspended sediment yield of only 34.3 t/mi^2. Hysteresis analysis was conducted using a source unmixing method and hysteresis index to quantify sediment source and flow pathways during events. The contribution of three major sources during events were highly variable, but seasonality and antecedent precipitation were both found to be influences. The confluence floodplain was found to have a quantitatively large role in intercepting and storing sediments, retaining 40% of the annual inputs. A numerical sediment transport model estimated 2,055 tons of sediment was permanently retained. Hysteresis was also found to influence the spatial variability of erosion and deposition mechanisms in the floodplain. The floodplain was found to have a particulate nitrogen removal rate from 0.5-0.9kgN/ha/year which is on the same order of magnitude as the nitrate removal rates in this same system. Our results suggest that particulate N fluxes from disturbed forested watersheds near rivers should be considered in watershed N budgets as well as a source for HABs in regulated rivers.

KEYWORDS: backwater confluence floodplain, sediment fate and transport, high resolution water quality monitoring, sediment hysteresis, particulate nitrogen fluxes, mixed-use watershed

Ciara Pickering

07/12/2020

Date

EFFECTS OF WATERSHED DISTURBANCES AND RIVER-TRIBUTARY CONFLUENCES ON SEDIMENTATION DYNAMICS IN THE UPPER OHIO RIVER BASIN

By
Ciara Pickering

Dr. William Ford
Director of Thesis

Dr. Donald Colliver
Director of Graduate Studies

07/12/2020
Date

DEDICATION

In memory of Quentin H. Pickering. He dedicated his career, as a research biologist, to studying water contaminants and pollution control on the Ohio River. I am so thankful for his inspiration and to be able to continue to pursue his passions through my own research.

ACKNOWLEDGMENTS

Although the following thesis is an individual work, it would not have been possible without the support, guidance, and encouragement of several individuals. First and foremost, I would like to acknowledge my graduate advisor Dr. William Ford whose patience, kindness, and genuine interest in his students' success is unparalleled. Without his dedicated guidance and timely feedback, this project would not have been possible. I sincerely hope to emulate his strong work ethic in my own professional career. I would also like to thank my Thesis Committee: Dr. Carmen Agouridis and Dr. James Fox. I was so fortunate to have my first Biosystems and Agricultural Engineering course taught by Dr. Agouridis. Her enthusiasm and expertise were inspirational. Dr. Agouridis was also my undergraduate advisor, playing a significant role in my Environmental Engineering education as well as in my career development by helping me find my first internship. Dr. Fox introduced me to both fluid mechanics and sediment transport and has the unique ability to teach highly complex topics in an engaging and meaningful way. His courses played an integral role in my understanding of the core engineering principals used to produce this thesis.

In addition, I would like to acknowledge the guidance and support of my family and friends. My parents, Bruce and Kathy Pickering, were always there to provide words of encouragement and emotional support. My sisters, Elyse and Alyson Pickering always provided a good laugh and company during much needed breaks. While at the University of Kentucky, I have been blessed with a great support system of friends who I've been able to lean on for encouragement and support.

Thank you to the National Science Foundation whose grant funded my graduate research. I would also like to thank the Biosystems and Agricultural Engineering Department at the University of Kentucky for providing an incredible place to develop an excellent educational foundation through academic studies and research, as well as providing me with an amazing community of colleagues. Lastly, I would like to acknowledge and thank Dr. Ford's research team for their support - specifically Nolan Bunnell, Austin Hoffman, Gina DeGraves, Cory Radcliff, Whitney Phelps, and Katie Emmett. Their help, both in the field and in the lab was invaluable.

TABLE OF CONTENTS

LIST OF TABLES

LIST OF FIGURES

CHAPTER 1. INTRODUCTION

1.1 Importance of Fine Sediments for HAB Formation and Toxicity in Rivers

The occurrence of toxic cyanobacterial Harmful Algal Blooms (HABs) in fluvial freshwater systems has increased since the mid-1990s (NOAA, 2014; Smith, 2003; Chaffin et al., 2013). As an example, the Ohio River Basin has had blooms occur in summer and early fall of 2015 and 2019 which spanned as much as 700 miles of the river and affected municipalities and recreational activities across five states, directly or indirectly impacting 5 million people (Graham et al., 2016). The most common cyanoHAB is *Microcystis Aeruginosa* and its associated toxin microcystin. Microcystin is a hepatotoxin that targets and kills liver cells by bonding with protein phosphate enzymes causing major cell damage and is poisonous to humans, livestock, pets and wildlife (World Health Organization, 2003; Levy, 2017). Microcystin and HABs also have significant economic impacts. HABs reduce property values, reduce tourism and recreation revenue, and increase municipal drinking water treatment costs (Paerl et al., 2016). In the last 10 years, Lake Erie has had two large microcystis blooms which cost $71 million and $65 million in 2011 and 2014, respectively (Paerl et al., 2016). While the causes of HABs are not fully understood, high water temperatures, thermal stratification, low velocities, and eutrophication have all been found to proliferate the blooms (Paerl and Huisman, 2008). Fine sediment dynamics in riverine environments are increasingly recognized to play important roles in proliferation and toxicity of Microcystis blooms due to their contribution to harsh environmental conditions that enable Microcystis to outcompete other plankton for vital resources, their impacts on trophic status, and their potential to seed HABs.

Microcystis' evolutionary traits enable the cyanobacteria to flourish in adverse environments that often limit planktonic production including sediment-laden waters and low-nutrient conditions. Cyanobacteria has been through extreme geochemical and climate changes that have allowed it to adapt and thrive in extreme environments (Paerl and Huisman, 2008). As an example, Microcystis has the ability to inflate and deflate their gas vesicles, an ability other phytoplankton lack (Walsby, 1997; Levy 2017). In turbid waters with high suspended sediment concentrations, this enables Microsystis to inflate their gas vesicles and rise to the surface where more sunlight is available (Walsby, 1997; Levy 2017). Growth rates of other phytoplankton are limited by light availability due to the light attenuation properties of the sediment (Dijkstra, 2019). Alternatively, the gas vesicle can also be deflated when a cell is running low on phosphorus to allow the organism to sink to the riverbed and acquire sediment bound nutrients (Levy, 2017). These dynamics may be particularly important in mesotrophic or oligotrophic systems (with low dissolved nutrients) where other plankton will experience rate-limiting growth conditions associated with nutrient limitations (Cottingham et al., 2015).

The most important condition necessary for HABs to occur is abundance of bioavailable nutrients for production, and fine sediments are recognized to supply bioavailable nutrients in freshwater systems. Cyanobacteria, like many other microorganisms, use nutrients to create energy (ATP) necessary for their growth and reproduction. The two rate-limiting nutrients that fuel HABs are phosphorus (P) and nitrogen (N) (Elser et al., 2007, Lewis et al., 2011; Paerl et al., 2016). One of the first extensively studied HABs occurred in the 1960s on Lake Erie. Poorly treated sewage, industrial waste, and runoff from surrounding farms brought in excessive amounts of

phosphorus and nitrogen allowing cyanobacteria to flourish. After extensive investigation, researchers found that phosphorus was the key nutrient in freshwater algal bloom proliferation (Edmonson, 1971; Levy, 2017). This idea was widely accepted by other researchers as well, and the Environmental Protection Agency (EPA) even mandated total maximum daily loads (TMDLs) for P in hopes of decreasing the intensity and occurrence of algal blooms (Paerl et al., 2016).

Studies have also emphasized the importance of N forms to influence HAB production and toxicity. Chaffin and Bridgeman (2013) investigated which of the four different forms of N, NO_3^-, NH_4^+, urea, and the amino acid alanine, caused cyanobacteria growth to be the greatest and found that ammonium had the highest preference index in all of their experiments, meaning that cyanobacteria will utilize all forms of N, but prefer ammonium for optimal growth. Caraco et al. (1989) found that mineralization of organic matter and the related sulfur cycling can significantly increase the ammonium and phosphate in the sediment porewater, which is then mobilized in the waterway with any disturbance to the sediment. Nevertheless, nutrient release from sediment is rarely regarded as an important environmental concern despite the fact that it could have a significant impact on the total nutrient loads of a water body (Morgan et al., 2012). Morgan et al., preformed a study to investigate the impact of sediment resuspension on surface water nutrient concentrations. When the sediment was suspended it was found that both NH_4^+ and PO_4^- were released into the water increasing the total concentrations of each. Formation of Fe hydroxides, through the oxidation of the sediment FeS, returns the PO_4^- quickly back to the sediment bed, limiting the dissolved PO_4^- concentration over time. However, NH_4^+ can continue to be released from the suspended sediment over longer periods of time,

actually increasing the overall N concentration in the water (Morgan et al., 2012). This warrants further investigation into sediment nutrient fluxes, particularly high in sediment nitrogen.

Recent research has shown that sediment in tributaries store not only nutrients but also high levels of phytoplankton, including Microcystis (Conroy et al., 2014). Conroy et al. found that Microcystis comprised a large percentage of algal groups in the Maumee and Sandusky Rivers suggesting the rivers as a potential source of inocula for summer blooms that occur annually in Western Lake Erie (Conroy et al., 2014; Kitchens et al.,.2018).The annual cycle of Microcystis begins with an overwintering period in the upper layers of sediment. As water temperatures rise in the spring it renters into the water column and proliferates causing the HABs before returning back to the sediments in the fall (Kitchens et al., 2018). It is hypothesized that Microcystis cells pick up vital nutrients from the sediments during overwintering to later fuel early season growth (Kitchens et al., 2018). Based on these lines of evidence, it is clear that fine sediments and their associated bio-chemical properties play an important role in the formation and toxicity of algal blooms in riverine environments.

1.2 Objectives

The Upper Ohio River basin has experienced multiple river spanning toxic cyanobacterial Harmful Algal Blooms (HABs) over the past five years, reflecting a growing trend among freshwater rivers (Smith, 2003; Chaffin et al., 2013). This portion of the Ohio River Basin drains the Western Allegheny Plateau ecoregion of Appalachia. The ecoregion (32,630 mi^2) is roughly 63.7% forest, 23.9% agriculture, 7.5% urban, and 0.2%

wetland (United States Geological Survey, n.d.). The forested areas are classified as mixed mesophotic forests consisting of maple, buckeye, beech, tulip tree, oak, and linden. The agricultural areas are a combination of cropland and pasture but remain mostly un-grazed (Omernik, 1987). The urban areas are primarily located in the valleys, adjacent to large rivers. Management of sediment and their associated nutrients in large river systems is most effectively met by focusing on waterways that are near large rivers and have limited transit times (Alexander et al., 2008). As will be shown in Chapter 2, limited suspended sediment transport research has been conducted in this ecoregion. The focus of this thesis is on quantifying sediment source and transport dynamics in confluence tributary watersheds of the Western Allegheny Plateau and quantifying the implications for the fluvial N budget.

Five primary objectives of this research are defined below and serve as a template for the subsequent sections of this thesis:

1) Measurement of sediment yields from disturbed watersheds in the Western Allegheny Plateau ecoregion.
2) Quantify temporal variability of sediment pathway dynamics by coupling sediment hysteresis analysis with source unmixing and comparing with relevant environmental drivers
3) Measure capacity of backwater floodplains occurring at confluences of small tributaries and large riverine systems to buffer sediment fluxes to regulated rivers.
4) Simulate the sedimentation dynamics within confluence floodplains including depositional and erosion patterns in the floodplain and stream channel.
5) Assess the implications for fluvial N budgets in disturbed Appalachian watersheds.

1.3 Thesis Contents

Chapter 1: Introduction. Provides an overview of the role of fine sediments in proliferation of harmful algal blooms, defines the objectives of this thesis (serving as a template for organization of the thesis), and defines the contents of this thesis.

Chapter 2: Literature Review. Provides a review of research focused on sediment fluxes in Appalachian watersheds, sediment source and flow pathway dynamics in mixed-use watersheds, sediment dynamics in backwater confluences of streams and regulated rivers, numerical modeling of confluence floodplain sedimentation dynamics, and role of particulate nitrogen in total nitrogen budgets.

Chapter 3: Methodology. Outlines methodology for the data collection, data analysis, and the modeling framework for both the sediment flux model and the confluence floodplain sediment transport model.

Chapter 4: Results. Details the results of the sediment flux model, the hysteresis and sediment source decomposition analysis, the confluence floodplain sediment transport model, and the particulate nitrogen yield estimates.

Chapter 5: Discussion. Discusses the results and implications from the investigation of watershed and confluence floodplain sediment transport dynamics.

Chapter 6: Conclusions and Future Work. Summarizes the major findings of this thesis and highlights future research needs.

Chapter 7: References Cited. Lists the details of works cited in this thesis.

CHAPTER 2. LITERATURE REVIEW

2.1 Sediment Fluxes in Appalachian Watersheds

Few studies have investigated sediment fluxes Appalachian watersheds and the sediment fluxes reported are highly variable (see Table 2.1). Of the studies that have been conducted, the majority are focused on watersheds in the Central Appalachian ecoregion. No studies in our review reported sediment flux estimates for watersheds in the Western Allegheny Plateau. The majority of sediment flux studies were conducted by government agencies for infrastructural purposes such as predicting the usable life span of on-stream reservoirs, designing domestic water supplies, and setting total maximum daily loads (U.S EPA, 2007; Williams and Reed, 1972; Bolstad et al., 2006). A few other studies were focused on assessing the impact of mining disturbances on watershed sediment fluxes (Burns and McArthur, 1996; Ward, 1984; Fox and Martin, 2015). Although two of the studies were conducted in mixed use watersheds, none examined the influence of landcover on watershed sediment fluxes or specifically the role of urban disturbances. The urban influences may be particularly important since urban areas throughout Appalachia are often located near tributary-main river confluences. Because of the proximity to the regulated river, contaminants have short transit times, limiting the tributaries ability to decrease contaminants exported to the main river (Alexander et al., 2008; Ford et al., 2020).

Regarding methods of measuring sediment fluxes, studies in Appalachia have predominately used variations of sediment rating curves to estimate annual sediment loads. However, in other watersheds (outside of Appalachia) rating curves developed from weekly or even daily sampling have been found to be an inadequate way to characterize the temporal variability in suspended sediment concentration, usually missing peak

hydrologic events which are the periods of greatest concentration (Lewis and Eads, 2009). In addition, mixed-use watersheds found in Appalachia have variable sediment source dynamics. But even after extensive monitoring, a single rating curve likely cannot account for the change in the hysteretic behavior from event to event. To overcome this, methods such as rising and falling limb rating curves have been used to attempt to account for hysteresis patterns. Nevertheless, accurate quantification of sediment yields may require long-term, continuous monitoring of both discharge and suspended sediment concentration (Schilling et al., 2011).

Increased robustness and reliability of in situ water quality monitoring sensors have reduced this barrier for researchers and allowed continuous high-frequency monitoring at resolutions that were previously infeasible (Vaughan et al., 2017). Specifically, in stream turbidity sensors are a widely used surrogate for suspended sediment concentrations capable of capturing diel variations in sediment concentrations and storm event dynamics (Snyder et al., 2018). Turbidity is a measurement of the optical clarity of water and it correlates well with suspended sediment concentrations because the turbidity is largely controlled by suspended particles in the water column that scatter light (Rasmussen et al., 2009; Jastram et al., 2010). A relationship can be established to continuously predict suspended sediment fluxes from the turbidity data, accurately capturing variable sediment dynamics during events. Of the few studies quantifying annual sediment yields in Appalachia, none have utilized high resolution turbidity sensors or assessed how typical rating curve methods impact estimation of seasonal and annual sediment fluxes.

2.2 Sediment Source and Flow Pathway Dynamics in Mixed-Use Watersheds

Management of sediment yields from watersheds require a rigorous understanding of the sources activated during storm events because events are key periods in which both nutrients and sediment are mobilized, transported along flow pathways, and delivered to adjacent waters downstream (Lloyd et al., 2016a; Beschta, 1987; Evans et al., 2003; Meade and Parker, 1985; Walling and Webb, 1987). Storm event analyses can provide a unique insight into variability in the sources of solutes and sediment within the watershed and the hydrologic pathways that connect the sources to the stream channel (Wymore et al., 2019). An understanding of the transport pathways activated during storm events can be developed by studying the changing relationships between discharge and water quality parameters throughout the length of the event. This relationship often exhibits a non-linear loop like behavior known as hysteresis (Lloyd et al., 2016a). Hysteresis loops vary in size and shape as a result of the lag in response time between the peak discharge and the peak concentration (Lloyd et al., 2016b). Hysteresis loops that fall into the same class, suggest similar sources and transport processes are occurring during both events.

Hysteresis analysis has been used to link sediment source availability and flow pathway dynamics to watershed sediment fluxes in mixed-use watersheds. The supply and location of sediment sources within the watershed have a strong influence on the hysteretic behavior during storm events (Gellis, 2013). Mixed-use catchments have a variety of loop types and can experience more complex hysteresis loops, like figure-8 patterns, as a result of a combination of sources and transport processes occurring simultaneously. Cumulatively, previous research suggests that qualitative hysteresis analysis and quantitative hysteresis indices can help inform important sources of sediment fluxes in

watersheds and provide insight into time-varying land cover controls from these watersheds (Wymore et al., 2019). The following provides a review of the relevant land cover impacts on sediment source supply and documented hysteresis effects.

In forested watersheds, the suspended sediment in streams is supplied from floodplain erosion, mass movement, surface erosion on hillslopes, subsurface erosion sources, and previously deposited sediments in the stream network. Floodplain erosion rates in forested headwater streams are typically low but can be an important source of fine sediment in areas where floodplains exist adjacent to the stream channel (Gomi and Hassen, 2005). Mass movements such as landslides and debris flows are infrequent external sediment sources in forested steepland regions but can be a major source during the storm events in which they occur and the contribution to the suspended sediment supply depends of the degree of connectivity from the hillslopes to the stream channel (Gomi and Hassen, 2005; Roberts and Church, 1986). In general, surface erosion is not a large contributor to the suspended sediment yields due to the dense vegetation cover in forested areas. However, during high antecedent moisture conditions, overland flow may mobilize sediment from areas that are not typically connected to the channel network (Gomi and Hassen, 2005; Rivenbark and Jackson, 2004). Regarding subsurface erosion sources, recent studies have suggested that sediment concentration peaks on the receding limb in forested watersheds may be attributed to subsurface sediments originating from macropores, which can induce complex hysteresis loops when activated (Wymore et al., 2019). Previously deposited sediments in forested streams may become partially or totally mobilized and contribute to the suspended sediment and is dependent on the availability of fine sediment storage in the channel (Paustian and Beschta, 1979; Sidle and Campbell, 1985). Often there

is also some seasonal variability to the accumulation and exhaustion of the stored surface material and this source results in a clockwise hysteresis loop (Gellis, 2013).

Anthropogenic disturbances and spatial distribution of these disturbances within a watershed add to the complexity of analyzing sediment source dynamics in mixed used watersheds. Sediment sources in agricultural watersheds include erosion of upland soils, collapse of streambanks, and resuspension of bed sediments, which could result in both clockwise and counter-clockwise hysteresis pending proximity of agricultural land-cover to the stream monitoring station (Schilling et al., 2011). Sediment sources in urban watersheds are streambanks, streets, and uplands (Devereux et al., 2010). Urban areas experience high runoff volumes that dilute the suspended sediment concentrations on the rising limb and the upland sediments often arrive on the receding limb subsequently resulting in counterclockwise hysteresis loops (Gellis, 2013). Due to the flashy nature of these systems, streambanks have often been found to be the main contributor to suspended sediment loading in urban systems and would exhibit single-line hysteresis patterns since this source increases proportionally with flow (Williams, 1989; Megnounif et al., 2013). Megnounif et al. (2013), recently developed a method that enables source unmixing based on hysteretic patterns. Source signals are used to partition sediment yields into baseload and wash loads. Wash loads represents the supply of new sediment sources that become available, such as upland sources as well as the re-suspension of recent deposits throughout the fluvial network (Megnounif et al., 2013). Baseloads are a result of the erosive power of the flow and represent the erosion of gully, streambed, and streambank sources. The baseload may be exacerbated in urban streams where flashy hydrologic response results in high peak flows that are dilute in upland sediments (Gellis, 2013; Megnounif et al., 2013).

2.3 Backwater Confluences of Streams and Regulated Rivers

Backwater confluences are low gradient regions where low-order tributaries discharge to larger, high-order regulated rivers. These features are abundant in large regulated river basins and serve critical economic and ecological functions as they often form floodplain wetlands (Ford et al., 2020). During flooding, the tributary and the floodplain become hydrologically connected when the riverine floodwaters meet the locally derived water in a process known as perirheic mixing (Junk et al., 1989; Tockner et al., 1999; Jones et al., 2014). Zones of perirheic mixing promote rapid deposition-erosion dynamics and nutrient transformation processes due to increased hydraulic residence times and steep redox gradients (Mertes 1997; Banach et al., 2009; Chow et al., 2013; Jones et al., 2014; Jensen and Ford, 2019). For this reason, floodplain wetlands have been proposed as a watershed management strategy to reduce nitrogen loads in the lower Mississippi River Valley (Mitsch et al., 2001), yet it is imperative to implement strategies that maximize pollutant removal while minimizing the mobilization of nutrients (Jones et al., 2014). Given that fine sediments are rich in nutrients that are subject to regeneration, consideration of sediment transport dynamics is critical for effective management.

Historically, research on sedimentation dynamics in confluence features began with a focus on confluence geometry and geomorphology and the implications for depositional fluxes in downstream portions of the main-river reach. Miller (1958) was one of the first scientists to bring attention to confluences when he noted changes in channel width and bed material at channel junctions. His research proposed a relationship between the channel width downstream of the confluence and the widths of the two converging channels. While this work was relatively rudimentary, it emphasized the significance of channel

confluences as important points of change within a fluvial system. This encouraged others to begin to investigate confluence features. Several following studies found that the confluence angle and the discharge ratio between the confluent channels are the dominant control on flowrates, sediment transport processes, and bed morphology at the confluences (Mosley,1976; Best, 1986). Knighton was one of the first to study sediment dynamics at confluences and documented that the change in downstream grain size of the bed material within the main channel is related to the geology and length of the confluent tributary (Knighton, 1980; Best, 1986). Contemporary research on sedimentation dynamics in confluences of small tributaries with large rivers have all continued to focus on downstream sedimentation dynamics (Benda et al., 2004; Leite Ribeiro et al., 2012; Marren et al., 2014). Only recently have studies assessed sedimentation dynamics of backwater confluence features (Ford et al., 2020). A need exists to quantify the magnitude of sediment depositional fluxes in confluence floodplains.

2.4 Numerical Modeling of Confluence Floodplain Sedimentation Dynamics

In backwater confluence zones, river and tributary flow regimes and sediment source dynamics are perceived to be key drivers of sedimentation dynamics (Ford et al., 2020). Isolated backwater flooding of the regulated river is caused by regional storm events. The flow conditions on the regulated river rise and the confluence becomes inundated creating zones of nearly stagnant flow. The backwater decreases the energy gradient and promotes deposition of river sediments on the confluence floor. Isolated flooding of the tributary is caused by local events. The flow conditions on the tributary rise and causes downstream flooding. Local events increase the energy and transport capacity of the fluid entering the tributary and sediment from the upland sources and in-stream

sources is transported downstream through the confluence and to the river. However, due to the low gradient nature of most confluence zones, the decelerating flow conditions encourage some deposition of tributary sediments on the confluence floor before being discharged to the river. Concurrent flooding of both the river and the tributary is most often the case during storm events and results in a highly complex mixture of two contrasting flow conditions for isolated river and tributary flooding. The sedimentation dynamics at the confluence during concurrent flooding are a combination of sediment deposition from the river's backwater, sediment deposition from the tributary, and sediment erosion and transport through the confluence through to the river (Ford et al., 2020). Ford et al. (2020) used isotope tracers to identify source provenance of sediments from the tributary and riverine sources in a backwater confluence stream channel. The study recognized that these measurements provide only a snapshot in time, and thus temporally dynamic depositional dynamics remain poorly understood and alternative methodologies are needed to characterize floodplain depositional patterns and the governing mechanics.

Given the hydraulic and sediment source complexity, time-stepping numerical modeling of floodplain wetland systems may help quantify prevailing controls on sedimentation dynamics in these understudied watershed features. Due to the unsteady, non-uniform flow conditions that occur in backwater confluences, unsteady flow modeling is needed to accurately simulate the complex hydrodynamics. Regarding sediment transport processes, erosion/deposition may occur in both floodplains and the stream channel and need to be considered. Potential sinks of sediment include deposition to the floodplain and streambed, while potential sources include erosion of floodplain and stream sediments (including remobilization of previously deposited sediments), and erosion of

cohesive streambanks. Modeling these systems can provide insight into hotspots of sediment erosion and deposition dynamics in confluence features.

In order to validate such models, high-frequency upstream-downstream monitoring platforms are critical to capture the rapidly varying source and transport dynamics. Sediment transport models require continuous sediment input time series data at the boundaries (Lepesqueur et al., 2019). Robust sediment transport boundary conditions are very important to accurately model the sedimentation dynamics and become even more important in unsteady flow models (Gibson, 2006). Insufficient boundary conditions can often be a source of model error, as well as model instability (Gibson, 2006). The majority of sediment is transported during storm events lasting only a small fraction of the year (Inamdar et al., 2015). These events have highly variable sediment transport patterns that cannot be accurately represented by manual sampling alone (Lepesqueur et al., 2019). The unpredictability of sediment transport is only further complicated by the variable hydraulic conditions at the confluence of these backwater systems. Alternating tidal flow conditions and the associated sediment dynamics of the river and tributary result in highly complex boundary inputs to the control volume. In sediment transport modeling, high-frequency turbidity monitoring is often recognized as the best proxy for obtaining the continuous time series of SSC that is needed for the boundary conditions (Martínez-Carreras et al., 2016; Lepesqueur et al., 2019).

2.5 Implications for Nitrogen Budgets

Particulate nitrogen delivery from steep-gradient Appalachian watersheds with predominantly forested landcover is likely a significant contributor to fluvial N budgets in

the Western Allegheny Plateau. Traditionally, nutrient research has focused almost exclusively on dissolved species of nitrogen and neglected particulate nitrogen (Galloway et al. 2008). Nevertheless, recent studies have shown that in steep-gradient watersheds, particulate N may be the dominant form of N transported during storm flows (Hoover and Mackenzie, 2009; Taylor et al., 2015; Inamdar et al., 2015). In a forested watershed with moderate slope gradients, Inamdar et al. (2015) found that particulate nitrogen was the dominant form of nitrogen transported during storm events and contributed up to 87% of the total nitrogen concentrations. These fluxes are important to consider, as a large portion of the particulate nitrogen exports are then deposited within the fluvial network and subject to regeneration, through mineralization and subsequent nitrification, during low flow and low input conditions (Peterson et al., 2001). The deposition and subsequent transformations of particulate nitrogen exports in the fluvial network could have significant consequences for nitrogen cycling in downstream regulated rivers; therefore, understanding the timing and magnitude of PN yields is recognized.

Regarding confluence floodplains, their net source/sink capacity broadly depends on sedimentation dynamics and subsequent fate of particulate N within the confluence. Many studies have characterized riverine wetlands as net sediment and nutrient sinks with little analysis of site nutrient and sediment budgets or deposition and erosion processes (Arp and Cooper, 2004). In river water, phosphorus is often adsorbed to sediment particles causing sediment deposition to be widely recognized as a major source of dissolved reactive phosphorus in floodplain wetlands (Mitsch et al. 1979; Johnston 1991; Vought et al. 1994; Olde Venterink et al., 2006). Sediment deposition is generally not recognized as a major source of dissolved inorganic nitrogen in floodplain wetlands because the fraction

of nitrogen adsorbed to suspended matter is typically low in river water. However, the annual N-input by sediment deposition per area floodplain has still been found to be very high, often exceeding 100 kg-N/ha/year (Olde Venterink et al., 2006). It has been questioned whether the nutrient inputs from sediment deposition is permanent or temporary, since these sediments could be resuspended during future inundation events, or regenerated through biochemical processing (Peterson et al., 2001; Olde Venterink et al., 2006; Ford et al., 2017). It is imperative to understand sediment N being deposited and eroded spatially throughout the floodplain to understand how confluence floodplains influence water quality.

Accurate estimates of particulate N yields and depositional dynamics requires coupling of high frequency sediment dynamics with sediment N composition, which can vary with sediment source inputs. In part, particulate nitrogen fluxes are underrepresented in fluvial nitrogen budgets because they require accurate quantification of sediment fluxes and temporal variability of sediment N composition. High-frequency turbidity sensors may partially overcome this limitation. Organic particles and organic coatings on inorganic sediments can absorb light instead of scattering it causing non-linearity to occur between suspended sediment concentration and turbidity (Bright et al., 2018). Since particulate organic matter (POM) can scatter light differently than inorganic materials, turbidity has been used as a surrogate for POM concentrations and has even been found to be a better indicator of turbidity than suspended sediment concentrations in some systems (Bright et al., 2018). The relationship between POM content and turbidity may enable elucidation of continuous particulate N flux estimates within the watershed.

2.6 Tables and Figures

Table 2.1. Reported sediment load estimates for Appalachian watersheds.

Reference	Ecoregion	Landcover	Watershed Size	Sediment Loading Methods	Sediment Loading Estimates
Burns and McArthur (1996)	Central Appalachians	Over 60% forested with some mining disturbances	263 mi^2	Fit upper and lower curve to sediment yields from published studies in the region	325-708 $t/yr/mi^2$
Williams and Reed (1972)	Ridge and Valley	65% Forested, 15% Cultivated, 17% Grass, 3% Urban	301 mi^2	Estimated from measured sediment yields at various stations	76 $t/yr/mi^2$
	Piedmont Plateau	22% Forested, 40% Cultivated, 41% Grass, 3% Urban	510 mi^2		220 $t/yr/mi^2$
	Appalachian Plateau	64% Forested, 9% Cultivated, 19% Grass, 8% Urban	282 mi^2		140 $t/yr/mi^2$
Bolstad et al. (2006)	Blue Ridge	100% Forested	2.2 mi^2	Estimated using separate rating curves were generated for the rising and falling limbs of the hydrographs due to hysteretic relationships.	*9.3 $t/yr/mi^2$
		100% Forested	0.6 mi^2		*6.2 $t/yr/mi^2$
		72.6% Forested, 26.2 % Agricultural	0.5 mi^2		*32.6 $t/yr/mi^2$
		95.8% Forested	1.7 mi^2		*37.3 $t/yr/mi^2$
		87.3% Forested, 4.9% Agricultural	6.5 mi^2		*88.6 $t/yr/mi^2$
U.S. EPA (2007)	Central Appalachians	63.4% Forested, 19.1% Pasture, 11.1% Cropland, 6.3% Urban	285 mi^2	Estimated using a sediment delivery ratio formula found using the CBP Phase V Model	63 $t/yr/mi^2$

Dun et al. (2013)	Central Appalachians	100% Forested	0.12 mi^2	Assumed equal parts of particulate and dissolved matter and estimated the concentration of dissolved matter from the measured anion and cation concentrations	36.25 $t/yr/mi^2$
		100% Forested	0.13 mi^2		20.72 $t/yr/mi^2$
Ward (1984)	Central Appalachians	Predominately forested with mining and logging disturbances	5.06mi^2	Estimated d using suspended-sediment regression curves for each water year	22.9-139.5 $t/yr/mi^2$
		Predominately forested with human disturbances	151 mi^2		38.7-174.9 $t/yr/mi^2$
Fox and Martin (2015)	Central Appalachians	91% Forested, 9% Reclaimed mining	1.36 mi^2	Estimated using a sediment yield model calibrated by sediment fingerprinting	207.2 t/yr/mi^2
		91.6% Forested, 8.4% Reclaimed mining	0.86 mi^2		440.3t/yr/mi^2

CHAPTER 3. METHODOLOGY

3.1 Study Site

To meet the objectives of the study, the Fourpole Creek watershed (60.6 km^2) located in southwestern West Virginia was selected as the study site. Fourpole Creek is a fourth order tributary of the Ohio River and the outlet of the watershed is located along the Ohio River in Huntington, WV (Figure 3.1). This watershed was selected for study because: 1) the watershed is part of a broader NSF EPSCoR RII T2 project focused on studying controls of nutrients to the Ohio River, 2) previous studies have been conducted on sediment and nitrogen dynamics in the watershed (Jensen and Ford, 2019; Ford et al., 2020), 3) Fourpole Creek and its watershed is representative of the broader land cover, geology, and topography in the ecoregion (Jensen and Ford, 2019) suggesting that findings may help inform the transport dynamics of the broader ecoregion; 4) the presence of a backwater confluence floodplain at the watershed outlet that has well-defined upstream and downstream boundaries for monitoring and numerical modeling applications.

Upstream of the confluence floodplain wetland, the majority of the watershed experiences moderately high slopes (Figure 3.2) around 87-131. The highest slopes are found in the southwestern area of the watershed which is within 4 miles confluence floodplain. The slopes drastically decrease as you approach the confluence with the Ohio River. The northern areas of the watershed experience extremely low slopes ranging from 0-38%. The Foupole Creek watershed has geology composed of shale, sandstone, and alluvium with predominantly C hydrologic group soils. The predominate soil type in the uplands is Gilphin-Upshur, found in different textures and at different slopes (Figure 3.3). These lowland areas have the highest intensity of development. There are small areas of

fully developed and currently developing areas in the uplands of the watershed, but it remains predominately undisturbed forested land. The majority of the forested area is deciduous forest with areas of mixed forest found along upstream tributaries of Fourpole Creek. There are some small agricultural disturbances in the uplands, however the agricultural land use is largely pasture/grassland with hardly any cultivated crops. Overall, the Fourpole Creek watershed is a mixed-use watershed with 62% forested, 34% urban and 3% agricultural/grassland land uses (Figure 3.4).

At the confluence of Fourpole Creek and the Ohio River is a riparian forested wetland (Figure 3.5), which is regulated by hydrologic regimes of the Ohio River and Fourpole Creek (Ford et al., 2020). The wetland area is 0.25 km^2 or about 0.4% of the total watershed drainage area. Most of the wetland is classified as a palustrine forested wetland, meaning it is a nontidal wetland dominated by trees, shrubs, mosses, and lichens (Jensen and Ford, 2019). The water regime is classified as temporarily flooded so surface water is often present throughout the wetland for short periods of time. The inundation levels of the wetland are primarily controlled by backwaters from the Ohio River, but could also be influenced by extreme local events. The stream channel is well defined and is comprised primarily of coarse-grained (greater than 53 micrometer) sediments, with limited transient storage (Ford et al., 2020). The tributary overbanks are predominately Chargin-Melvin silt loam that becomes flooded frequently. Another predominate soil type found in the confluence floodplain is Chagrin silt loam. It lies in areas with 0 to 3 percent slopes and occasionally becomes flooded. Throughout the floodplain areas of udorthents can be found. These are areas of wet soils where the upper soil material has been disturbed.

This study leverages two monitoring stations that are part of the NSF SENSE monitoring program (Figure 3.5). At the confluence of Fourpole creek and the Ohio River is a confluence floodplain wetland that is frequently inundated during high flows from the Ohio River, creating backwater tidal inputs from the river, and non-uniform flow conditions propagating upstream. We have established high-frequency monitoring platforms upstream of the wetland and at the river confluence. At the upstream location, a YSI EXO2 sonde was deployed from August 2018 to present. At the downstream station, a YSI EXO2 sonde, SUNA V2 nitrate sensor, and two Teledyne 6712 automated samplers were located at the Fourpole Creek floodwall station and have been deployed since June 2017. Automated samplers were not possible at the upstream location because of vandalism and theft issues. At both upstream and downstream locations, time-integrated sediment trap samplers have been deployed and have collected weekly samples since July 2016 (Phillips et al., 2000).

3.2 Data Collection and Analysis

YSI EXO2 sondes at both stations included sensors to measure turbidity, fDOM, conductivity, temperature, pH, dissolved oxygen, and depth at a 15-minute resolution. The sonde probes were cleaned and calibrated once a month to prevent instrument drift. There are no built in QC flags for the YSI EXO2 outside of the SmartQC mechanism used during calibration. Six quality control checks were used as outlined by Campbell et al. (2013): date and time, range, persistence, change in slope, internal consistency, and spatial consistency. The time and date of each deployment was recorded in the field notes and the time and date stamps were cross checked with the actual date and time of deployment. The sondes were always deployed in the current time zone, EST or EDT. The time and date

stamps were manually corrected for data sets from sondes deployed in the field during a time change. A MATLAB script was developed to flag data that fell outside of the measurable range for each sensor probe. The ranges were defined for each sensor probe in the EXO User Manual. The data was manually reviewed for identical sequential measurements and periods of data where this occurred were omitted since this is indicative of sensor failure or fouling. The data was also manually reviewed for sharp increases or decreases over a short intervals and periods where this occurred were also omitted since this indicates the sensor was disturbed or malfunctioned. Internal consistency was reviewed by checking for consistency in trends between related parameters (i.e. conductivity often decreases as turbidity increases). Spatial consistency was reviewed by comparing general trends in the data between the two sites. Linear interpolation was used to gap-fill data that was deemed erroneous (Snyder et al., 2018; Campbell et al., 2013).

Due to vandalism and theft issues, automated samplers were not used at the upstream YSI monitoring station. Instead, Teledyne ISCO 6712 samplers were installed at the floodwall station approximately 2 km downstream. Samplers were utilized from November 2018 to August 2019. One sampler was programed to collect a sample every seven hours for a week and when the first sampler finished its program the second sampler followed the same routine for the next week. In addition to these regular interval samples, storm events were targeted and the samplers were programed to take hourly samples in order to collect high resolution data and capture both the rising and falling limb of the events. The samples were collected bi-weekly and brought back to the laboratory where the samplers were refrigerated in a dark space until analysis.

Each of the ISCO grab samples were filtered using Whatman GF/C 1.2µm filters, dried, and then reweighed to determine the total suspended solids (TSS) concentration per EPA method 160.2 (NCASI Technical Bulletin No. 291, 1977). After the samples were analyzed for TSS, the filters were placed in a muffle furnace at 550°C and then reweighed to determine the particulate organic matter (POM) content following standard methods (ATSM, 2002). Prior to filtration, a turbidity measurement of the homogenized sample was taken for each grab sample using a YSI EXO2 sonde identical to the sonde measuring the turbidity in the field and 50mL of each sample was subsampled for particle size distribution analysis. A LISST-Portable XR laser diffraction particle size analyzer from Sequoia Scientific was used to obtain a particle size distribution for each sample.

3.3 Analytical Methods

3.3.1 Sediment Flux and Yield Estimates

A site-specific suspended sediment concentration prediction model was developed to estimate suspended sediment concentrations from the continuous turbidity measurements. The measured TSS concentrations and the corresponding turbidity measurements were compiled and a power relationship was established for this data set. Turbidity measured in the field was used as the explanatory variable and a regression model was computed to predict the response variable, TSS. A simple regression model is usually sufficient for the relation of turbidity to suspended-sediment concentration, but in some cases a multiple linear regression with turbidity and flowrate as the explanatory variables can do a better job predicting the suspended sediment concentration (Rasmussen et al., 2009). Since the grab samples were collected at the confluence, backwater from the Ohio River may result in contrasting sediment source inputs that have a different TSS-Turbidity

curve. To investigate if these factors had any impact on the turbidity-suspended sediment concentration relationship, a multiple linear regression was also performed with both turbidity and flowrate as the explanatory variables. To validate the prediction model created from field turbidity measurements, another simple linear regression was performed with the lab measured turbidity measurements and their corresponding TSS concentrations. This was to ensure/validate that drift or fouling in the field did not strongly influence TSS-Turbidity relationships.

To verify analogous sediment properties and TSS-Turbidity curves at the downstream and upstream site, we performed a laboratory study in which artificial TSS-Turbidity curves were developed using sediment trap samples at upstream and downstream locations (Ford et al., 2020). As previously discussed, grab samples could not be collected at the upstream site, so it had to be assumed that the relationship between turbidity and suspended sediment concertation at the upstream site was the same as the computed relationship at the downstream site. To confirm this assumption, a small laboratory investigation was conducted. Archived sediment trap samples from both sites were used to create artificial grab samples for both the respective sites. The concentrations of the artificial samples ranged from 50mg/L to 1200mg/L and were created using sediment samples from different seasons over multiple years to account for temporal sediment concentration variability. Turbidity measurements were taken for each sample using a YSI EXO2 sonde. Regressions were performed for the upstream and downstream lab test and the turbidity-suspended sediment concentration relationships. Hypothesis testing, specifically a t-test, was used to determine if there was a difference in the regression coefficients and no statistical difference was found.

Following estimation of continuous TSS estimates at the depth of the sensor, a data driven model was created in MATLAB to estimate sediment fluxes and yields following well-established methods for fixed-station monitoring platforms. Discharge of suspended sediment was calculated as follows (Chang, 1988).

$$q_{ss} = \int_a^D Cu\, dz \tag{3.1}$$

where, q_{ss} is the suspended sediment flux per unit width of the channel (mg/s/m), D is the flow depth (m), a is the depth at which sediment suspension begins (m), C is the suspended sediment concentration (mg/m^3), and u is the velocity (m/s).

This requires both a concentration and a velocity profile that vary over the flow depth. The velocity profile was found by calculating the velocity at 50 different depth intervals evenly spaced throughout the depth profile. This was done for each time step using the following log-law equation:

$$\frac{u}{U_*} = 8.5 + 2.5 \ln\left(\frac{z}{k_s}\right) \tag{3.2a}$$

$$U_* = \sqrt{gRS_f} \tag{3.2b}$$

$$S_f = \frac{Q|Q|n^2}{2.208 R^{\frac{4}{3}} A^2} \tag{3.2c}$$

where, U_* is the shear velocity (m/s), S_f is the friction slope (m/m), Q is the volumetric flowrate, n is the Manning's roughness coefficient (unitless), u is the fluid velocity at the specified flow depth (m/s), z is the depth of interest (m), and k_s is Nikuradse sand roughness (m). There are no gaging stations monitoring flowrate within Fourpole Creek since there is often non-uniform flow conditions, so the flowrates at the upstream location

were estimated using an area weighted discharge method based on flowrates at a nearby stream gage with comparable watershed characteristics (Jensen and Ford, 2019; Emerson et al., 2005). This method uses known flowrates from a neighboring reference watershed and the ratio of both watersheds' drainage area to predict the unknown flowrates in the watershed of interest using the following equation:

$$Q_{FC} = Q_{HC} * \left(\frac{DA_{FC}}{DA_{HC}}\right) \quad (3.3)$$

where, Q_{FC} is the estimated stream flow in cubic feet per second for the site of interest (Fourpole Creek), Q_{HC} is the streamflow in cubic feet per second for the streamflow at the gaging station of the reference watershed (Hurricane Creek), DA_{FC} is the drainage area in square kilometers for the watershed of interest (Fourpole Creek), DA_{HC} is the drainage area in square kilometers for the watershed in which the streamflow gaging station is located (Hurricane Creek).

Hurricane Creek has USGS gage station 03201405 monitoring discharge at a 15-minute resolution, so it served as a good reference watershed. It neighbors the Fourpole Creek watershed and lies approximately 17 miles to the east. In addition to its proximity, the watersheds are very similar in size, soil type, land use, and geology (Jensen and Ford, 2019). Although the Fourpole Creek watershed and the Hurricane Creek watershed are only a few miles apart, winds typically move storms from west to east. The Hurricane Creek watershed lies almost due east of the Fourpole Creek watershed, creating the potential for differences in the timing of peak flowrates. This lag time between the peak flowrate in Fourpole Creek and Hurricane Creek is mostly dependent upon the speed at which the storm is moving. This is variable for each individual storm event, so the lag times

were investigated for 19 different events. This was done by comparing the timing of the peak depth reported from the YSI at the upstream monitoring station to the timing of the peak flowrate calculated using the area weighted discharge method. For every event the flow depth peaked before the peak discharge. The difference in peak to peak timing ranged from 45 minutes to 5 hours with a median of 2.5 hours. For the investigation of individual events the peak depth and peak discharge were aligned to be able to accurately investigate the hysteresis patterns and event sediment yields.

The sediment concentration profile was calculated using the Rouse Equation (Chang, 1988):

$$\frac{C}{C_a} = \left(\frac{D-z}{z} * \frac{a}{D-a}\right)^{z*} \tag{3.4a}$$

$$z_* = \frac{w_s}{KU_*} \tag{3.4b}$$

$$w_s = \frac{RgD^2}{18v+(0.75RgD^3)^{0.5}} \text{ (Bright et al., 2018; Ferguson \& Church, 2004)} \tag{3.4c}$$

where, w_s is the settling velocity (m/s), R is the ratio of fluid to particle density (unitless), D is the particle diameter (m), v is the kinematic viscosity of water (m/s^2), K is VonKarman's constant (unitless), and g is the acceleration due to gravity (m/s^2). The average particle diameter was determined as a function of turbidity, for each time step, using a turbidity-D50 particle size relationship found from our analysis of ISCO samples.

After both profiles had been found and the suspended sediment discharge per unit width was calculated for each time step, the data was multiplied by the channel width to report the sediment flux at each time step. Then the sediment fluxes were summed and

multiplied by the time step (15 minutes or 900 seconds) to produce sediment yields for individual events.

To compare sediment yields using this methodology to typical methodologies used in the literature, the annual sediment yield for the 2019 calendar year was estimated using both the continuous model and a modified sediment rating curve approach. Due to hysteretic relationship between suspended sediment and discharge, separate rating curves were generated for the rising and falling limb of the hydrographs, which is consistent with methods used in Appalachian sediment transport studies (Bolstad et al. 2006). The curves were derived from hourly paired sediment flux and discharge measurements. The sediment flux measurements were found from the continuous model and discharge measurements were calculated using the area weighted method mentioned previously. The paired data was separated in to respective rising and falling limb datasets and a unique power function was fit to each set. The power functions were used to predict concentrations from 15-minute discharge data, the rising limb function was used when discharge rates were increasing over time and falling limb function was used when discharge rates were decreasing over time. The concentrations were transferred into mass fluxes and summed up to reach a total annual sediment yield measurement.

3.3.2 Storm Event Sediment Source and Pathway Analysis

Watershed sediment source and pathway dynamics were investigated through hysteresis and sediment unmixing analysis. Sediment transport hysteresis occurs due to the differences the timing of peak sediment concentrations and discharge. The analysis of the hysteretic loop patterns can be used determine the dominant sediment sources activated during an event. These loops can be further quantified using hysteresis indexing. The

hysteresis index allows for objective classification of the size and direction of the hysteresis loop. Source signals in the hysteresis loops can be used to unmix sediment sources and partition sediment yields into baseload and wash loads. These analytical methods were used to help understand the watershed sedimentation dynamics.

A storm event was defined as any hydrological response to precipitation that resulted in a rising and falling limb (Lloyd et al., 2016a). Events were identified by an increase in discharge by at least 20% above flowrate prior to the precipitation. The discharge can recede for long periods of time depending on the intensity of the storm, so the falling limb ended when the flowrate came within 5% of the initial flowrate on the rising limb. If another storm occurred before the discharge had the chance to return to prior flow conditions, the falling limb ended at the lowest flowrate before the discharge began to increase again. Hysteresis analysis was performed with discharge and suspended sediment concentration for each of the 19 storm events at the upstream site. Hysteresis is based on the response time of discharge and sediment concentration, so the flowrate timing was adjusted for each event individually so that the peak discharge and the peak flow depth occurred simultaneously. Sediment concentration was plotted based on the change in discharge and unique hysteresis loops were created for each event.

Regarding categorization, we classified hysteresis loop shapes in to five defined types based on Williams (1989). Class I is a single-valued line that occurs when the ratio of concentration (*C*) to discharge (*Q*) is approximately equal on the rising (*r*) and falling (*f*) limb of the storm ($\frac{C_r}{Q_r} \cong \frac{C_f}{Q_f}$) . Single line hysteresis suggests that there is a non-rate-limiting supply of a single sediment source. Class II is a clockwise loop that occurs when

the concentration-discharge ratios on the rising limb are greater than the falling limb ($\frac{C_r}{Q_r} > \frac{C_f}{Q_f}$ for all values of Q). Clockwise hysteresis is caused by more rapid increases in sediment concentration than increases in discharge resulting in a 'flushing' of sediment and suggests a source close to the watershed monitoring station that is supply limited. Class III is a counterclockwise loop that occurs when the concentration-discharge ratios on the rising limb are less than those on the falling limb ($\frac{C_r}{Q_r} < \frac{C_f}{Q_f}$ for all values of Q). Counterclockwise hysteresis is caused by more rapid increases in discharge than increases in sediment concentrations and suggest a sediment source located higher up in the watershed. Class IV is a single line plus a loop that occurs when the concentration-discharge ratios for one range of discharge values is the same on the rising and falling limbs but the concentration discharge ratios for another range of discharge values are not the same on the rising and falling limbs. This suggests a change in the availability, storage, or transportability of sediment during the event. Class V is a figure eight that occurs then the concentration-discharge ratios for one range of discharge values is greater on the rising limb than the falling limb and the concentration-discharge ratios for another range of discharge values are greater on the falling limb than the rising limb ($\frac{C_r}{Q_r} > \frac{C_f}{Q_f}$ for one range of Q values and $\frac{C_r}{Q_r} < \frac{C_f}{Q_f}$ for another range of Q values). Like Class IV, this also suggests a change in sediment availability, storage, or transportability during the event (Lloyd et al., 2016a).

The size and shape of hysteresis loops can be quantified using a hysteretic index. There are several indices to describe the shape and direction of the hysteresis loop

(Butturini et al., 2008; Langlois et al., 2005; Lawler et al., 2006; Lloyd et al., 2016a) but the method purposed by Lloyd et al. (2016a) was used to determine the hysteresis index for each event loop. First the event flowrates and the sediment concentrations are normalized using the following equations:

$$Normalized\ Q_i = \frac{Q_i - Q_{min}}{Q_{max} - Q_{min}} \tag{3.5a}$$

where Q_i is the discharge at timestep i, Q_{min} is the minimum event flowrate, and Q_{max} is the maximum event flowrate.

$$Normalized\ C_i = \frac{C_i - C_{min}}{C_{max} - C_{min}} \tag{3.5b}$$

where C_i is the turbidity at timestep i, C_{min} is the minimum event turbidity, and C_{max} is the maximum event turbidity. The normalization of concentration and flowrate allow for the comparison of events with different magnitudes. The hysteresis index is calculated using the following equation:

$$HI_{Qi} = C_{RL-Qi} - C_{FL-Qi} \tag{3.5c}$$

where HI_{Qi} is the index at percentile i of discharge Q, C_{RL-Qi} is the turbidity on the rising limb at percentile i of Q, and C_{FL-Qi} is the turbidity on the falling limb at the equivalent discharge point. The percentiles of discharge were calculated using the following equation:

$$Q_i = k(Q_{max} - Q_{min}) + Q_{min} \tag{3.5d}$$

where k is the discharge percentile. The hysteresis index was calculated for every 5% change in discharge, so k was equal to 0.05, 0.1, 0.015…0.95. The hysteresis index ranges from -1 to 1 and the sign of the index indicates the direction of the loop (negative is

counterclockwise and positive is clockwise) and the number represents the thickness of the loop (Lloyd et al., 2016a). To further quantify the sources and transport processes occurring during each event, a method proposed by Megnounif et al. (2013) was used to estimate the contributions from two different classifications of sources. The total suspended sediment yield (Y_S) for each event is given by:

$$Y_S = Y_{S1} + Y_{S2} \approx \sum_{j=0}^{N} \left(\frac{C_j Q_j + C_{j+1} Q_{j+1}}{2}\right)\left(t_{j+1} - t_j\right) * 10^{-3} \quad (3.6a)$$

where Q_j is the discharge (m^3/s) at time t_j, C_j is the sediment concentration (g/L) at time t_j, and N is the number of measurements for the event. Y_{S1} is classified as the base load and represents sediment production from weathering processes occurring in the stream network, such as streambed, bank and gully erosion. Y_{S2} is classified as the wash load and represents the supply of new sediment sources that become available, such as material from uplands, bank caving, and re-suspension of fresh deposits within the stream network (Megnounif et al., 2013).

The type of hysteresis loop observed for each event can be used to identify sediment sources by decomposing the loops into a series of stages to enable the estimation of the contributions of the Y_{S1} and Y_{S2} components. The number of stages is dependent upon the hydrograph and loop type (Figure 3.6) and a specific sediment rating curve was defined for each stage and expressed as the function:

$$C_k^i(t_j) = f_{ik}(Q_j) \quad (3.6b)$$

where i refers to the class type (I-VI) and k refers to the stage number (1-5).

Class I is a single valued line and suggests that suspended sediment concentration is heavily dependent upon discharge. This relationship is typically associated with an uninterrupted supply of sediment throughout the event (Williams, 1989) and depends more on the entrainment of channel bed material than on the supply of hill slope sediments (Walling and Webb, 1982; Probst and Bazerbachi 1986; Hudson, 2003; Megnounif et al., 2013). In class I, the sedigraphs and hydrographs peak at the same time so this class is comprised of two stages in the C-Q relationship: in stage one the sediment concentration and the discharge rate both increase and in stage two the sediment concentration and the discharge rate both decrease. The sediment is supplied during stage one and can be expressed by the function $C_1^I(t_j) = f_{I1}(Q_j)$. In this class $Y_S \approx Y_{S1}$ and was estimated by:

$$Y_{S1} \approx \sum_{j=0}^{N} \left(\frac{f_{I1}(Q_j)Q_j + f_{I1}(Q_{j+1})(Q_{j+1})}{2} \right) (t_{j+1} - t_j) * 10^{-3} \quad (3.6c)$$

Class II is a clockwise loop and suggests a depletion of available sediment in the stream channel or catchment (Peart and Walling, 1982). In class II, the sedigraph peaks before the hydrograph creating three stages in the C-Q relationship. The first stage is characterized by a sharp increase in concentration with an increase in discharge representing the mobilization of temporarily stored sediment (Walling and Webb, 1981) or the wash-load transported by the first surface runoff at the beginning of the event (Rovira and Batalla, 2006, Megnounif et al., 2013). The second stage is characterized by a decrease in concentration with a continual increase in discharge representing a depletion of sediment within the channel system. The third stage is characterized by a decrease in both concentration and discharge representing the loss of energy in the system. The majority of stored and easily mobilized sediment gets evacuated during the rising limb of the

hydrograph leading to a depletion of the Y_{S2} component (Megnounif et al., 2013). The sediment left in the third stage is assumed to be derived from the channel network (Walling and Webb, 1982). The function of the Y_{S1} component is expressed as $C_3^{II}(t_j) = f_{II3}(Q_j)$ and was extended to the previous two stages allowing for the Y_{S1} component to be estimated by:

$$Y_{S1} \approx \sum_{j=0}^{N} \left(\frac{f_{II3}(Q_j)Q_j + f_{II3}(Q_{j+1})(Q_{j+1})}{2}\right)(t_{j+1} - t_j) * 10^{-3} \quad (3.6d)$$

Class III is a counterclockwise loop and represents sediment supplied to the stream on the receding limb and can be caused by a sediment wave that travels slower than the discharge wave, high soil erodibility with prolonged erosion, bank caving, or sediment from distal sources (Williams, 1989; Megnounif et al., 2013). In class III, the hydrograph peaks before the sedigraph peaks creating three stages in the C-Q relationship. The first stage is characterized by an increase in concentration with a sharp increase in discharge representing the maximum erosive power of the flow. The second stage is characterized by a sharp increase in concentration and a decrease in discharge representing new sediment sources becoming available for transport (Megnounif et al., 2013). The third stage is a decrease in concentration and discharge representing the loss of energy in the system. The sediment supplied in the first stage is assumed to be dominated by sediment eroded from the stream channel and representative of Y_{S1}. The function of the Y_{S1} component is expressed as $C_1^{III}(t_j) = f_{III1}(Q_j)$ and was extended to the following two stages allowing for the Y_{S1} component to be estimated by:

$$Y_{S1} \approx \sum_{j=0}^{N} \left(\frac{f_{III1}(Q_j)Q_j + f_{III1}(Q_{j+1})(Q_{j+1})}{2}\right)(t_{j+1} - t_j) * 10^{-3} \quad (3.6e)$$

Class IV is a figure eight loop (note this is Class V by Williams' classifications discussed earlier) which combines class II and class III. In class IV, the sedigraph can have two peaks, one peaking before the hydrograph peaks and one peaking after the hydrograph peaks creating four stages. The first stage is characterized by increases in both concentration and discharge however concentration is changing at a higher rate. The second stage is characterized by a decrease in concentration but a continual increase in discharge. The first and second stage represent the beginning of a clockwise loop. The third stage is characterized by an increase in concentration but a decrease in discharge representing new sediment sources becoming available (Megnounif et al., 2013). The fourth stage is characterized by a decrease in both concentration and discharge representing the loss of energy in the system. The third and fourth stage represent counterclockwise hysteresis. The initial partial clockwise hysteresis is caused by the mobilization of temporarily stored sediment and the wash-load transported by the first surface runoff at the beginning of the event. These sources become depleted on the rising limb of the hydrograph, but new sources are connected to the channel network on the falling limb inducing a partial counterclockwise hysteresis. During extreme dry conditions, figure eights can occur in which the partial counterclockwise hysteresis precedes the partial clockwise hysteresis, but the methods for determining the Y_{S1} component remain the same (Gellis, 2013). None of these four stages represent the sediment derived from the channel network however, it can be assumed that between the initial discharge and the maximum discharge, the concentration relative to transport capacity increases linearly (Megnounif et al., 2013). A line can be used to join the points [Q_0, $C(Q_0)$] and [Q_{max}, $C(Q_{max})$] creating an artificial fifth stage that was used to estimate sediment derived from the channel network. The

function of the Y_{S1} component is expressed as $C_5^{IV}(t_j) = f_{IV5}(Q_j)$ and was extended to the entire event for the Y_{S1} component to be estimated by:

$$Y_{S1} \approx \sum_{j=0}^{N} \left(\frac{f_{IV5}(Q_j)Q_j + f_{IV5}(Q_{j+1})(Q_{j+1})}{2}\right)(t_{j+1} - t_j) * 10^{-3} \quad (3.6f)$$

Class V and VI are a single line plus one loop (note this is Class IV by Williams' classifications discussed earlier) which combines class I and either class II or III respectively. In class V, the sedigraph peaks before the hydrograph but parts of the rising and falling limbs of the hydrograph and sedigraph align creating four stages. The first stage is characterized by equal rates of change for concentration and discharge. The second stage is characterized by a greater increase in concentration than in discharge, but the discharge continues to increase. The third stage is characterized by a decrease in concentration but a continual increase in discharge. The fourth stage is characterized by equal rates of change for concentration and discharge. In class VI, parts of the rising and falling limbs of the hydrograph align, but the sedigraph peaks after the hydrograph creating four stages. Stages one and four remain the same as class V. Stage two is characterized by an increase in concentration but a decrease in discharge. Stage three is characterized by a greater decrease in concentration than in discharge but the discharge continues to decrease. Similar to class I, the synchronized stages (one and 4) represent the sediment derived from the channel network in classes V and VI (Megnounif et al., 2013). The function of the Y_{S1} component is expressed as $C_{1\&4}^{V}(t_j) = f_{V1\&4}(Q_j)$ or $C_{1\&4}^{VI}(t_j) = f_{VI1\&4}(Q_j)$ and was extended to the entire event for the Y_{S1} component to be estimated by:

$$Y_{S1} \approx \sum_{j=0}^{N} \left(\frac{f_{V1\&4}(Q_j)Q_j + f_{V1\&4}(Q_{j+1})(Q_{j+1})}{2}\right)(t_{j+1} - t_j) * 10^{-3} \quad (3.6g)$$

or

$$Y_{S1} \approx \sum_{j=0}^{N} \left(\frac{f_{VI1\&4}(Q_j)Q_j + f_{VI1\&4}(Q_{j+1})(Q_{j+1})}{2} \right) (t_{j+1} - t_j) * 10^{-3} \quad (3.6h)$$

In addition to the YS1 and YS2 unmixing analysis, the YS2 component was also decomposed. The YS2 component was often found to have two peaks, without an additional peak in flowrate. This suggests two separate sediment sources, source 1 that is activated earlier in the event and gets depleted before peak flow (YS2-a) and source 2 that is activated on the receding limb of the hydrograph (YS2-b). For events that had multiple sediment peaks and only one discharge peak, the YS2 component was separated at the local minimum between the two peaks. The YS2 sediment yield prior to the local minimum was considered source a and the YS2 yield after the minimum was considered source b.

3.3.3 Measuring Sediment Transport in Backwater Confluences

To assess sediment retention in the back-water confluence feature, we compared upstream and downstream sediment fluxes. Downstream sediment fluxes were estimated using an analogous approach to that described in section 3.3.1. The same TSS-turbidity power relationship used at the upstream site was used for the downstream monitoring station. A data driven model was developed in MATLAB (see Appendix D) to estimate sediment fluxes and yields from the concentrations measured at the two fixed-station monitoring platforms, as described in 3.3.1. The flowrates downstream at the confluence of the Ohio River and Fourpole Creek were estimated using a previously published HEC-RAS unsteady flow model (Jensen, 2018; Jensen and Ford, 2019). The flowrates at the upstream of the wetland were estimated using the area-weighted method and discharge measurements taken at a gauging site on Hurricane Creek, in a neighboring watershed. We

considered the uncertainty in lag times for the upstream flow boundary conditions in order to estimate uncertainty in sediment fluxes at the downstream monitoring station (given the HEC-RAS model requires continuous inputs). As mentioned, peak discharge was found to lag depth by 45 minutes to 5 hours with a mean lag of 2.5 hours. The impact of discharge lag time on sediment yields were investigated but ultimately the lag time did not have a large impact on the sediment yield results at the downstream site. A uniform 2.5-hour discharge lag was assumed, and the discharge data was adjusted accordingly prior to sediment flux calculations.

Sediment fluxes into and out of the system as well as depositional yields in the floodplain were investigated on an event and annual basis. The nineteen events investigate in sections 3.3.1-3.3.2 were examined from September 2018 to December 2019. Sediment fluxes were calculated at the upstream and downstream site at a 15-minute interval. Since the downstream site is often subject to backwater from the Ohio River during events, fluxes measured during negative flowrates were considered to be inputs ($Qssin_{down}$) into the tributary-wetland system and fluxes measured during positive flowrates were considered outputs ($Qssout_{down}$) of the system. The fluxes into the wetland at the upstream site were always considered as inputs ($Qssin_{up}$). Net retention in the control volume was estimated using a mass-balance for the system:

$$Net\ Retention = Qssin_{up} + Qssin_{down} - Qssout_{down} \tag{3.7}$$

3.3.4 Modeling Sedimentation with Confluence Floodplains

While measurements provide insights into cumulative net retention of sediment in the confluence floodplain, we were interested in longitudinal distributions and the impacts

of sediment hysteresis on sedimentation dynamics. Figure 3.7 summarizes the conceptual model for sedimentation dynamics in the backwater confluence floodplains. A 1-D HEC-RAS unsteady flow model was used to acquired flow inputs at the outlet and several cross sections along the tributary. The confluence floodplain wetland channel geometry was simplified into five reaches and reach wide hydraulic parameters were calculated (Figure 3.8). Sediment inputs at the boundary conditions are explicitly measured and include tributary loadings from the upstream monitoring site and backwater sediment loadings from the downstream monitoring site during hydrologic events on the Ohio River. Internal sediment sources may be considered static or dynamic and include unconsolidated streambed material, streambank material, and unconsolidated fresh floodplain deposits. The model was evaluated by comparing measured and modeling sediment loads at the watershed outlet.

3.3.4.1 Modeling Sedimentation with Confluence Floodplains

A mass balance of suspended sediment serves as the basis for modeling and is simulated using a 1-D formulation that considers erosion, deposition, and advective inputs and outputs (e.g., Russo and Fox, 2012) and were simulated separately for the floodplain and the stream channel. The finite difference approximation to the governing sediment mass balance for the stream (SS_s) and floodplain (SS_f) are simulated as:

$$SS_{s_i}^{\ j} = SS_{s_{i-1}}^{\ j} + E_{b_i}^{\ j} + Q_{ssin-s_i}^{\ j}\Delta t - Q_{ssout-s_i}^{\ j}\Delta t \quad (3.8a)$$

$$SS_{f_i}^{\ j} = SS_{f_{i-1}}^{\ j} + E_{f_i}^{\ j} - D_{f_i}^{\ j} + Q_{ssin-f_i}^{\ j}\Delta t - Q_{ssout-f_i}^{\ j}\Delta t \quad (3.8b)$$

where, i is the temporal index, j is the reach index, q is the erosion source index, s and f represent the stream and floodplain compartments, respectively, E is the mass eroded from

the specified source (kg), *D* is the mass deposited (kg), Q_{ssin} is the mass flux of sediment into the control volume (kg/s), Q_{ssout} is the mass flux out of the control volume (kg/s), and Δt is the timestep (s). Erosional sources include streambank sediments and floodplain deposits. We simulate erosion considering shear, supply and transport capacity limitations.

$$E_{b_i}^{\ j} = \min\left[a_b\left(\tau_{f_{b_i}}^{\ j} - \tau_{cr_b}\right)^{b_b} SA_{b_i}^{j}\Delta t,\ T_{c_{b_i}}^{\ j} - SS_{s_{i-1}}^{\ j}, S_{b_{i-1}}^{\ j}\right] \quad (3.9a)$$

$$E_{f_i}^{\ j} = \min\left[a_f\left(\tau_{f_{f_i}}^{\ j} - \tau_{cr_f}\right)^{b_f} SA_{f_i}^{j}\Delta t,\ T_{c_{f_i}}^{\ j} - SS_{f_{i-1}}^{\ j}, S_{f_{i-1}}^{\ j}\right] \quad (3.9b)$$

where, a is the erodibility of the source material, b is the exponent for the erosion equation, τ_f is the shear stress of the fluid at the centroid of the erosion source (Pa), τ_{cr} is the critical shear stress of the erosion source (Pa), SA is the surface area of the erosion source (m^2), Tc is the transport carrying capacity of the fluid (kg), and S is the sediment supply (kg). Shear stress was estimated for both floodplain and stream compartments as $\tau = \gamma R S_f$.

The bulk transport carrying capacity was estimated for the stream and floodplain separately as follows:

$$T_{c_s\ i}^{\ j} = C_{tc_s}\left(\tau_{f_{s_i}}^{\ j}\right)^{1.5} L_s\Delta t \quad (3.10a)$$

$$T_{c_f\ i}^{\ j} = C_{tc_f}\left(\tau_{f_{f_i}}^{\ j}\right)^{1.5} L_f\Delta t \quad (3.10b)$$

where Tc is average transport carrying capacity across the reach at a timestep (kg), C_{tc} is a calibration coefficient ($m^{1/2}\cdot s^2/kg^{1/2}$), τ_f is the shear stress of the fluid at the location of sediment source (Pa), and L_f and L_s are the lengths of the floodplain and stream reaches (m), respectively. Since transport capacity changes with the type of flow, a low calibration

coefficient was used for base flow and a high calibration coefficient was used for event flow. An individual threshold velocity was found for the stream and the floodplain in each reach to determine which coefficient to use at a given time step.

Depositional fluxes were only estimated for the floodplains since no net deposition occurs in the stream channel in this system. The floodplain depositional flux was estimated using the approach of Lauer and Parker (2008) which was developed to estimate depositional fluxes of suspended sediments for meandering channels when integrated across the extent of a stream reach as follows:

$$D_{f_i}^{\ j} = \frac{C_{f_i}^{j} Q_{f_i}^{j}}{\alpha B_f^{j^2} (1-\lambda_p)} \left[1 - \exp\left(-\frac{w_s \alpha B_f^{j^2}}{Q_{f_i}^{j}}\right)\right] S A_f \Delta t \tag{3.11}$$

where C_f is the suspended sediment concentration in the floodplain (kg/m^3), Q_f is the flowrate in the floodplain (m^3/s), α is the scaling coefficient in floodplain deposition function, B_f is the width of the floodplain (m), and λ_p is the sediment deposition porosity in the floodplain.

The mass flux ($Q_{ssin_i}^{\ j}$) is calculated as the product of flow and average concentration and is calculated at upstream nodes of each reach. This value can be positive or negative depending on the flow conditions at the nodes. Conversely $Q_{ssout_i}^{\ j}$ is calculated at the downstream nodes and can be also be positive or negative pending hydraulic conditions. Both Q_{ssin} and Q_{ssout} are calculated independently for the stream and floodplain based on the flowrates. We maintain separate mass balances for the stream and floodplain.

Calculation of fluxes requires continuous estimates of flowrates in the floodplain and stream channel. Consistent with the work of Lauer and Parker (2008) we used a simple

representation to partition the bulk flow into floodplain flow and channel flow. We assumed that the floodplain can be split into two separate zones of rectangular cross section including a channel and floodplain zone. Flow is solved in each zone according to a simple Manning's approximation. Flowrate in the stream channel and floodplain zones Q_s and Q_f, respectively, are fully specified by the respective channel and floodplain manning's coefficients n_s and n_f, channel and floodplain flow depths, d_s, d_f and reach average slopes $S_{f\text{-}s}$ and $S_{f\text{-}f}$, the following relations describe channel and floodplain momentum balance:

$$Q_{s_i}^{\ j} = \frac{1}{n_{s_i}^{\ j}} A_{s_i}^{\ j} R_{s_i}^{\ j\frac{2}{3}} S_{f_{s_i}}^{\ \ j\frac{1}{2}} \tag{3.12a}$$

$$Q_{f_i}^{\ j} = \frac{1}{n_{f_i}^{\ j}} A_{f_i}^{\ j} R_{f_i}^{\ j\frac{2}{3}} S_{f_{f_i}}^{\ \ j\frac{1}{2}} \tag{3.12b}$$

where A is area (m^2), R is hydraulic radius (m), and S_f is friction slope (m/m).

Source supply mass-balances are estimated using a mass-balance as follows for the streambank and floodplain sources:

$$S_{b_i}^{\ j} = S_{b_{i-1}}^{\ j} - E_{b_i}^{\ j} \tag{3.13a}$$

$$S_{f_i}^{\ j} = S_{f_{i-1}}^{\ j} + D_{f_i}^{\ j} - E_{f_i}^{\ j} \tag{3.13b}$$

Where, S is the supply (kg) for a given reach and is assumed infinite for the banks. Based on the depositional and erosional fluxes, we also calculated the change in elevation of the floodplain. As discussed in the model calibration and evaluation section the stream channel was in quasi-equilibrium based on field observations over the 2017-2019 years at our study site.

3.3.4.2 Model Discretization, Inputs, and Parameterization

To apply the sediment transport model to the Fourpole Creek floodplain wetland, we coupled unsteady hydrodynamic modeling with the sediment mass-balance formulation. Regarding the hydrodynamic modeling, the unsteady, non-uniform nature of mixing from the river and tributary channels required the use of HEC-RAS. HEC-RAS has the ability to perform both 1-D and 2-D unsteady flow analysis. The relative accuracy of using a 1-D or a 2-D modeling approach for a specific application is highly debatable (Gibson, 2016). There are some situations where 2-D modeling can produce more accurate results than 1-D modeling but there are also situations in which 1-D modeling can produce equal or even better results. There are a large range of situations that fall into this grey area, but professionals have developed a general rule to determine if a 2-D model is necessary: if the length-to-width ratio of the modeled reach is larger than 3:1, a 1-D model is appropriate and will likely be able to represent the lateral expansion of flow. For the modeled reach of Fourpole Creek, the length-to-width ratio was found to be 4:1 in the areas with the widest floodplain and for the rest of the reach the ratio was found to be much higher (Jensen and Ford, 2019). The HEC-RAS 2-D modeling user's manual outlines situations in which 2-D modeling can provide better results than 1-D modeling including leveed systems, highly braided streams, bays and estuaries (where flows are coming from multiple locations and times), alluvial fans, and flow around abrupt bends. The 1-D model represents the 2-D flow dynamics in both the streamwise and lateral directions however it assumes that the primary direction of flow occurs along the channel. After careful consideration, a 1-D model was deemed appropriate for this site.

A previously published 1-D unsteady flow HEC-RAS model was used to simulate the flow conditions over the time period needed for this study. The model was originally developed using LiDAR data to delineate both the floodplain and the stream channel with right and left bank edges. Thirty-one cross sections were created at regular intervals along the modeled reach. The more cross sections that are created in HEC-RAS the more accurate the flow results are, however, thirty-one small reaches in the sediment model was not manageable or necessary for computation of the sediment transport model. For simplification purposes, the entire modeled reach was broken down into five smaller reaches. Each small reach consisted of six cross-sections with the fifth reach consisting of seven (Figure 3.8). The channel widths, floodplain widths, and bank heights for each of the six cross sections within each small reach were averaged. The averaged values for each of the three geometry parameters was assumed to be constant throughout the small reach. In addition, the channel and floodplain geometry was simplified to a rectangular shape (Figure 3.8) where d represents the flow depth, h represents the bank height, w represents the channel width, and B represents the floodplain width (assumed to be equal for both over banks).

The HEC-RAS model has the capability to output time series results of individual parameters at all thirty-one cross sections specified in the model geometry. Time series data sets were generated from the unsteady flow model results for the following parameters which are relevant to our sediment transport model:

A Total area of cross section active flow

Q Total flow in the total cross section

R Hydraulic radius for the total cross section

n Manning's n value for the total cross section

n_c Conveyance weighted Manning's n for the main channel

n_L Conveyance weighted Manning's n for the left overbank

n_R Conveyance weighted Manning's n for the right overbank

Manning's n-values represent the roughness of the flow path in the channel and floodplain. Individual Manning's n values were assigned at each cross section at each time step based on land use classifications that the cross sections intersected.

HEC-RAS has the ability to generate time series data sets for friction slope in addition to the parameters listed above, but due to rounding error within the software, the friction slopes were calculated outside of the program with the parameters extracted from the model results by using a simple variation of Manning's equation:

$$S_f = \left(\frac{Qn}{AR^{\frac{2}{3}}}\right)^2 \tag{3.14}$$

The calculated friction slope was used as the friction slope for both the stream channel and the floodplain.

A series of equations were used to find three unknown parameters: flow depth (d), flow rate in the stream channel (Q_s), and flow rate in the floodplain (Q_f) at the upstream and downstream node of each reach.

$$Q_{s_i}^{\ j} = \frac{1}{n_{s_i}^{\ j}}(w^j d_i^j)\left(\frac{w^j d_i^j}{w^j + 2d_i^j}\right)^{\frac{2}{3}}(S_{f_i}^{\ j})^{\frac{1}{2}} \quad \text{when d < h} \tag{3.15a}$$

$$Q_{s_i}^{\ j} = \frac{1}{n_{s_i}^{\ j}}(w^j d_i^j)\left(\frac{w^j d_i^j}{w^j + 2h^j}\right)^{\frac{2}{3}}(S_{f_i}^{\ j})^{\frac{1}{2}} \quad \text{when d > h} \tag{3.15b}$$

$$Q_{f_i}^{\ j} = \frac{1}{n_{f_i}^{\ j}}(2B^j(d_i^j - \mathrm{h^j}))\left(\frac{(2B^j(d_i^j - \mathrm{h^j}))}{2B^j + 2(d_i^j - \mathrm{h^j})}\right)^{\frac{2}{3}}(S_{f_i}^{\ j})^{\frac{1}{2}} \quad \text{when d > h} \tag{3.15c}$$

$$Q_{T_i}^{\ j} = Q_{s_i}^{\ j} + Q_{f_i}^{\ j} \tag{3.15d}$$

Given the system of equations, an iterative routine was written to solve for the floodplain flow rate, stream flow rate and flow depth simultaneously. Initially, the depth was guessed to be extremely small and equation 3.14a was solved to find the stream flow rate. If the stream flow rate was not equal to the known total flow rate, d was increased, and the stream flow rate was recalculated until the stream flow rate was equal to the total flow rate or the depth was greater than the bank height. If the flow depth became greater than the bank height, equation 3.14b was used to calculate the stream flow rate because the wetted perimeter term of the stream channel reached the maximum value and no longer increases with each increase in depth. Similarly, equation 3.14c was used to calculate the floodplain flow rate and the depth continues to increase until the sum of the stream flow rate and the floodplain flow rate were equal to the total flow rate (equation 3.14d).

Once the flow depth at the upstream and downstream nodes of each reach had been found, a reach wide volumetric water balance was used to find an average reach depth. An initial stream volume was assumed for each reach and subsequent volumes for each time step were calculated using the flowrates at the nodes upstream and downstream of the reach:

$$V_{T_i}^{\ j} = V_{T_{i-1}}^{\ j} + Q_{T_i}^{\ j}\Delta t - Q_{T_i}^{\ j+1}\Delta t \tag{3.16a}$$

$$V_{s_i}^{\ j} = V_{s_{i-1}}^{\ j} + Q_{s_i}^{\ j}\Delta t - Q_{s_i}^{\ j+1}\Delta t \tag{3.16b}$$

$$V_{f_i}^{\ j} = V_{f_{i-1}}^{\ j} + Q_{f_i}^{\ j}\Delta t - Q_{f_i}^{\ j+1}\Delta t \tag{3.16c}$$

From the reach volume in the stream and the floodplain respectively, an average depth for each reach was found using:

$$d_{s_i}^{\ j} = \frac{V_{s_i}^{\ j}}{SA_s^j} \tag{3.17a}$$

$$d_{f_i}^{\ j} = \frac{V_{f_i}^{\ j}}{SA_f^j} \tag{3.17b}$$

Due to the simplification of the channel and floodplain geometry and the abrupt geometry change from reach to reach, the water surface in the channel and the floodplain were often disconnected. Another iterative process was used to adjust the depth in the stream and floodplain simultaneously until water surface continuity between the two partitioned areas was achieved. The floodplain and stream volumes were recalculated from the final depth and total volume was used to ensure volume conservation. The difference in the final stream volume and the stream volume prior to the depth adjustment was considered the exchange volume. If the exchange volume was positive, water moved from the floodplain into the stream and conversely if the exchange volume was negative, water moved from the stream into the floodplain. With the movement of water also comes movement of suspended sediments. The floodplain and stream can have different suspended sediment concentrations so the volume of water being exchanged and the suspended sediment concentration of the section the water was being exchanged from was used to find the lateral mass input of sediment being transferred.

Suspended sediment fluxes at the boundaries of the control volume included inputs from the upstream Fourpole Creek source and the downstream Ohio river source. The data

driven sediment flux model was used to determine the sediment fluxes into the first reach and out of the fifth reach from the continuous turbidity measurements taken at the upstream and downstream monitoring stations. Due to the oscillating flow conditions at the end of reach five, the fluxes during negative flows were boundary condition inputs and fluxes during positive flows were outputs used for model calibration and validation.

3.3.4.3 Model Evaluation Procedure

Several variables in the modeling equations vary from system to system and needed to be calibrated for this site specifically. Each unknown parameter was manually adjusted within an individual range of reported literature values (see Table 3.2). Calibration was performed for 240 days randomly selected throughout the year and the remaining 116 days were used for validation. There were nine days where backwater conditions occurred at the outlet for the entire day so these could not be used for calibration or validation. Nash Sutcliffe efficiency (NSE) and percent bias (PBIAS) model statistics were calculated for each manual calibration run and the parameter adjustment ended when acceptable model statistics were achieved.

The NSE statistic is calculated as follows:

$$\mathrm{NSE} = 1 - \frac{\sum_{i=1}^{n}\left(SSC_{obs_i} - SSC_{model_i}\right)^2}{\sum_{i=1}^{n}\left(SSC_{obs_i} - \overline{SSC_{obs}}\right)^2} \tag{3.18a}$$

The NSE statistic was chosen because it works well for continuous long-term modeling and can determine how well the model simulates trends (Moriasi et al., 2015). Additionally, it is commonly used in the sediment transport field so there are reported threshold values for satisfactory, good, and excellent model performances (Moriasi et al., 2015). NSE values

can range between negative infinity and 1, with 1 indicating that your modeled data is identical to the observed data. Model runs that resulted in an NSE of 0.6 or higher were considered to do a good job of representing the sediment fluxes out of the system. This threshold was chosen based on reported NSE values for sediment models from Moriasi et al., 2015.

The PBIAS statistic indicates the model's tendency to over or under predicted the measured data and is calculated using the following:

$$\text{PBIAS} = 100 * \frac{\sum_{i=1}^{n}(SSC_{model_i} - SSC_{obs_i})}{(\sum_{i=1}^{n} SSC_{obs_i})} \quad (3.18b)$$

The PBIAS statistic was chosen as a second model performance indicator because it is a clear indicator of poor model performance (Moriasi et al., 2015). PBIAS values can range from -100% to 100% with 0% being the best value. The positive values indicate that the model is underestimating, and the negative values indicate that the model is overestimating. A PBIAS of ±10% indicates that the model is doing a good job at balancing the over and under predictions. This threshold was chosen based on reported PBIAS values for sediment models in Moriasi et al., 2015.

3.3.5 Implications for Particulate Nitrogen Yield

Bright et al., (2018) found turbidity to be a strong surrogate for predicting particulate organic matter. The measured particulate organic matter content and the corresponding turbidity measurements were compiled and plotted against one another such that turbidity could be used to predict the percent POM. At low turbidities the percent POM can vary because of heterogeneities in suspended solids composition, but as turbidity increases the variability in the percent POM greatly decreases. To account for this trend,

average POM contents for specified turbidity ranges were integrated into the data driven sediment model to estimate POM yield.

Suspended sediment trap samples were analyzed on a combustion analyzer to determine the POC/POM ratio. The sediment trap samples were weighed, subsampled, and wet sieved through a 53µm sieve with deionized water. The wet sieved liquid was centrifuged and freeze dried before it was grinded using a Wig-L-Bug and sent to the Kentucky Stable Isotope Geochemistry Laboratory for further inorganic C removal and elemental analysis (see Ford et al., 2020). The carbon content of particulate organic matter was highly variable. Based on previously published results, sediment traps suggest C contents of 2.9% at high flow conditions (Ford et al., 2020). When comparing this the average POM concentration of 9.55%, our results suggest that 28% of POM is organic C. Others report the carbon content of particulate organic matter to be between 45% and 50% by mass (Moody et al., 2013). A high value of 50% and a low value of 28% were used to predict the carbon content of the particulate organic matter. To estimate particulate N fluxes, an average C:N ratio from the sediment trap data of 9.8 was used to predict the particulate nitrogen content. Particulate N loadings at upstream and downstream monitoring stations were estimated as follows.

$$PN_{min} = \left(\sum_{i=1}^{n} POM(i)\right)\frac{0.28}{9.8} \quad (3.19a)$$

$$PN_{max} = = \left(\sum_{i=1}^{n} POM(i)\right)\frac{0.5}{9.8} \quad (3.19b)$$

where the percentage of the particulate organic matter in the suspended sediment varies as a function of turbidity:

$$POM(i) = \begin{cases} 0.2625 * SS(i), & Turbidity(i) < 10 \\ 0.1581 * SS(i), & 10 < Turbidity(i) < 100 \\ 0.1116 * SS\ (i), & 100 < Turbidity(i) < 400 \\ 0.0955 * SS(i), & Turbidity(i) \geq 400 \end{cases} \quad (3.20)$$

where SS is the suspended sediment transported at timestep i.

3.4 Tables and Figures

Table 3.1. Defines soil codes in the legend of Figure 3.4.

Soil Code	Soil Name and Description
GxD	Gilpin-Upshur-Urban land complex, 15 to 25 percent slopes
CoB	Coolville silt loam, 3 to 8 percent slopes
Ud	Udorthents, smoothed
VuD	Vandalia-Urban land complex, 8 to 25 percent slopes
SrB	Sensabaugh loam, 3 to 8 percent slopes, rarely flooded
GuC	Gilpin-Upshur silt loams, 8 to 15 percent slopes
Gy	Guyan silt loam
Us	Urban land-Ashton-Lindside complex
AhC	Allegheny, bedrock substratum-Urban land complex, 3 to 15 percent slopes
CtB	Cotaco silt loam, 3 to 8 percent slopes
Ur	Urban land
VaD	Vandalia silt loam, 15 to 25 percent slopes
GuC3	Gilpin-Upshur complex, 8 to 15 percent slopes, severely eroded
Ca	Chagrin silt loam, 0 to 3 percent slopes, occasionally flooded
GlC	Gilpin silt loam, 8 to 15 percent slopes
Cm	Chagrin-Melvin silt loams, frequently flooded
W	Water
GlE	Gilpin silt loam, 25 to 35 percent slopes
UpC	Upshur silty clay loam, 8 to 15 percent slopes
GuD3	Gilpin-Upshur complex, 15 to 25 percent slopes, severely eroded
UwB	Urban land-Wheeling complex, 0 to 6 percent slopes
MoB	Monongahela loam, 3 to 8 percent slopes
Lm	Lindside silt loam, 0 to 3 percent slopes, occasionally flooded
BeD	Beech loam, 15 to 25 percent slopes
BeE	Beech loam, 25 to 35 percent slopes
UtD	Urban land-Gilpin-Upshur complex, 15 to 25 percent slopes
BuC	Beech-Urban land complex, 3 to 15 percent slopes
MuC	Monongahela-Urban land complex, 3 to 15 percent slopes
LgC	Latham-Gilpin complex, 8 to 15 percent slopes
UsB	Urban land-Ashton-Lindside complex, 0 to 8 percent slopes
SvC	Sensabaugh-Vandalia-Urban land complex, 3 to 15 percent slopes
GuF	Gilpin-Upshur silt loams, 35 to 70 percent slopes
GuE	Gilpin-Upshur complex, 25 to 35 percent slopes
GuD	Gilpin-Upshur complex, 15 to 25 percent slopes
Lo	Lobdell silt loam, 0 to 3 percent slopes, occasionally flooded
LlE	Lily sandy loam, 25 to 35 percent slopes
DoD	Dormont silt loam, loamy substratum, 15 to 25 percent slopes
SoA	Sensabaugh loam, 0 to 3 percent slopes, occasionally flooded

Table 3.2. Calibrated model parameters.

Parameters	Units	Description	Calibrated Model Value	Source
C_{tc_s} (High)	$\frac{m^{\frac{1}{2}} * s^2}{kg^{\frac{1}{2}}}$	Calibration coefficient for the transport capacity of the stream at high velocities	7.04 x 10^{-6}	6.00 x 10^{-6} - 1.20 x 10^{-4} Russo and Fox, 2012
C_{tc_s} (Low)	$\frac{m^{\frac{1}{2}} * s^2}{kg^{\frac{1}{2}}}$	Calibration coefficient for the transport capacity of the stream at low velocities	5.67	Manually adjusted during calibration
C_{tc_f} (High)	$\frac{m^{\frac{1}{2}} * s^2}{kg^{\frac{1}{2}}}$	Calibration coefficient for the transport capacity of the floodplain at high velocities	7.75 x 10^{-6}	6.00 x 10^{-6} - 1.20 x 10^{-4} Russo and Fox, 2012
C_{tc_f} (Low)	$\frac{m^{\frac{1}{2}} * s^2}{kg^{\frac{1}{2}}}$	Calibration coefficient for the transport capacity of the floodplain at low velocities	5.69	6.00 x 10^{-6} - 1.20 x 10^{-4} Russo and Fox, 2012
w_s	$\frac{m}{s}$	Mean settling velocity of suspended material	2.42 x 10^{-4}	1 x 10^{-5} - 5 x 10^{-4} Russo and Fox, 2012
τ_{cr_f}	Pa	Critical shear of the floodplain source	0.09	0.024 - 0.8 Russo and Fox, 2012
τ_{cr_b}	Pa	Critical shear of the streambank source	2.05	0.3 - 20 Russo and Fox, 2012
a_b	$\frac{kg}{Pa * m^2 * s}$	Erodibility of streambank source	9.85 x 10^{-5}	4.47 x 10^{-5} - 3.65 x 10^{-4} Russo and Fox, 2012
a_f	$\frac{kg}{Pa * m^2 * s}$	Erodibility of floodplain source	3.47 x 10^{-4}	2.24 x 10^{-4} - 1.29 x 10^{-3} Russo and Fox, 2012
α	*Unitless*	Scaling coefficient in floodplain deposition function	8	20 Lauer and Parker, 2008b
λ	*Unitless*	Sediment deposition porosity in the floodplain	0.38	0.35 Lauer and Parker, 2008b

Figure 3.1 West Virginia is located in the southeast region of the United States. The Fourpole Creek watershed is located in Wayne and Campbell counties in the southwestern part of the state

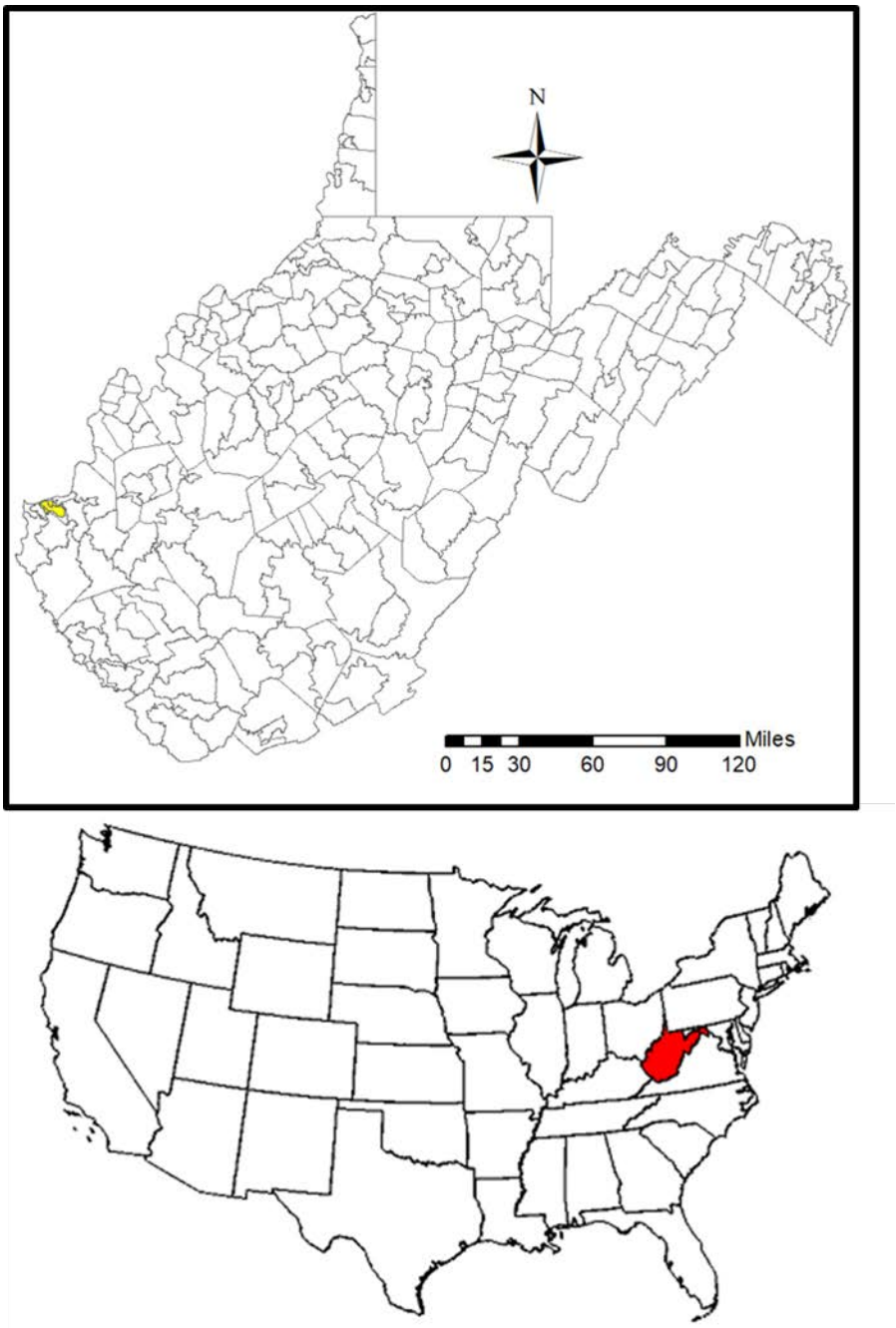

Figure 3.2 Slope in the Fourpole Creek watershed

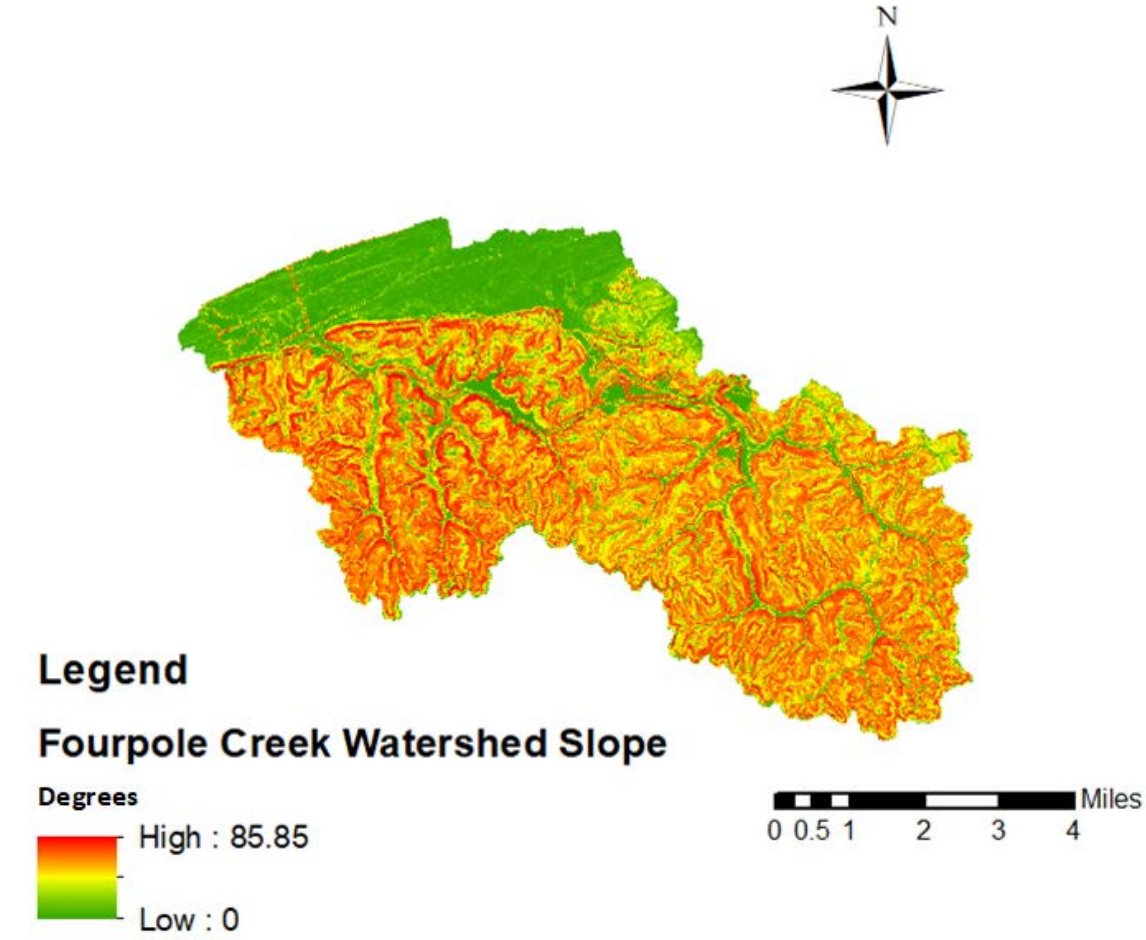

Figure 3.3. Land use in the Fourpole Creek watershed.

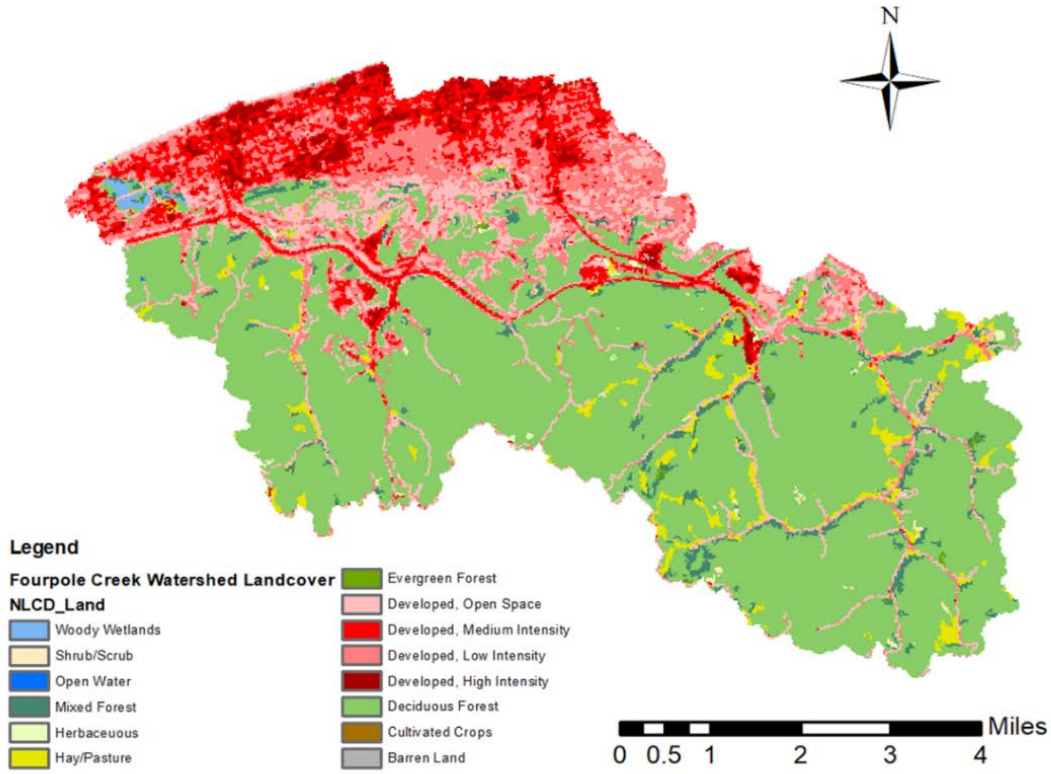

% OF WATERSHED AREA	LAND USE
0.23%	Woody Wetlands
0.18%	Shrub/Scrub
0.01%	Open Water
2.62%	Mixed Forest
0.21%	Herbaceuous
2.74%	Hay/Pasture
0.12%	Evergreen Forest
10.10%	Developed, Open Space
9.03%	Developed, Medium Intensity
12.73%	Developed, Low Intensity
2.53%	Developed, High Intensity
59.42%	Deciduous Forest
0.00%	Cultivated Crops
0.06%	Barren Lan

Figure 3.4. Soil types found in the Fourpole Creek watershed and confluence floodplain. The top figure portrays the soil types found along Fourpole Creek between the upstream and downstream monitoring stations.

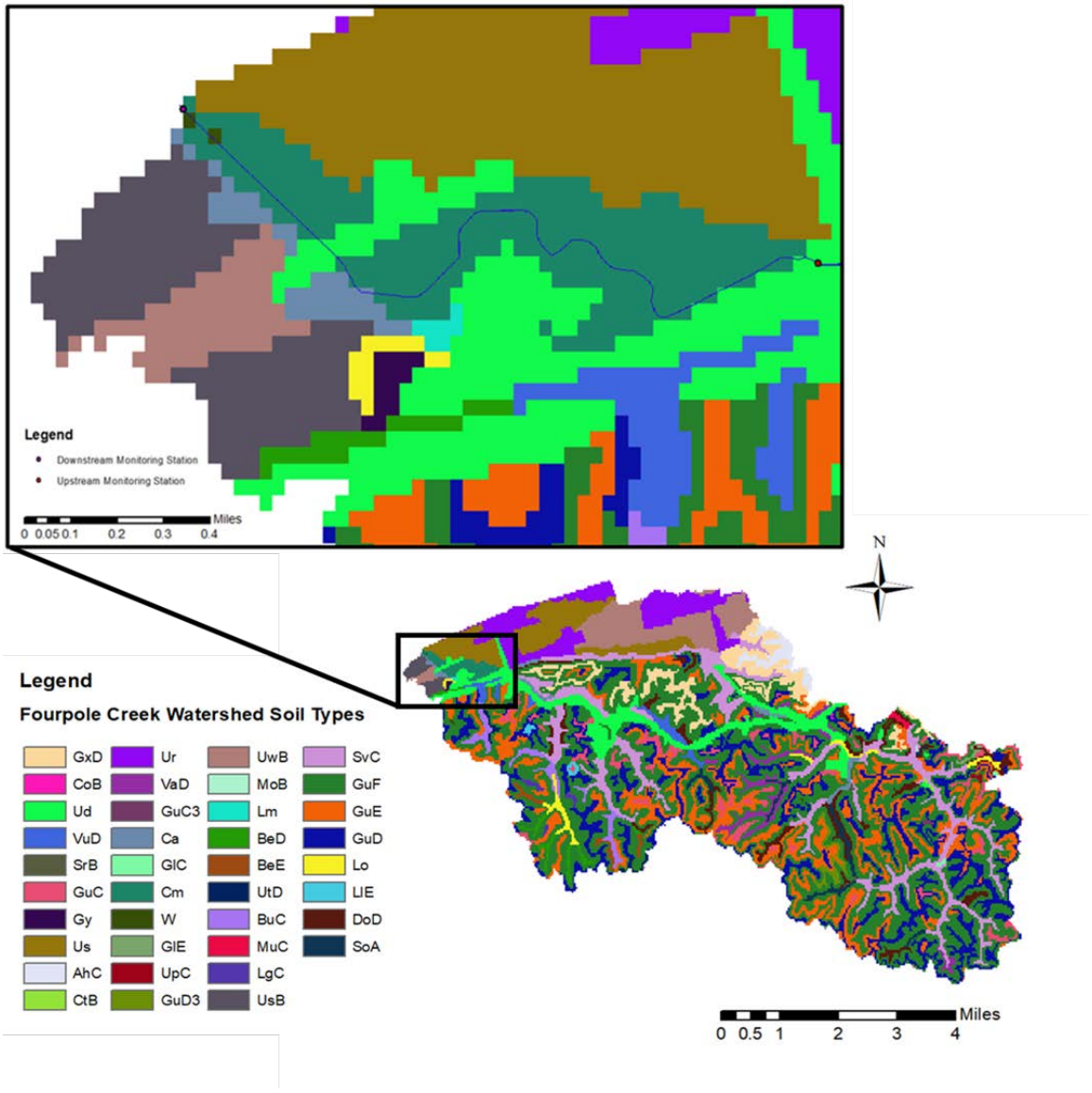

Figure 3.5. Two monitoring stations that are part of the NSF SENSE monitoring program. One is located upstream of the confluence floodplain wetland and the other is located downstream at the confluence of Fourpole Creek and the Ohio River.

Figure adapted from Jensen and Ford, 2019.

Figure 3.6. Hysteresis loop stage decomposition for unmixing baseload and wash load sediment sources as purposed by Megnounif et al., (2013).

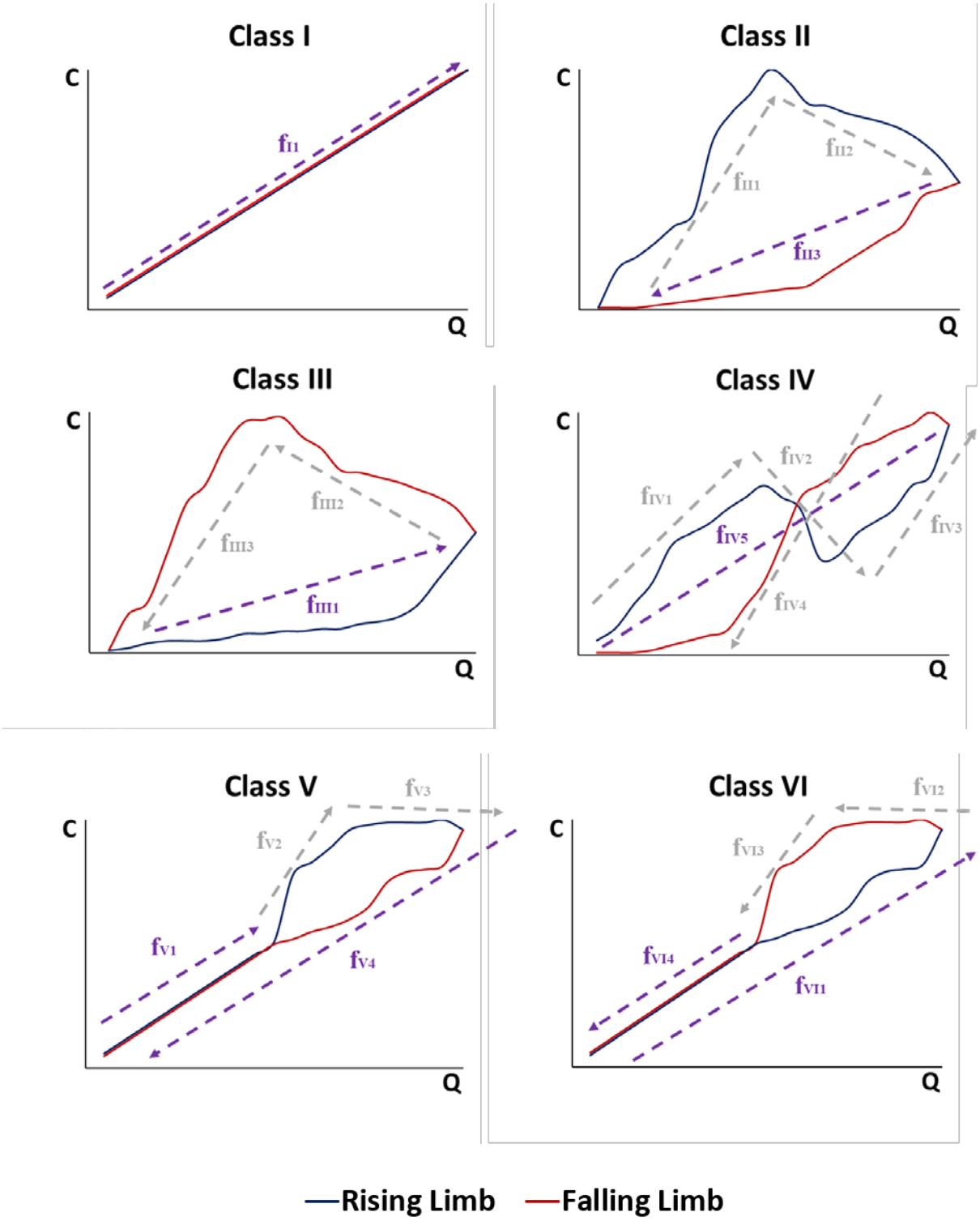

Figure 3.7. Conceptualization of Sediment Transport Model.

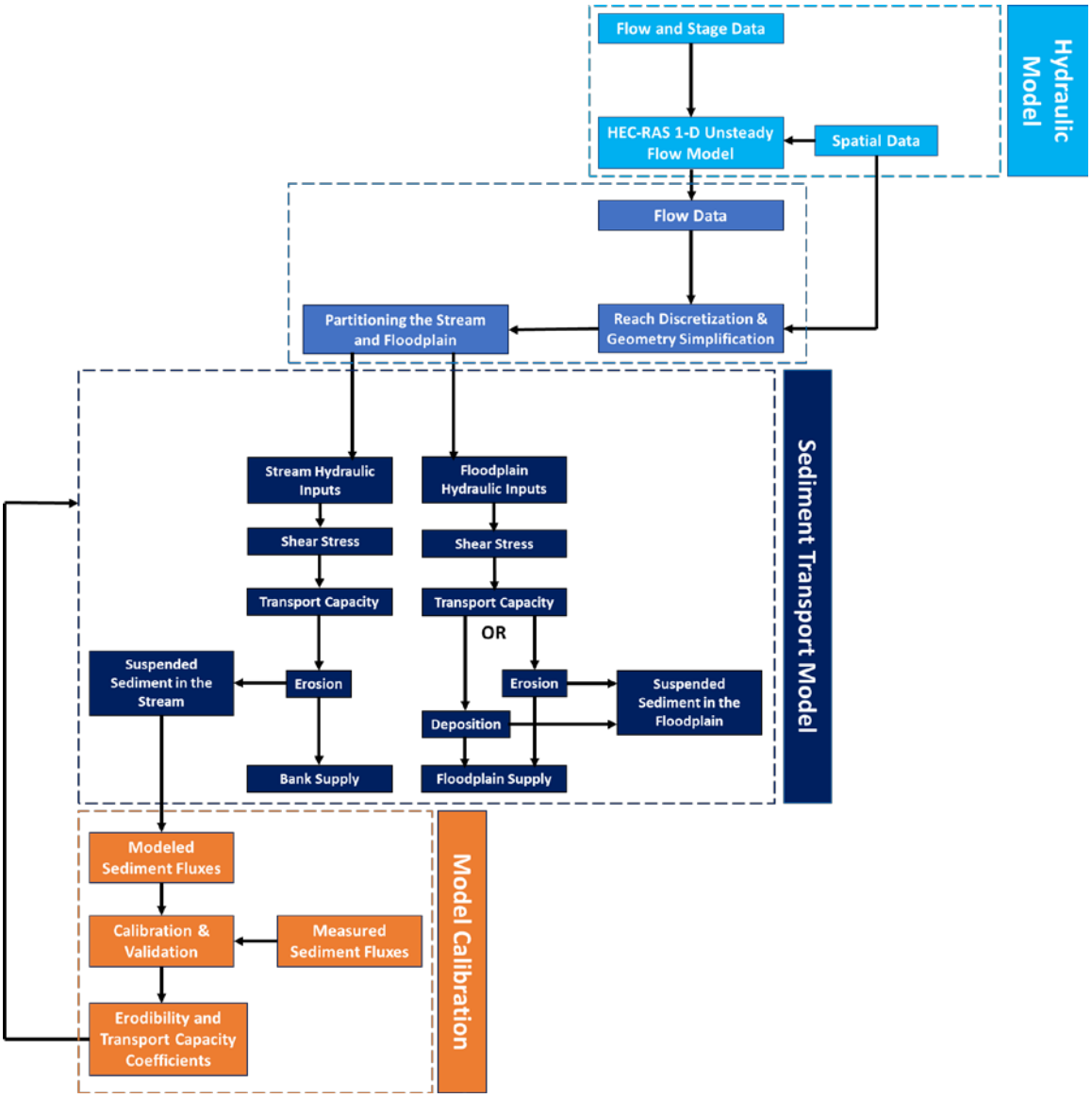

Figure 3.8. Reach discretization from H EC-RAS model and simplified cross section geometry.

	w	***h***	***B***
	Channel Width (m)	*Bank Height (m)*	*Floodplain Width (m)*
Reach 1	28.18	2.10	393.54
Reach 2	20.26	1.69	225.23
Reach 3	19.01	1.23	251.05
Reach 4	23.33	0.74	349.44
Reach 5	28.26	0.57	195.61

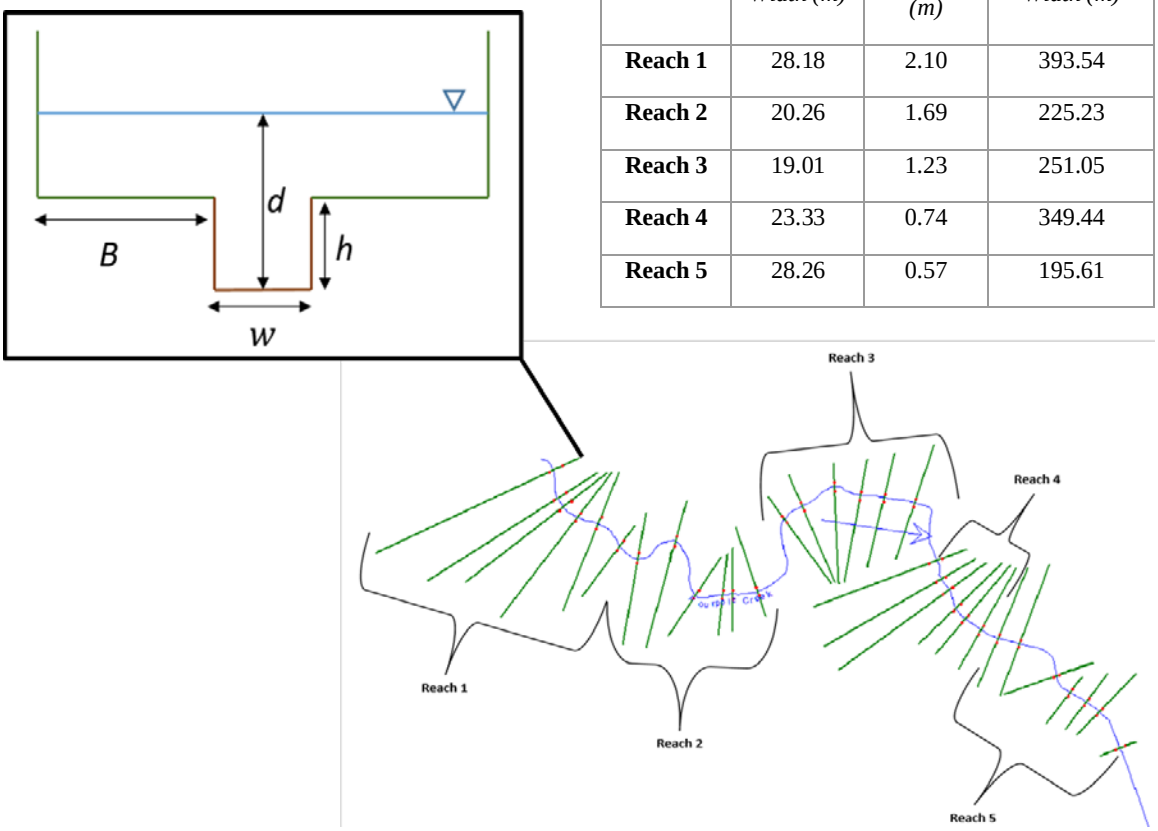

CHAPTER 4. RESULTS

4.1 Sediment Yield Measurements from Disturbed Appalachian Watersheds

4.1.1 SSC-Turbidity Calibration

Results of linear regression analysis on *in situ* SSC-turbidity calibrations highlight a significant relationship between log-transformed values of SSC and turbidity (Table 4.1; Figure 4.1). The simple linear regression performed between suspended sediment concentration and turbidity for in situ field measurements show that turbidity is a significant predictor with a P-value of 3.55×10^{-79} which is less than the alpha-level of 0.05 (Table 4.1). However, residual and normal probability plots for the simple linear regression were examined and it was determined that the assumptions for linear regression analysis were not met due to the lack of homoscedasticity. The residual plot showed unequal variance among the residuals and the normal probability plot was non-linear (Figure 4.2). As previously mentioned, logarithmic base-10 data transformation has proven to be effective in normalizing residuals of turbidity-SSC regressions (Rasmussen et al., 2009). A logarithmic base-10 transformation of both the response and explanatory variables was done. This transformation is equivalent to a power function regression performed on untransformed variables and used for many streamflow-SSC transport curves (Glysson, 1987; Curtis et al., 2006; Rasmussen et al., 2009). Linear regression using the log-transformed values resulted in a P-value of 6.6×10^{-70} for turbidity as a predictor of SSC, which is less than the alpha-level of 0.05, suggesting it is a statistically significant predictor. Likewise, log-transformations greatly improved the residual plot and normal probability plot (Figure 4.2) and the assumptions for linear regression analysis were met. The power regression model had a coefficient of determination (R^2-value) of 0.6451

indicating a moderately strong relationship between turbidity and suspended sediment concentration. Although this model was deemed sufficient, there was often large variability above and below the predicted values, particularly at low SSC values.

Results for the laboratory SSC-turbidity calibration curve for the automated grab samples showed a strong correlation between the lab turbidity measurements and the SSC concentrations with little variability around the curve (Figure 4.1). As hypothesized correlating the lab turbidity measurements and suspended sediment concentrations, showed less variability and had a higher R^2-value of 0.9465 suggesting a strong relationship. When compared, the two models were similar with the in-situ model having a slightly higher scaling term and the lab model having a slightly higher exponent. The models correlated well during high turbidity, however not during low turbidites causing the difference in the scaling and exponent coefficients. Given the strength of the calibration for the laboratory calibration, this curve was used in sediment flux and yield calculations.

The findings from the laboratory sediment trap study support that SSC-Turbidity relationships for sediments at the upstream and downstream monitoring stations are not statistically different, highlighting that SSC-Turbidity curves developed at the downstream monitoring platform are applicable upstream (Figure 4.1). The regression models for laboratory sediment trap measurements between SSC and turbidity showed strong correlation between suspended sediment concentration and turbidity with scaling factors of 5.4 and 5.2, and exponents of 1.0 and 1.1 for upstream and downstream trap samples, respectively (Figure 4.1). The regression models were significant with an R^2-value of 0.96 and 0.94, respectively. Prior to analysis, the residual plots for both data sets were examined and determined to be normally distributed with equal variance (Figure 4.2) and

hence two-sample t-tests were used to compare distributions. Since the upstream and downstream artificial samples were made with the same range concentrations, we were able to compare the distributions of turbidity measurements for the upstream and downstream lab analyses. Results of the t-test comparing the two turbidity distributions had a P-value of 0.990 suggesting that there is no significant difference in the turbidity measurements between the upstream and downstream site. These results confirm that any differences in sediment compositions at the upstream and downstream sites did not significantly impact SSC-Turbidity relationships.

While between-site differences did not significantly impact SSC-turbidity calibration curves, we did find that sampling method (trap vs. pump samplers) impacted SSC-turbidity relationships, likely reflecting the particle-size bias induced by sediment trap samplers. The new measurements fell within the variability of the field measurements, however the upstream lab measurements tracked on the high side of the variability. This was displayed in the scaling term of the regression model which was two to four times larger than the scaling factor for the grab-sample calibrations. This difference prompted an investigation the particle size composition of the grab and trap samples. The grab samples had an average D_{50} of 38.65 microns while the trap samples had an average D_{50} of 11.39 microns. This suggested that the sediment trap samples may have had a size class bias resulting in models that over predict the suspended sediment concentrations, but the similarity between the two models gave confidence that the relationship between turbidity and suspended sediment concentration was very likely the same at both the upstream and downstream sites.

4.1.2 Particle Size Results

Results from the particle size analysis of suspended sediment sample show that there is high variability in suspended particle size at low turbidities, but as turbidity increases the suspended sediment become more homogenized, decreasing the particle size variability (Figure 4.3). A power function was found to describe the relationship between particle size and turbidity. Although there was still some variability in the D90 particle size at high turbidities, turbidity explained 75% of the variability in the D10 particle size. The power relationship between turbidity and D50 particle size was also very strong with an R^2 value of 0.71 (Figure 4.3). This function was used to predict particle size as a function of instantaneous turbidity in the sediment flux model to account for the variability in settling velocity when constructing concentration profiles.

4.1.3 Sediment Yield Results

Comparison of sediment yield results using the continuous monitoring and sediment rating curve approaches showed contrasting loadings on an annual basis. The continuous sediment yield results showed that 3,592,308 kg or 3,592.3 tons of suspended sediment was transported from the watershed during the entire monitoring period. When normalizing the results per watershed area and days measured, the suspended sediment yields were estimated to be 153.5 t/yr/mi^2. Separate sediment rating curves were constructed for the rising and falling limbs at upstream site and used to predict sediment fluxes as a function of discharge (Figure 4.4). A power regression was fit to the rising and falling limb datasets and both had a strong R^2-value of 0.7941 and 0.8453 respectively. The sediment rating curve estimated a suspended sediment yield of 801.9 tons or 34.3

t/yr/mi^2 for the same monitoring period. The annual suspended sediment yield predicted from the sediment rating curve was only 22.3% of the yield predicted by the continuous data. The sediment rating curve over and underpredicted instantaneous fluxes predicted by the high-resolution model. The over-predication periods occurred at lower base fluxes and the under-prediction periods occurred during higher event fluxes (Figure 4.5).

The individual event yields were highly variable using the continuous estimation approach. Event 1 was found to have the highest suspended sediment flux of 43,516 kg/hr and Event 17 was found to have the lowest average flux of 88kg/hr. The variability in sediment yields was heavily associated with flow variability. In events that had a maximum flowrate greater than 1,000 ft^3/s, the maximum event yield was found to be 587,460 kg with an average yield of 424,100 kg. In events that had a maximum flowrate less than 100 ft^3/s, the maximum event yield was found to be 21,728 kg with an average yield of 12,433 kg. Seasonality does appear to have an effect on event yields as well. The winter months had the highest seasonal average event yield at 224,433 kg, followed by the summer months with an average event yield of 164,568 kg. The spring and fall months had much lower seasonal averages with average event yields of 88,046 kg and 89,705 kg respectively.

Individual event suspended sediment yields were also calculated using the sediment rating curve method and often contrasted the continuous estimation method, despite similar long-term averages. The sediment rating curve estimated every event yield significantly lower, estimating anywhere from 5.5% to 41% of the modeled event yields (Table 4.2, Figure 4.5). On average the sediment rating curve predicted 16.8% of the modeled yields across all the events. Both methods found Event 1 to have the highest yield and Event 17

to have the lowest. However, unlike the data driven model predictions, the sediment rating curve predicted almost similar sediment fluxes for Event 1 and Event 3. In general, the sediment rating curve method does a better job of predicting yields in the fall and winter and a worse job in the summer when compared to the continuous estimates of suspended sediment yields.

4.2 Source and Flow Pathway Dynamics

Hysteresis analysis results displayed a variety of hysteresis loop types and magnitudes (Figure 4.6). The most frequent loop shape was the figure 8 shape that occurred during 9 of the events followed by 5 counterclockwise loops, 3 single lines, 1 single line with a clockwise loop, and 1 clockwise loop. The figure-8 shape occurred during four out of the six summer events, but was also seen periodically in the winter, spring, and fall months. Winter was also heavily comprised of figure-8 events, accounting for three out of the six events that season. In the spring, the counterclockwise loop was the most prevalent, as it was present for half of the events. The fall experienced three different hysteresis shapes, a figure 8, a single line, and a counterclockwise loop. During all three events in the summer of 2019, there was a large peak in concentration on the falling limb of the discharge.

Hysteresis index was observed to vary seasonally and as a function of antecedent rainfall. A timeseries of the average event hysteresis (Figure 4.7) indices shows that the hysteresis loops in the winter display weak to moderate positive patterns and loops in the summer display stronger negative patterns. The influence of antecedent rainfall on hysteresis index was examined (Figure 4.7) since soil moisture conditions can influence

the volume and timing of runoff as well as the soil erodibility. While the amount of precipitation 48 hours prior to the event was only found to explain 26% of the variability, the precipitation 96 hours prior to the event was found to explain 52% of the variability in the hysteresis index.

Unmixing analysis results suggest high variability in source contributions between baseload stream network sources, and wash load sources in the basin (Table 4.3, Figure 4.8). The base load sources (YS1) were responsible for 12% to 100% of the total suspended sediment yield in the events. The activation of the base load sources is related to the hysteresis shape. Single line shapes indicate that 100% of the suspended sediment yield is from base load sources. All three single line hysteresis patterns were found in late fall and early winter. Clockwise loops indicate a flushing of the proximal sources. One clockwise hysteresis loop occurred in late winter and the base load source was responsible for 80% of the total sediment yield for that event. Counterclockwise loops indicate prominence of distal sources. Counterclockwise loops were the second most present hysteresis loop pattern occurring in every season and during 5 out of the 19 events. The contribution of the base load source during counterclockwise patterns was highly variable ranging from 13%-64%. The proportion of the base load and wash load sediment sources for the figure-8 shapes is highly variable as well. The base load sources can contribute 21% to 87% of the total suspended sediment yield for the event. During the summer 2018, the base load sources are a significantly larger portion of the total yield than in summer 2019 creating a strong negative discharge percentile HI value (Table 4.4).

Results of the unmixing analysis show a source activated on the rising and falling limb for the wash load (YS2) source in most events. To investigate this further, the wash

load was decomposed in to two sources (Table 4.5). The first source (YS2-a), was found to contribute from 13%-88% and source 2 (YS2-b) from 12-87% of the wash load. During the line and loop hysteresis pattern in Event 3, YS2-a constituted 88% of the wash load. During figure-8 events, on average, YS2-a contributed 40% of the wash load and YS2-b contributed 60%. YS2-b dominated during counterclockwise hysteresis. Antecedent moisture appeared to play an important role in the source contributions. YS2-a was found to be the highest at 88% of the wash load component when there was the highest precipitation 48 and 96 hours prior to the start of the event. Linear regression between 96-hour antecedent precipitation suggest antecedent moisture explains 51% of the variability in the source contributions, with YS2-b contributions having a higher proportion of wash load during low antecedent moisture conditions.

4.3 Measurements of Sediment Retention in Confluence Floodplains

The continuous sediment yield results for 2019 found that about 40% of the inputs into the confluence floodplain were retained. The data showed that Fourpole Creek transported 3,592.3 tons of suspended sediment into the confluence control volume and the Ohio River transported 1,732.1 tons of suspended sediment into the confluence control volume over the course of the year. At the outlet, 3,156.6 tons of suspended sediment was exported to the Ohio River from Fourpole Creek, resulting in a system retention of 2,167.8 tons of sediment within the 0.78km^2 confluence floodplain. If all the sediment retained in the system was deposited and distributed equally throughout the entire floodplain, there would be about 0.17cm or 1.7mm increase in the floodplain sediment depth.

Results suggest that the confluence floodplain is both a source and a sink for sediments throughout the year. Figure 4.9 shows a time series of the sediment stored in the floodplain, including both sediment deposits and temporary stored sediment suspended in the water column of the inundated floodplain. Each event on the hydrograph is associated with an increase in sediment storage and the magnitude of the increase is often proportional to the magnitude of the outlet stage for the event. In addition, the final recession of the outlet stage on the falling limb of the event hydrographs is often associated a loss of retained sediments, suggesting some of the sediment stored in the water column of the floodplain is transported out as the water recedes back to the stream channel. This emphasizes the control the Ohio River has on the transport and fate of the sediments within confluence floodplain system. The average outlet stage throughout the winter was 1.8m and during this period, 1,308.67 tons of sediment was retained. 66% of the annual net retention occurred during the first 3 months of the year.

Source-sink dynamics were highly variable for the nineteen monitored events (Table 4.6). For sixteen events, the confluence control volume was found to be a net sink of sediment, and three events showed that the control volume was a net source of sediment. The percentage of sediment retention during each event ranged from 21% to 96%, with the highest percent in the winter events. The three source events occurred in the spring and summer and the change in sediment flux upstream and downstream was, on average, about an order of magnitude lower than the amount of sediment retained for most of the sink events. Event 1 had the highest inputs at 596,823 kg being transported into the system. However, Event 9 was the largest sink with 340,143 kg of sediment retained. Despite Event 1 having 18% more sediment inputs, 35% more sediment was retained in the

floodplain during Event 9. This is likely attributed to the magnitude of the backwater conditions. During Event 1, the maximum stage at the outlet was only 1.3m while the maximum stage during Event 9 was 5.4m. The extreme stage at the outlet likely caused an increase in the volume of water stored in the floodplain and the deceleration backwater conditions promoted deposition. This idea can be visualized when comparing the turbidity measurements at the upstream and downstream monitoring station for each event (Figure 4.10). During Event 1 the turbidity peaks at the upstream and downstream site are only about 45 minutes apart. The sediment was routed quickly through the system allowing only about a 15% decrease in peak turbidity between the monitoring stations. However, during Event 9 the extreme backwater conditions greatly increased the residence time and the turbidity peaks at the upstream and downstream site are about 10.5 hours apart. The slower flow conditions likely promoted more deposition and decreased the peak turbidity between the monitoring stations by 47%.

4.4 Confluence Sedimentation Model Results

The sediment transport was found to perform well during both calibration and validation periods. The NSE statistics for the calibration and validation runs were 0.601 and 0.759 respectively and the PBIAS statistics were -4.03 and 2.85 respectively. The sediment transport model simulated an annual flux of 3,038.85 ton of suspended sediment out of the system. This is within 4% of the measured annual flux out of the system. Similarly, the model simulated 2,055.94 tons of net sediment deposition in the floodplain which is within 2.5% of estimated floodplain deposition from the measured results. Figure 4.11 compares the measured, routed, and calibrated model results for the daily sediment fluxes out of the system. The measured results are the sediment fluxes measured at the downstream

monitoring site when the flow out of the system is positive. The routed results are the fluxes out of the system when no erosion or deposition is simulated. The modeled results are the fluxes out of the system when erosion and deposition is simulated after the relevant sediment transport parameters had been calibrated. The direct sediment routing provided poor model statistics with an NSE of -0.724 and a PBIAS of 53.464. It generally over predicts the fluxes during the winter and underpredicts in the summer when compared to the measured results. After simulating the erosion and deposition dynamics in the model, the calibrated results still have periods of over and under prediction but compare substantially better to the measured results.

The depositional and erosional dynamics varied heavily from reach to reach (Figure 4.12). Reach 1 (the most upstream reach) had the least amount of deposition and the highest amount of erosion in the floodplain. The floodplain was found to be net erosive in this reach, losing about 1,179 kg of sediment and slightly degrading by 0.004mm. Reach 1 was the only reach to have bank erosion with 271,868 kg eroded over the year. 43% of this erosion occurred in the summer months and the rest occurred during isolated events throughout the remainder of the year. Reach 2 had the second highest amount of deposition in the floodplain with 731,893 kg of freshly deposited sediment, 28% of which was later eroded. Reach 2 had a net deposition of 530,746 kg of sediment and when normalized for the surface area of the reach, caused the floodplain in this reach to aggrade 2.8mm over the year. Reach 3 had the highest amount of deposition and erosion in the floodplain, 1,219,333 kg and 566,118 kg of sediment respectively. Reach 3 had a net deposition of 653,215 kg but being the largest reach, the floodplain only aggraded 2.3mm over the year. Reach 4 was the only reach to have no floodplain erosion. The deposition is this reach was 549,572

kg which caused the floodplain to aggrade by 2.9mm, the highest aggradation of any reach. Reach 5 had 684,244 kg of sediment deposited and 88,791 kg of erosion. Reach 5 had a net deposition of 595,453 kg which caused a 2.6mm aggradation of the floodplain.

The modeled reach dynamics were studied on an event scale for 4 hysteresis patterns. There is currently no method to examine hysteresis loops in systems that experience backwater conditions, so the influence of upstream hysteresis patterns on erosional and depositional processes in the floodplain was explored. Events 5 and 6 both displayed a single line hysteresis pattern at the upstream monitoring site. During this relationship the suspended sediment concentration and flowrate increase at the same rate and all the suspended sediment supplied is a result of the erosive power of the flow. Over the course of these two events (Figure 4.13), erosion occurred in Reaches 1, 2, and 3. In Reach 2 and 3 floodplain erosion occurred during both events, but in Reach 1 erosion only occurred during Event 6. Floodplain erosion typically occurs when the residual transport capacity is high. The transport capacity during Event 5 in Reach 1 was too low to cause erosion, but changes in fluid shear stress in Reaches 2 and 3 likely increased the transport capacity allowing erosion to occur. The residual transport capacities in Reaches 4 and 5 are low and deposition occurs. During Event 6, the highest floodplain accumulation occurs in Reach 2 and is likely mostly deposits of sediment eroded from the floodplain in Reach 1. The influence of the upstream single line hysteresis pattern appears to resonate through Reaches 1-3, but the backwater becomes the dominant control in Reaches 4 and 5 creating low fluid shear stresses and subsequent low transport capacities.

Counterclockwise hysteresis patterns were found to deposit more sediment in upstream reaches (Figure 4.14). In a counterclockwise loop, the peak suspended sediment

concentration occurs after the peak flowrate, suggesting that sediment is predominately from distal sources. During Event 8, more sediment was deposited in Reaches 1 and 2 than in the downstream reaches of the control volume. The residual transport capacity for all the reaches was generally low, however transport capacity spiked in reaches 2, 3, and 5 during peak flow. Minute amounts of floodplain erosion occurred during these spikes. The least amount of deposition occurred in Reach 4.

Clockwise hysteresis patterns were found to deposit more sediment in downstream reaches (Figure 4.15). In a clockwise loop, the peak suspended sediment concentration occurs before the peak flowrate, suggesting that sediment is predominately from nearby unconsolidated material in the fluvial network. Event 10 displayed a clockwise hysteresis pattern upstream of the floodplain. In this event, more sediment is deposited in the downstream reaches with little deposited in the upstream reaches. Reaches 2 and 3 again experienced spikes in residual transport capacity. Reach 3 experienced the greatest amount of deposits but Reach 4 and Reach 5 still experienced appreciable amounts of deposition. This suggests sediment deposited in Reaches 1 and 2 is sediment from upland sources, while the majority of sediment deposited in Reaches 3-5 is sediment from in channel and other nearby sources.

Figure 8 was the most common hysteresis pattern experienced at the upstream site and showed a mixture of clockwise and counterclockwise dominance for sediment fluxes, which further support the erosion/deposition findings from the aforementioned results. Counterclockwise figure 8 patterns mimic the same depositional floodplain patterns as the counterclockwise loops (Figure 4.16 and 4.17). Events 7 and 9, both counterclockwise figure 8, experienced the most deposition in Reach 1 and Reach 2. Clockwise figure 8

patterns were also found to mimic the depositional floodplain patterns of clockwise loops (Figure 4.18). During Event 11, Reach 1 and 2 experienced little deposition and Reach 2 even experienced large amounts of erosion with spikes in residual transport capacity. The most deposition occurred in Reaches 3 and 4, but even Reach 5 experienced more deposition than Reach 1 and Reach 2. In summary, upstream hysteresis patterns strongly influence deposition/erosion dynamics of floodplain sediments in backwater confluence features.

4.5 Particulate Nitrogen Yield Estimates

Results show that POM content had high variability at low turbidities that decreased with increasing turbidity (Figure 4.19). Four regions were established and the average percent POM in the lowest turbidity region was found to be 26.25% with a standard deviation of 17%. The average percent POM decreased with increasing in turbidity until the highest turbidity region where it was found to homogenize around 9.55%. These averages were incorporated into the PN yield equation (3.19) to account for the POM content variability in particulate N estimates.

Results show that PN inputs to the Fourpole Creek wetland are high and variability in composition plays an important role in loading for moderate events. For the entire monitoring period, the POM yield was found to be 619,520 kg or 10,223 kg/km^2. The particulate nitrogen yield for the entire monitoring period were estimated to be between 17,700 kgN and 36,665 kgN. This equates to an average of 13,861-28,713 kgN annually. Variability in POM content sometimes resulted in differences in events that transported the most PN as compared to the most sediment. In general, PN yields were highest during

events when the sediment yields were the highest such as events 1,9, and 8. Additionally PN yields were lowest in events with the lowest sediment yields such as event 18, 16, and 17. However, for some events the sediment yields were higher respectively than the PN yields were. For example, event 11 has the 4th highest sediment yield but it has the 6th highest PN yield. Additionally, event 3 has the 5th highest PN yield but the 6th highest sediment yield. The winter had the highest average PN yields and the spring had the lowest PN yields.

PN inputs from the Ohio river were found to be highly variable during events, ranging from 0.2-166kg. Downstream PN loading estimates found that the Ohio River contributes 0-43% of the total event PN inputs. Variability in POM content also resulted in differences in events that retained the most PN as compared to the most sediment. Event 11 had the lowest percentage of sediment retained (from events that were sinks for sediment), however Event 1 had the lowest percentage of PN retained. Event 7, which had the highest sediment retention at 96%, also had the highest PN retention at 94%. In general, the percentage of sediment retained was reflective of the percentage of PN retained. Events that occurred in the winter had the highest PN retention and three spring and summer events found the system to be a source of PN discharging as much as 203kg of PN during the event.

For the 2019 calendar year, 19,745-35,260kgN was imported into the confluence floodplain wetland. Foupole Creek contributed 11,400-20,358kgN while the Ohio River contributed 8,345-14,902kgN, 58% and 42% of the total inputs respectively. The system exported 16,739-29,890 kgN to the Ohio River, retaining 3,006-5,370kgN or 18% of the PN inputs the wetland. This is equivalent to 49.6-88.6kgN/km^2 annually.

4.6 Tables and Figures

Table 4.1. Multiple and simple linear regression results for turbidity and suspended sediment concentration. Flowrate is included as an explanatory variable given backflows (negative Q) were anticipated to impact calibration curves given the potential influence.

Multiple Linear Regression: Explanatory Variables Turbidity and Flowrate						
	Coefficients	*Standard Error*	*t Stat*	*P-value*	*Lower 95%*	*Upper 95%*
Intercept	19.491	5.736	3.398	0.0008	8.202	30.779
Turbidity	1.137	0.044	25.93	1.08E-78	1.05	1.223
Flowrate	0.071	0.053	1.329	0.185	-0.034	0.176
Multiple Linear Regression: Explanatory Variables log(Turbidity) and Flowrate						
	Coefficients	*Standard Error*	*t Stat*	*P-value*	*Lower 95%*	*Upper 95%*
Intercept	0.43	0.05	8.667	2.79E-16	0.333	0.528
log (Turbidity)	0.837	0.036	23.21	4.96E-69	0.766	0.908
Flowrate	-2.69E-04	2.04E-04	-1.32	0.188	-6.70E-04	1.32E-04
Simple Linear Regression: Explanatory Variables Turbidity						
	Coefficients	*Standard Error*	*t Stat*	*P-value*	*Lower 95%*	*Upper 95%*
Intercept	21.376	5.565	3.841	1.49E-04	10.425	32.328
Turbidity	1.14	0.044	26.04	3.55E-79	1.054	1.227
Simple Linear Regression: Explanatory Variables log(Turbidity)						
	Coefficients	*Standard Error*	*t Stat*	*P-value*	*Lower 95%*	*Upper 95%*
Intercept	0.435	0.05	8.784	1.20E-16	0.338	0.533
log (Turbidity)	0.827	0.035	23.43	6.60E-70	0.757	0.896

Table 4.2. Sediment yield estimates using the continuous sediment load estimation method and the sediment rating curve method.

Event	Date	Duration (hr)	Maximum Flowrate (ft^3/s)	Measured Sediment Yield (kg)	SRC Sediment Yield (kg)	SRC % of Modeled Suspended Sediment Yield
1	9/9/2018	13.5	1,092	589,020	63,215	10.76%
2	9/23/2018	16	168	63,849	4,718	7.35%
3	9/27/2018	15.75	1,184	209,620	58,923	28.10%
4	11/15/2018	68.25	764	216,000	61,165	28.19%
5	1/19/2019	26	610	126,490	34,936	27.46%
6	1/23/2019	23.75	765	179,580	46,722	25.95%
7	2/12/2019	14	390	137,110	13,841	10.07%
8	2/20/2019	10	909	363,100	41,133	11.35%
9	2/23/2019	19.25	1,292	475,800	56,607	11.91%
10	3/9/2019	19.75	226	63,778	10,597	16.44%
11	5/3/2019	27	466	229,110	22,043	9.60%
12	5/12/2019	35.75	198	21,223	9,106	40.95%
13	5/17/2019	11.75	69	21,342	1,400	6.44%
14	6/16/2019	15	258	78,270	9,477	12.04%
15	7/22/2019	16.75	391	110,080	11,561	10.47%
16	8/23/2019	39.5	43	11,920	787	6.50%
17	8/27/2019	39.5	9	3,477	192	5.52%
18	10/6/2019	18.75	173	13,079	3,251	24.11%
19	12/29/2019	30.75	174	35,697	10,077	26.09%

Table 4.3. Unmixing analysis for base load (YS1) and wash load (YS2) contributions during individual storm events.

Event	Date	Season	Hysteresis Shape	YS (kg)	YS1 (kg)	YS2 (kg)	YS1/YS
1	9/9/2018	Summer 2018	Figure 8	575,154	274,789	300,365	48%
2	9/23/2018	Summer 2018	Figure 8	63,250	50,152	13,097	79%
3	9/27/2018	Summer 2018	Line with Clockwise Loop	207,004	187,159	19,846	90%
4	11/15/2018	Fall 2018	Counterclockwise	214,202	72,554	141,648	34%
5	1/19/2019	Winter 2019	Single Line	125,795	125,795	0	100%
6	1/23/2019	Winter 2019	Single Line	177,746	177,746	0	100%
7	2/12/2019	Winter 2019	Figure 8	133,343	74,570	58,773	56%
8	2/20/2019	Winter 2019	Counterclockwise	353,785	183,676	170,109	52%
9	2/23/2019	Winter 2019	Figure 8	461,244	309,335	151,909	67%
10	3/9/2019	Winter 2019	Clockwise	63,736	50,586	13,150	79%
11	5/3/2019	Spring 2019	Figure 8	226,530	196,979	29,551	87%
12	5/12/2019	Spring 2019	Figure 8	22,278	14,556	7,662	66%
13	5/17/2019	Spring 2019	Counterclockwise	21,541	6,725	14,816	31%
14	6/16/2019	Spring 2019	Counterclockwise	77,717	48,856	28,861	63%
15	7/22/2019	Summer 2019	Figure 8	109,376	22,575	86,801	21%
16	8/23/2019	Summer 2019	Figure 8	12,025	3,352	8,673	28%
17	8/27/2019	Summer 2019	Counterclockwise	3,425	415	3,009	12%
18	10/6/2019	Fall 2019	Figure 8	13,416	4,669	8,747	35%
19	12/29/2019	Fall 2019	Single Line	36,537	36,537	0	100%

Table 4.4. Hysteresis index changes as a function of discharge and the average hysteresis index for each event.

	HI for Discharge Percentile																			
Event	5%	10%	15%	20%	25%	30%	35%	40%	45%	50%	55%	60%	65%	70%	75%	80%	85%	90%	95%	**Average HI**
1	-0.05	-0.05	-0.05	-0.06	-0.07	-0.07	-0.07	-0.08	-0.08	-0.09	-0.10	-0.13	-0.15	-0.18	-0.18	-0.23	-0.23	-0.57	0.25	**-0.12**
2	-0.06	-0.07	-0.07	-0.08	-0.08	-0.09	-0.10	-0.11	-0.11	-0.14	-0.15	-0.11	-0.07	0.11	0.29	0.38	0.30	0.35	0.37	**0.03**
3	-0.21	-0.23	-0.22	-0.25	-0.22	-0.20	-0.21	-0.21	-0.16	-0.08	0.01	0.03	0.02	0.07	0.03	0.09	0.29	0.21	0.15	**-0.06**
4	-0.10	-0.13	-0.14	-0.13	-0.14	-0.17	-0.18	-0.24	-0.28	-0.42	-0.39	-0.39	-0.44	-0.51	-0.57	-0.69	-0.68	-0.79	-0.71	**-0.37**
5	-0.03	-0.05	-0.04	-0.04	-0.01	-0.01	0.02	0.04	0.02	0.11	0.10	0.26	0.29	0.37	0.36	0.17	0.05	-0.04	-0.12	**0.08**
6	-0.16	-0.15	-0.12	-0.10	-0.16	-0.09	-0.04	0.03	0.10	0.15	0.18	0.23	0.28	0.30	0.30	0.19	0.33	0.48	0.28	**0.11**
7	-0.02	-0.04	-0.05	-0.04	-0.06	-0.08	-0.07	-0.08	-0.06	-0.04	-0.02	0.03	0.14	0.25	0.54	0.69	0.40	0.10	-0.08	**0.08**
8	N/A	-0.01	-0.04	-0.06	-0.07	-0.08	-0.08	-0.06	-0.04	-0.03	-0.03	-0.03	-0.02	0.01	0.12	0.18	0.21	0.16	-0.04	**0.01**
9	0.04	0.08	0.10	0.16	0.17	0.27	0.30	0.35	0.38	0.42	0.55	0.72	0.76	0.77	0.71	0.63	0.51	0.32	0.21	**0.39**
10	-0.08	-0.08	-0.06	-0.03	-0.04	-0.05	-0.09	-0.10	-0.08	-0.04	0.01	0.14	0.13	0.20	0.12	0.09	0.04	-0.10	-0.23	**-0.01**
11	N/A	0.14	0.18	0.21	0.40	0.61	0.36	0.39	0.36	0.23	0.04	-0.02	-0.18	-0.32	-0.24	-0.34	-0.47	-0.42	-0.21	**0.04**
12	-0.15	-0.23	-0.37	-0.42	-0.49	-0.44	-0.60	-0.63	-0.67	-0.60	-0.57	-0.27	0.17	0.35	0.31	0.31	0.17	0.14	0.12	**-0.20**
13	N/A	-0.38	-0.36	-0.37	-0.48	-0.55	-0.66	-0.78	-0.41	-0.07	0.19	0.26	0.23	0.13	0.13	0.10	-0.01	-0.11	0.11	**-0.17**
14	0.09	-0.04	0.02	-0.03	-0.02	-0.15	-0.22	-0.31	-0.39	-0.36	-0.48	-0.50	-0.45	-0.38	-0.55	-0.51	-0.57	0.05	0.03	**-0.25**
15	-0.43	-0.61	-0.89	-0.99	-0.94	-0.85	-0.69	-0.58	-0.56	-0.26	-0.22	-0.22	-0.18	-0.21	-0.18	-0.11	0.07	0.28	0.20	**-0.39**
16	-0.05	-0.16	-0.30	-0.43	-0.50	-0.77	-0.96	-0.95	-0.65	-0.60	-0.46	-0.33	-0.18	-0.19	-0.09	0.08	0.11	0.16	0.19	**-0.32**
17	N/A	-0.02	-0.04	-0.05	-0.08	-0.11	-0.15	-0.18	-0.29	-0.32	-0.43	-0.59	-0.68	-0.91	-0.48	-0.21	0.15	0.19	0.35	**-0.21**
18	-0.13	-0.06	-0.04	-0.07	-0.13	-0.12	-0.10	-0.11	-0.11	-0.10	-0.10	-0.14	-0.20	-0.27	-0.29	-0.28	-0.27	-0.20	0.18	**-0.13**
19	0.18	0.26	0.18	0.30	0.19	0.24	0.36	0.29	0.21	0.30	0.37	0.43	0.36	0.36	0.45	0.43	0.31	0.46	0.42	**0.32**

Table 4.5. The decomposition of the two major wash load sources, into YS2-a and YS2-b, activated during many events.

Event	Date	Season	Hysteresis Shape	YS2-a	YS2-b	%YS2-a	%YS2-b	Event Precipitation	48 hr. Precipitation	96 hr. Precipitation
1	9/9/2018	Summer 2018	Figure 8	122,480	177,885	41%	59%	4.32	0.1	0.1
3	9/27/2018	Summer 2018	Line with Clockwise Loop	17,445	2,401	88%	12%	0.88	0.41	2.76
7	2/12/2019	Winter 2019	Figure 8	21,483	37,208	37%	63%	1.77	0	0.85
8	2/20/2019	Winter 2019	Counterclockwise	33,022.99	137,085.87	19%	81%	1.42	0	0.09
10	3/9/2019	Winter 2019	Clockwise	7,384	5,767	56%	44%	0.84	0.32	0.33
12	5/12/2019	Spring 2019	Figure 8	1,015	6,647	13%	87%	0.94	0.17	0.17
13	5/17/2019	Spring 2019	Counterclockwise	5,685	9,132	38%	62%	0.82	0	0.01
14	6/16/2019	Spring 2019	Counterclockwise	5,744	23,121	20%	80%	1.05	0	0.22
15	7/22/2019	Summer 2019	Figure 8	38,698	48,220	45%	55%	1.60	0	0.64
16	8/23/2019	Summer 2019	Figure 8	1,834	6,840	21%	79%	1.82	0	0
17	8/27/2019	Summer 2019	Counterclockwise	1,017	1,993	34%	66%	0.70	0	1.82

Table 4.6. The sediment fluxes into and out of the floodplain as well as the sediment yield retained in the floodplain.

Event	Date	Season	Hysteresis Shape	Upstream Inputs (kg)	Downstream Inputs (kg)	Downstream Outputs (kg)	Net Retention (kg)	% of Inputs Retained
1	9/9/2018	Summer 2018	Figure 8	587,460	9,363	376,790	220,033	37%
2	9/23/2018	Summer 2018	Figure 8	64,228	13,119	22,256	55,091	71%
3	9/27/2018	Summer 2018	Line with Clockwise Loop	209,690	61	87,293	122,458	58%
4	11/15/2018	Fall 2018	Counterclockwise	217,010	9,929	123,760	103,179	45%
5	1/19/2019	Winter 2019	Single Line	127,240	18,897	76,951	69,186	47%
6	1/23/2019	Winter 2019	Single Line	180,070	12,852	83,271	109,651	57%
7	2/12/2019	Winter 2019	Figure 8	137,410	1,068	5,576	132,902	96%
8	2/20/2019	Winter 2019	Counterclockwise	362,250	0	80,281	281,969	78%
9	2/23/2019	Winter 2019	Figure 8	475,150	14,353	149,360	340,143	69%
10	3/9/2019	Winter 2019	Clockwise	64,479	31,092	13,064	82,507	86%
11	5/3/2019	Spring 2019	Figure 8	229,510	37	181,080	48,467	21%
12	5/12/2019	Spring 2019	Figure 8	22,236	4,529	7,620	19,145	72%
13	5/17/2019	Spring 2019	Counterclockwise	21,728	662	33,675	-11,285	-50%
14	6/16/2019	Spring 2019	Counterclockwise	78,711	8,321	58,551	28,481	33%
15	7/22/2019	Summer 2019	Figure 8	110,460	5,525	74,578	41,407	36%
16	8/23/2019	Summer 2019	Figure 8	12,103	13,157	32,845	-7,585	-30%
17	8/27/2019	Summer 2019	Counterclockwise	3,467	9,799	24,153	-10,887	-82%
18	10/6/2019	Fall 2019	Figure 8	13,484	8,617	13,263	8,838	40%
19	12/29/2019	Fall 2019	Single Line	38,621	19,193	8,453	49,361	85%

Table 4.7. The particulate nitrogen fluxes into and out of the floodplain as well as the particulate nitrogen retained in the floodplain.

Event	Duration (hr)	Date	Upstream PN Inputs (kg)	Downstream PN Inputs (kg)	Downstream PN Outputs (kg)	Net PN Retention (kg)	% of Inputs Retained
1	13.5	9/9/2018	1,668-2,979	39-69	1,432-2,558	275-492	16%
2	16	9/23/2018	183-326	41-74	79-142	145-258	65%
3	15.75	9/27/2018	690-1,232	0.3-0.5	305-545	385-687	56%
4	68.25	11/15/2018	701-1,253	57-103	341-610	417-746	55%
5	26	1/19/2019	428-764	59-105	236-421	251-448	52%
6	23.75	1/23/2019	594-1,061	56-104	268-479	364-686	56%
7	14	2/12/2019	396-707	5-9	24-43	377-673	94%
8	10	2/20/2019	1,025-1,831	-	240-429	785-1,402	77%
9	19.25	2/23/2019	1,375-2,456	46-82	486-867	935-1,662	66%
10	19.75	3/9/2019	206-369	89-160	50-90	245-439	83%
11	27	5/3/2019	657-1,174	0.2-0.3	516-922	141-252	21%
12	35.75	5/12/2019	82-147	33-59	19-34	96-172	83%
13	11.75	5/17/2019	61-127	3-5	106-190	-(42-58)	-65%
14	15	6/16/2019	235-419	27-48	196-349	66-118	25%
15	16.75	7/22/2019	316-564	25-45	226-404	115-205	34%
16	39.5	8/23/2019	35-63	47-84	113-203	-(31-56)	-38%
17	39.5	8/27/2019	11-19	39-69	98-176	-(48-88)	-96%
18	18.75	10/6/2019	45-80	22-39	39-69	28-50	42%
19	30.75	12/29/2019	122-219	93-166	42-75	173-310	80%

Figure 4.1. SSC-Turbidity power regression comparison for the field and laboratory turbidity measurements.

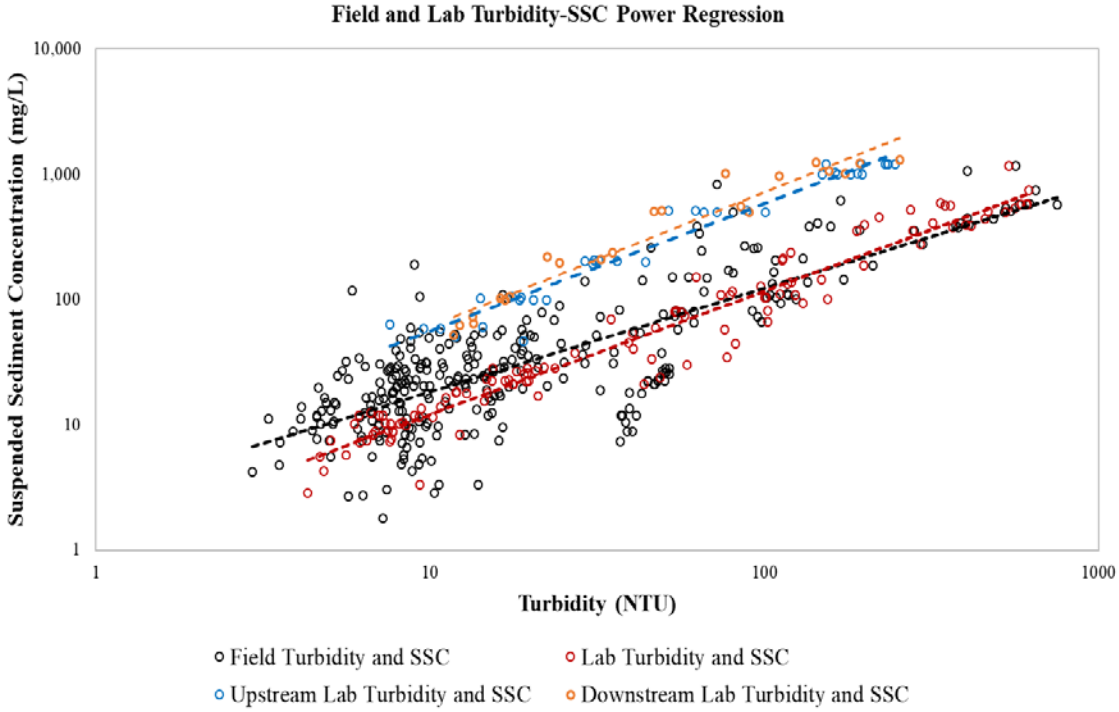

	Regression Power Function	Scaling Factor	Exponent	Coefficient of Determination
	$F(x)=ax^b$	**a**	**b**	**R^2**
Field Turbidity and SSC	$SSC=2.725(Turbidity)^{0.8268}$	2.725	0.8268	0.6451
Lab Turbidity and SSC	$SSC=1.2501(Turbidity)^{0.984}$	1.2501	0.984	0.9465
Upstream Lab Turbidity and SSC	$SSC=5.3959(Turbidity)^{1.0165}$	5.3959	1.0165	0.9548
Downstream Lab Turbidity and SSC	$SSC=5.1504(Turbidity)^{1.0719}$	5.1504	1.1109	0.9394

Figure 4.2. Statistical analysis for the SSC-Turbidity regression models. The top set of graphs compares the regression plot, residual plot, and normal probability plot of the SSC-Turbidity relationship of the data before and after the log transformation to determine normality. The bottom set of graphs are the residual plot and normal probability plot of the log transformed laboratory turbidity measurements for the upstream and downstream sites to determine normality.

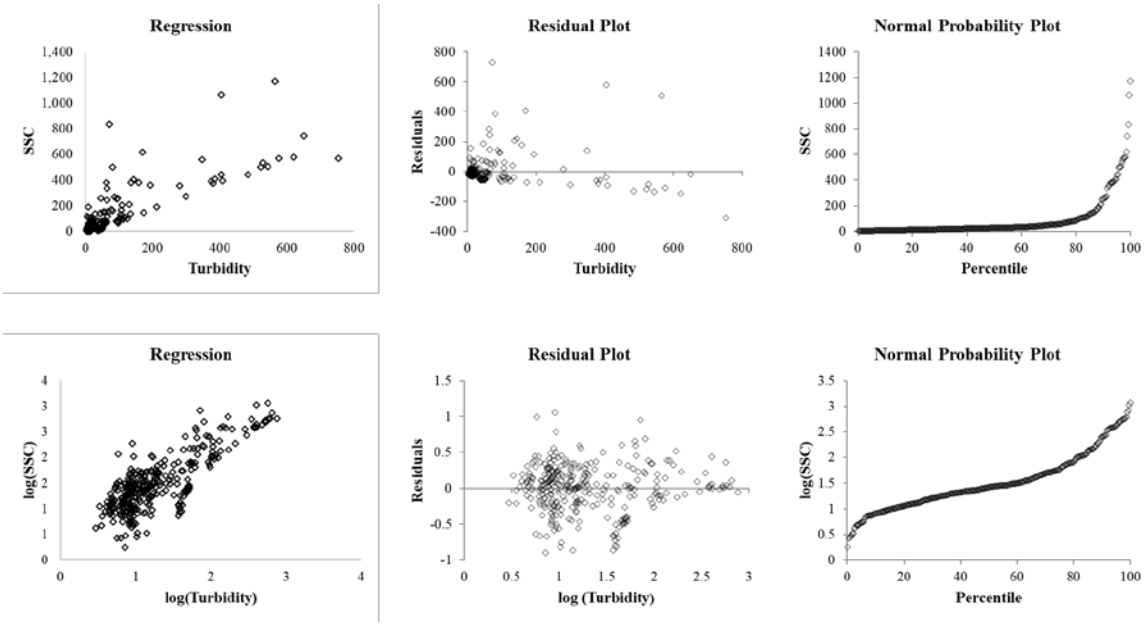

Upstream Samples ***Downstream Samples***

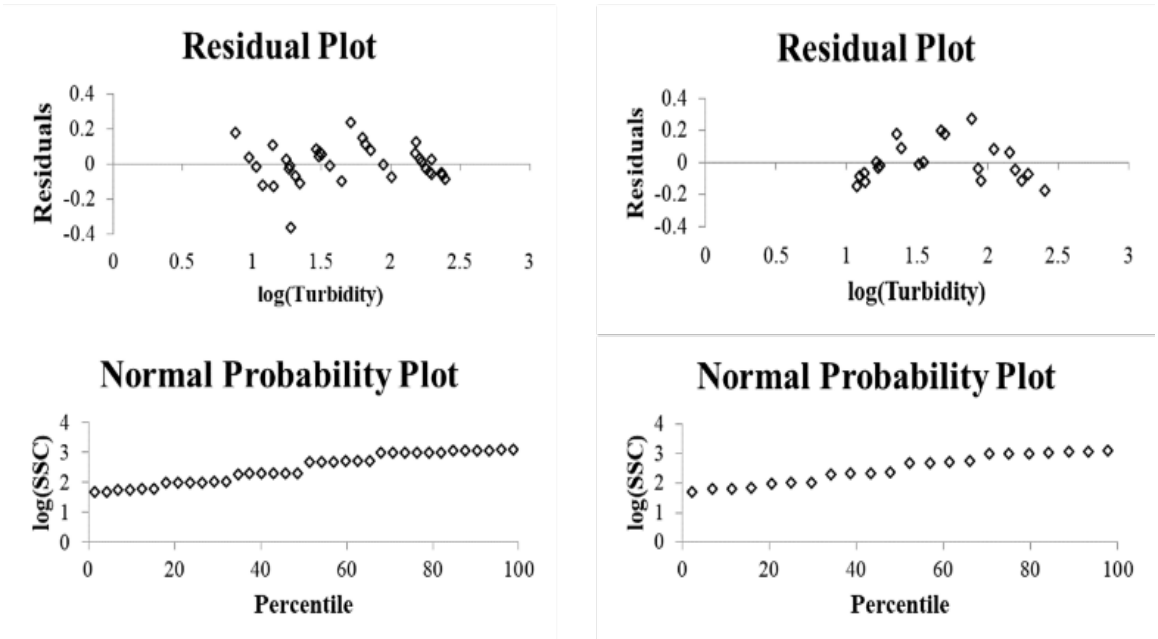

Figure 4.3. Particle size distribution analysis for suspended sediment samples as a function of turbidity collected at the Fourpole Creek floodwall station. Values for D10, D50 and D90 are provided. The D50 power function was used in the sediment flux model to vary settling velocity as a function of turbidity.

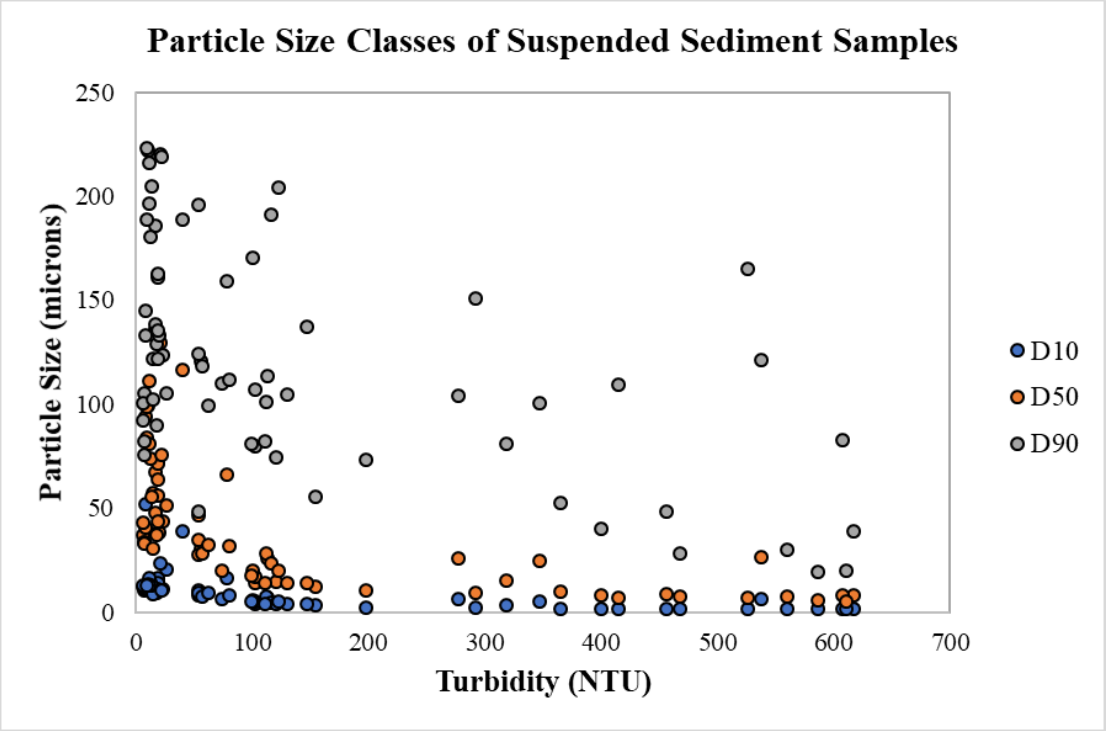

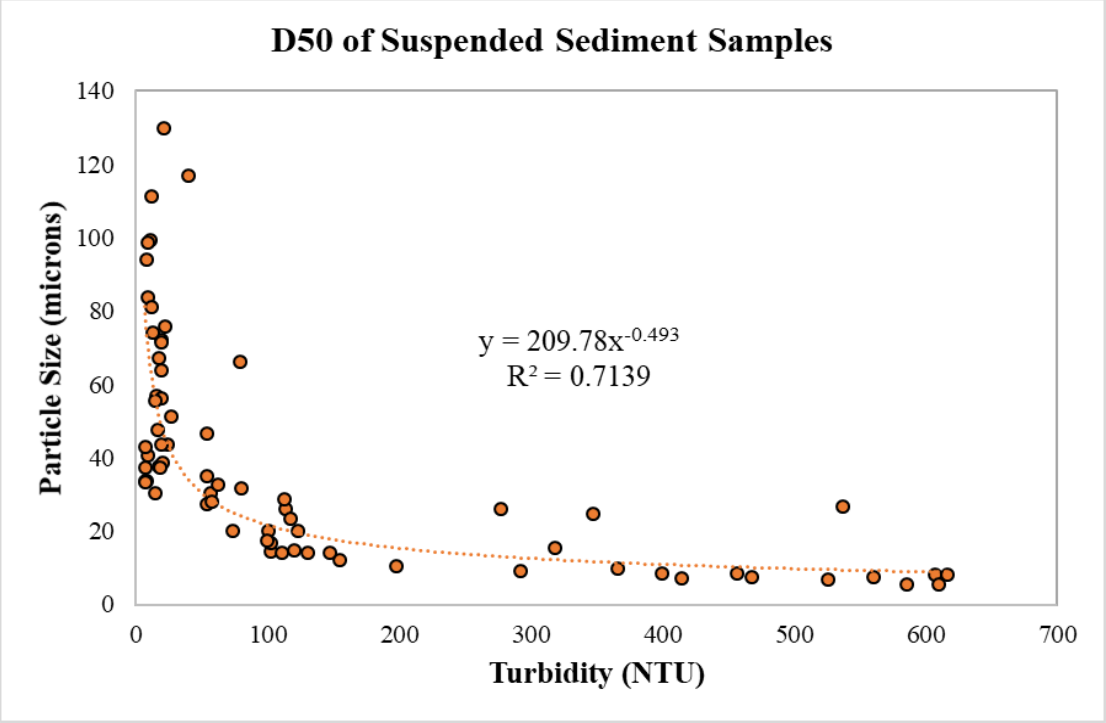

Figure 4.4. Due to the hysteretic nature of sediment transport, two sediment rating curves were used to relate suspended sediment flux (Qss) to discharge (Q). A power relationship is fit between suspended-sediment flux as a function of discharge which commonly follows a power relationship.

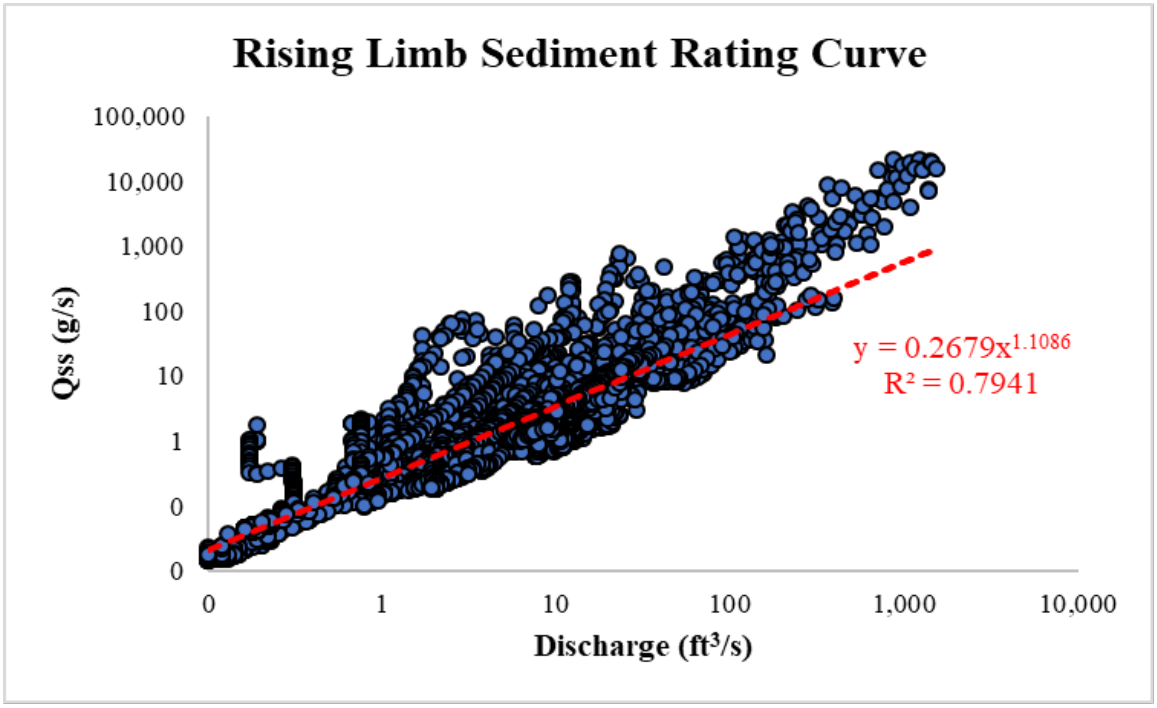

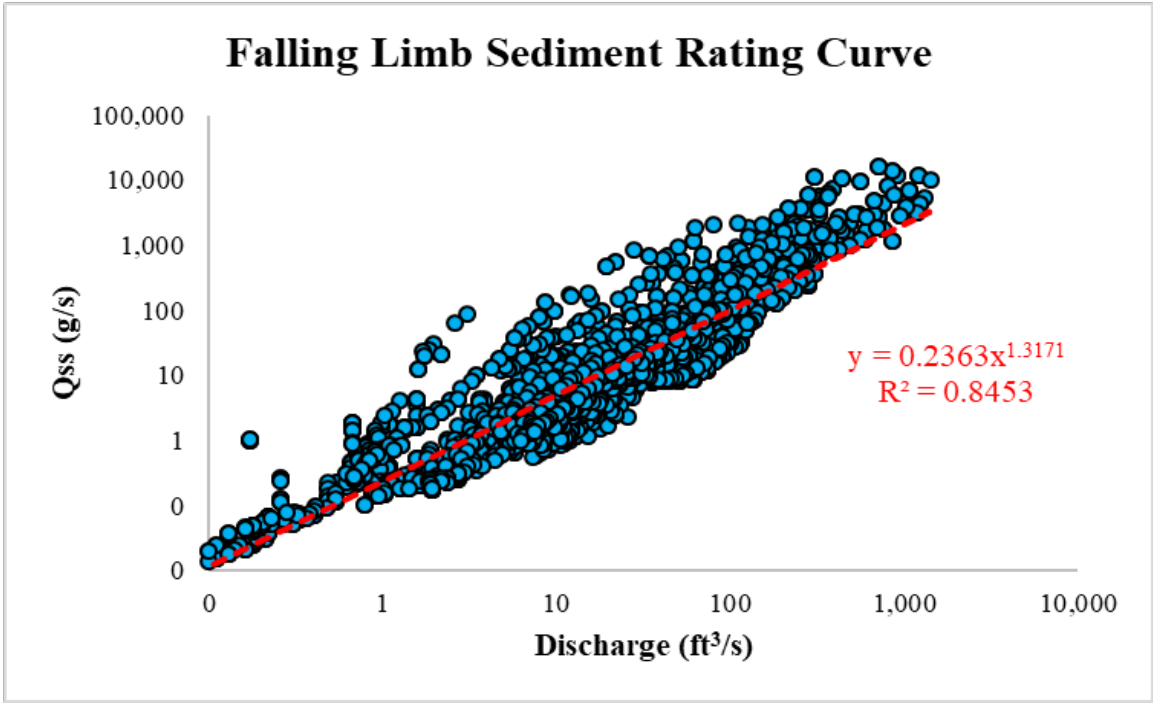

Figure 4.5. Time series and event comparison of sediment flux predictions from the high-resolution model to the sediment rating curve.

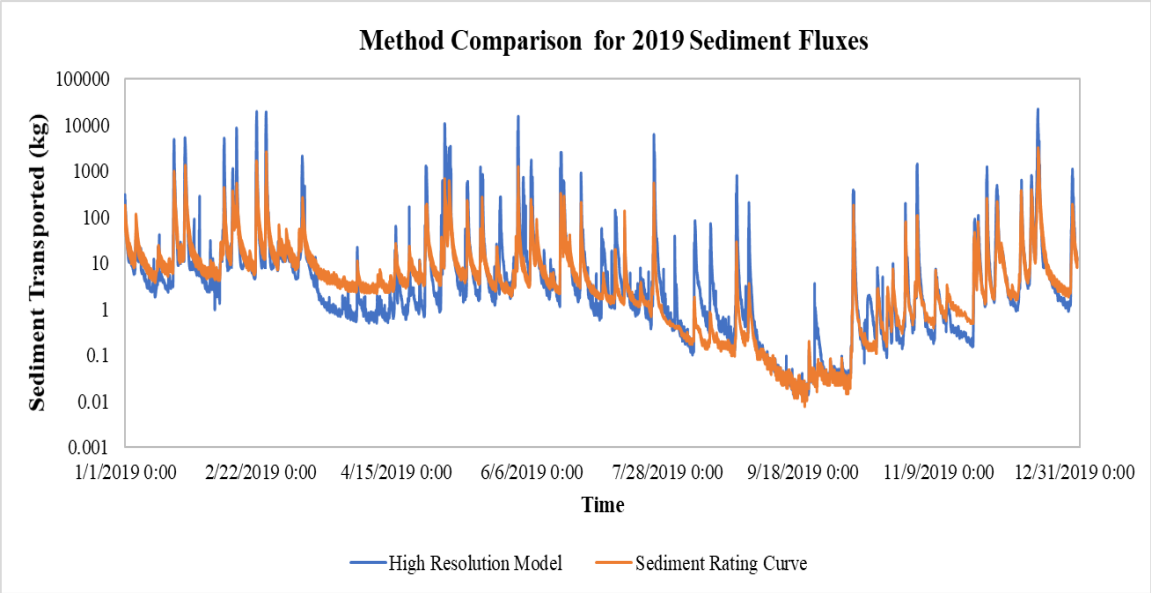

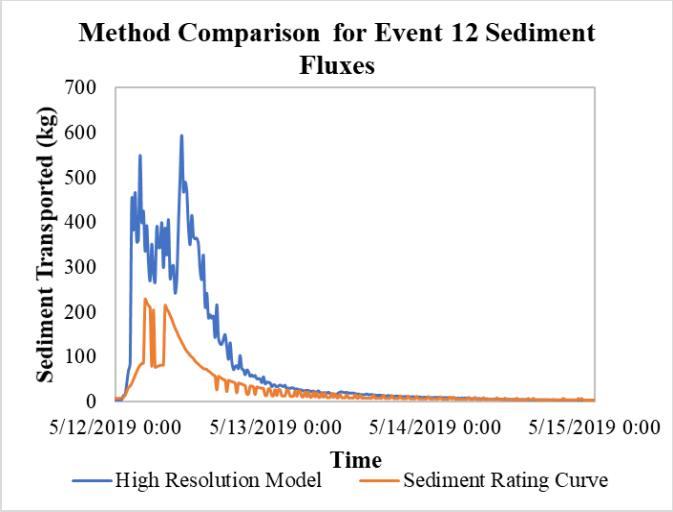

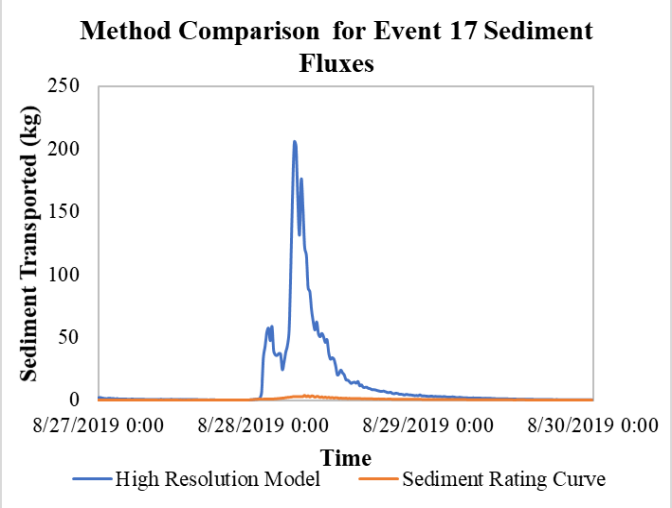

Figure 4.6. The hysteresis loop patterns for each event.

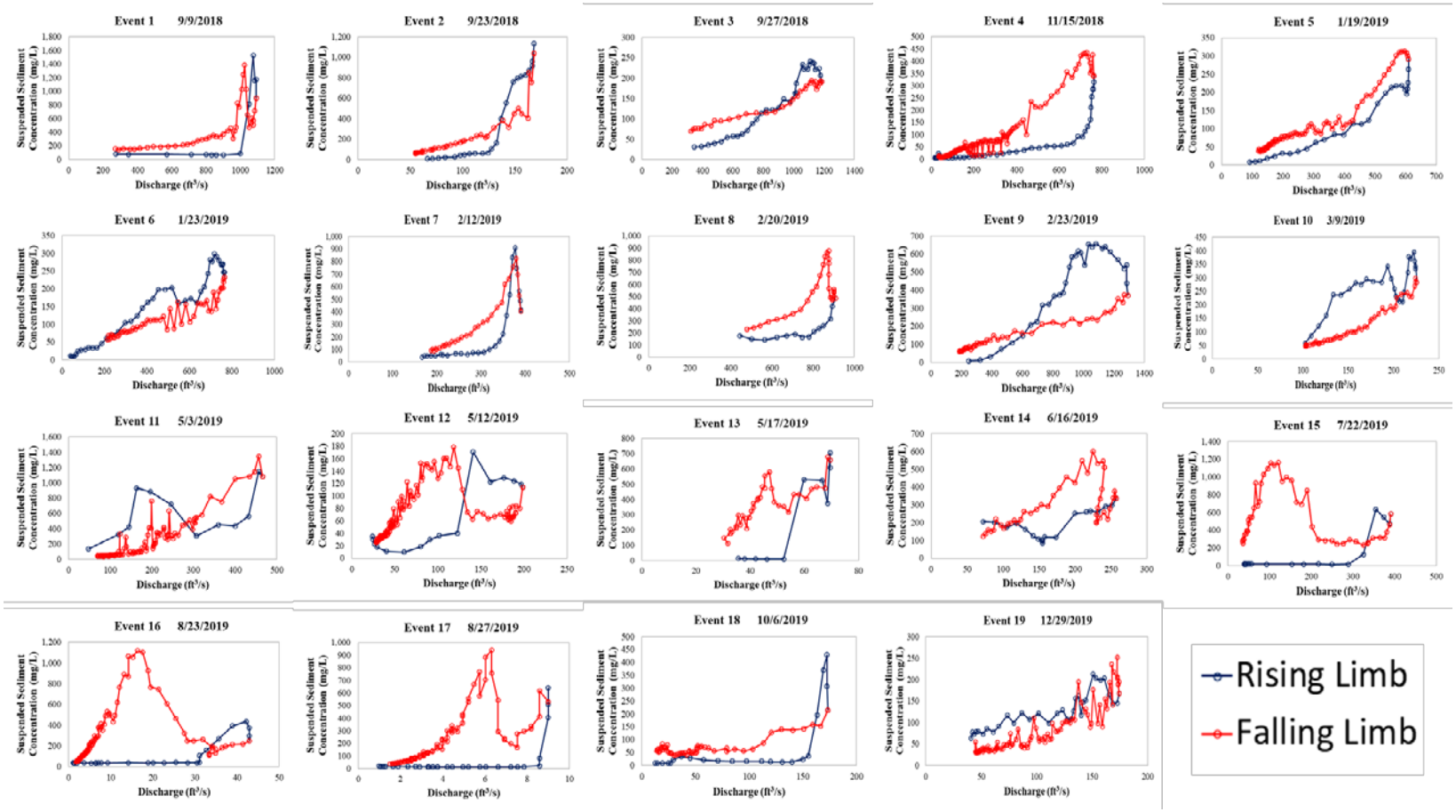

Figure 4.7. The top graph shows the seasonality of the average event hysteresis index. The bottom graphs relate average hysteresis index to 48-hour antecedent precipitation, 96-hour antecedent precipitation, and peak discharge.

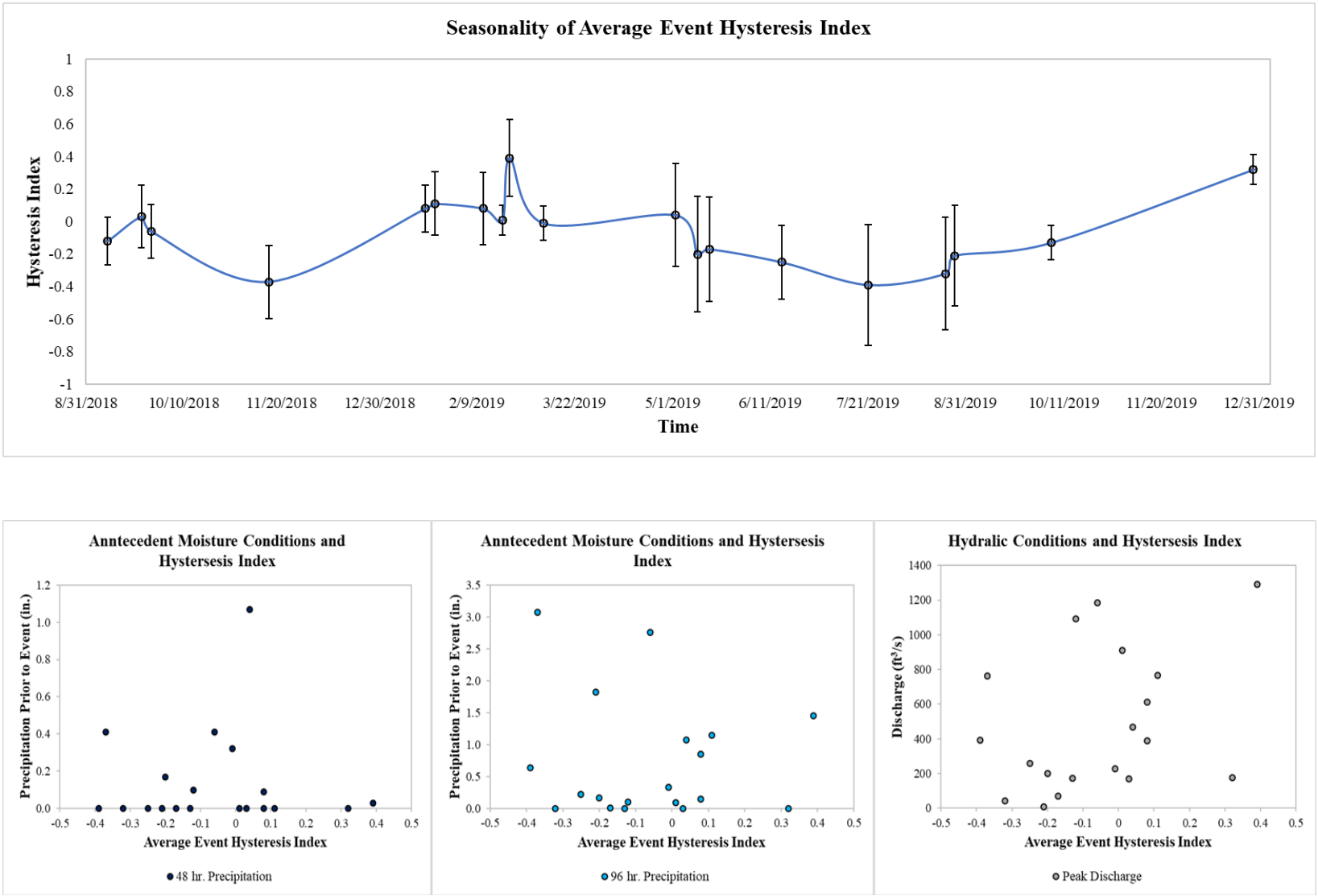

Figure 4.8. Graphical representation of timing of the activation of base load and wash load sources.

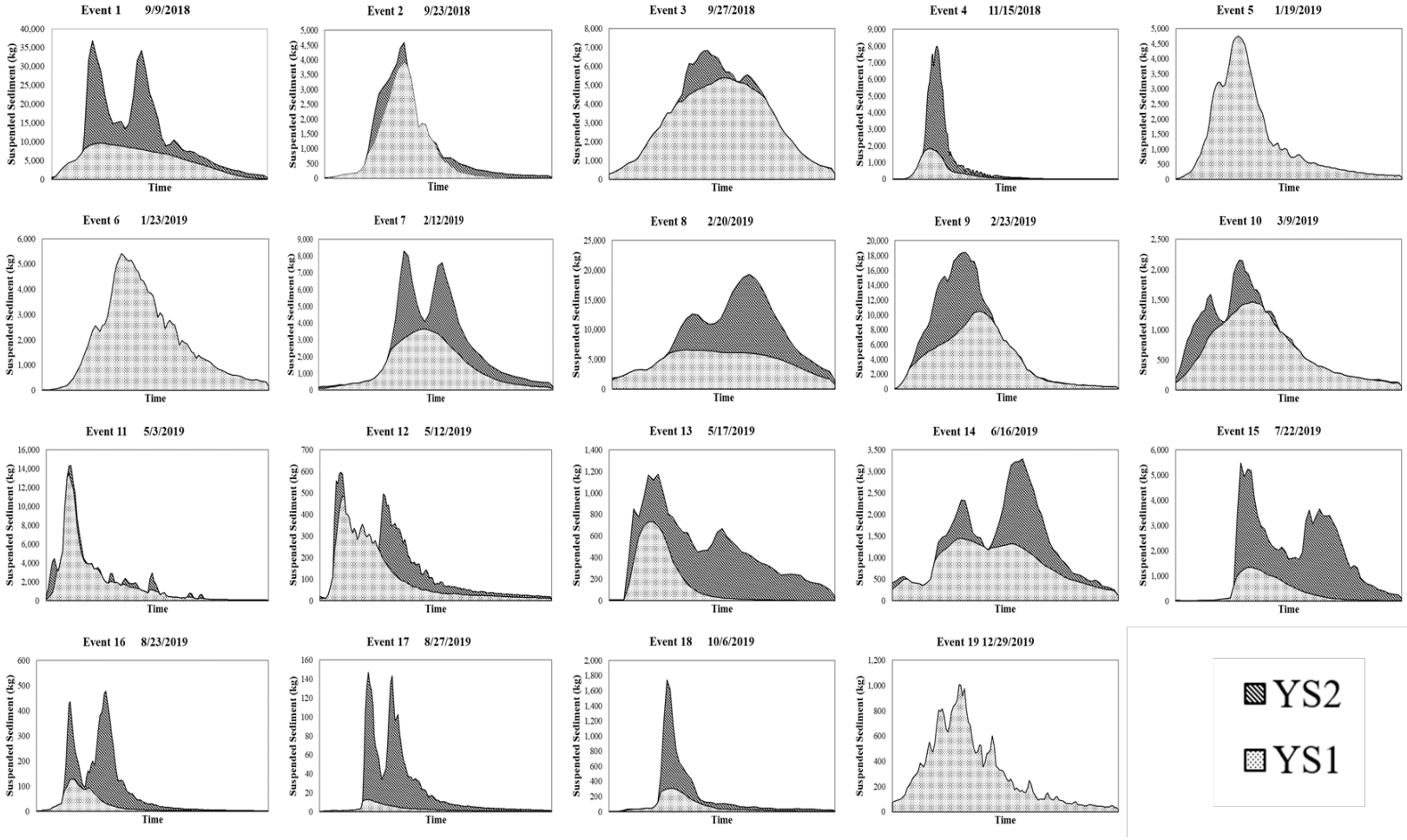

Figure 4.9. Cumulative sediment storage in the floodplain over time.

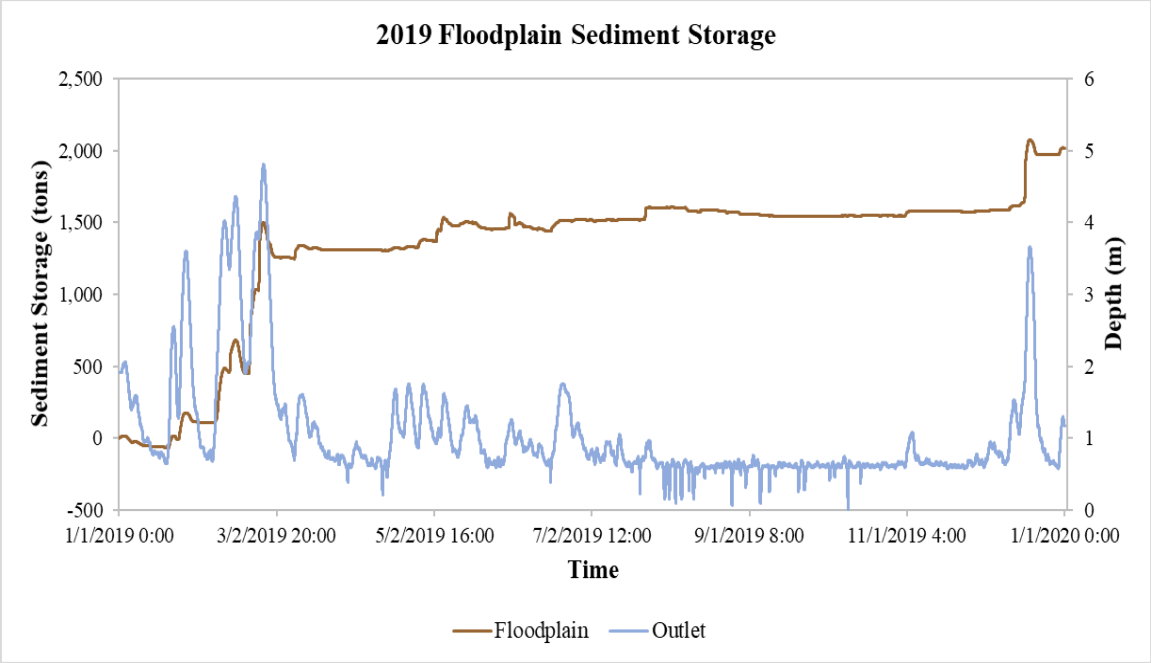

Figure 4.10. Comparison of the turbidity at the upstream and downstream monitoring site for two contrasting events. Event 1 occurred in the summer of 2018 during lower backwater conditions and Event 9 occurred the follow winter of 2019 during high backwater conditions.

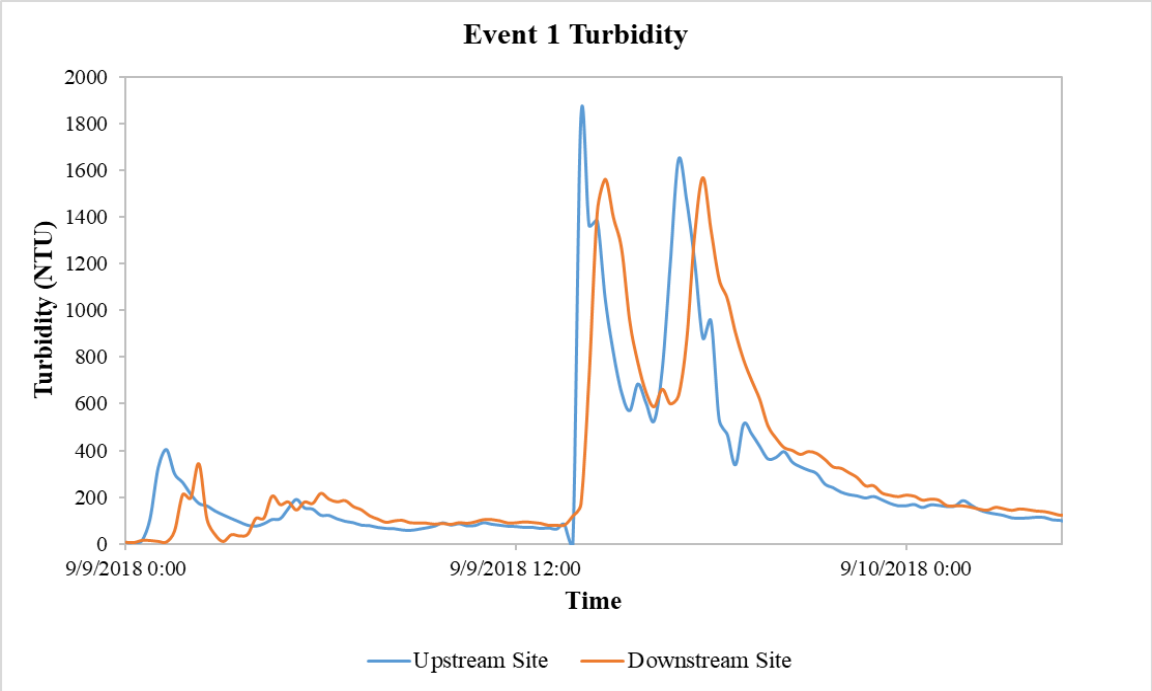

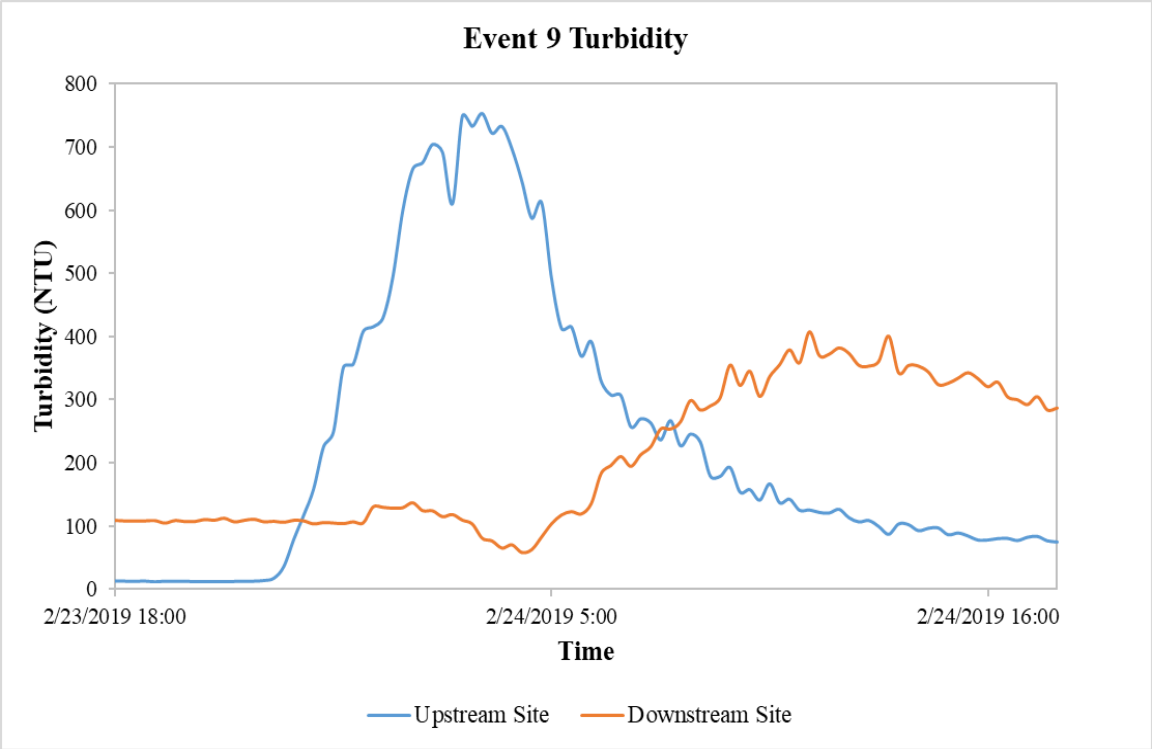

Figure 4.11. Comparison observed, routed, and modeled daily sediment fluxes out at the confluence of Fourpole Creek and the Ohio River.

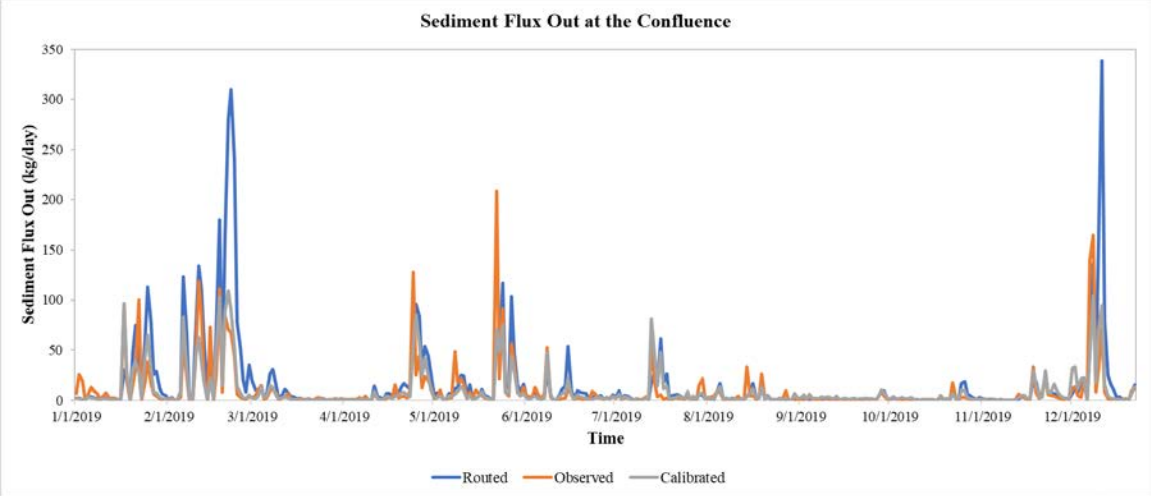

Figure 4.12. Sediment budget for each reach and the total system from the calibrated model results.

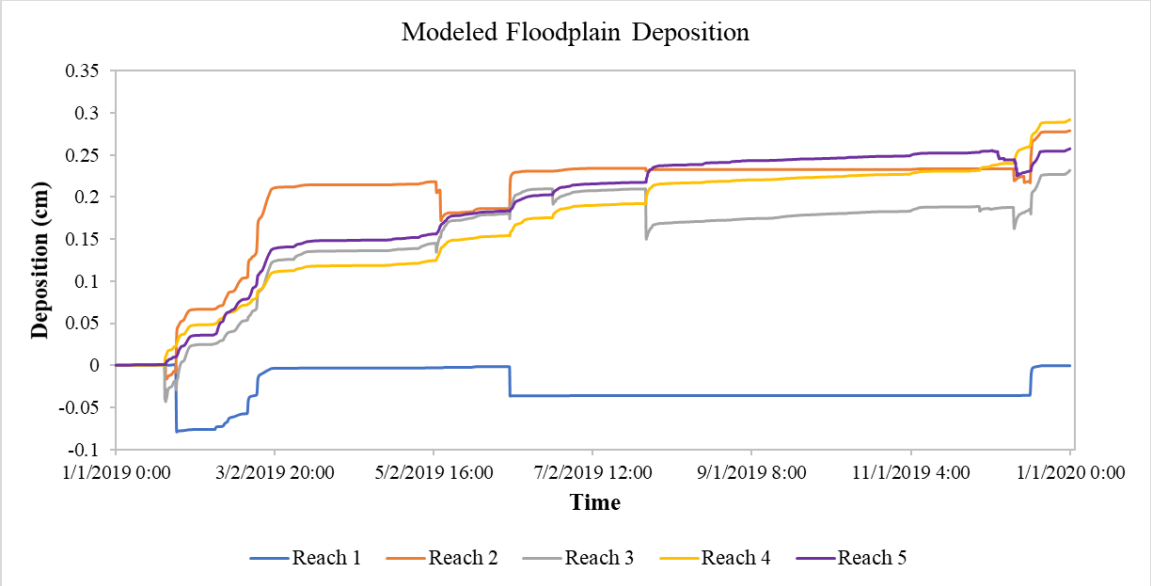

	Reach 1	Reach 2	Reach 3	Reach 4	Reach 5	Total
Floodplain Deposition	329,721	731,893	1,219,333	549,572	684,244	3,514,763
Floodplain Erosion	330,900	201,147	566,118	0	88,791	1,186,956
Streambank Erosion	271,868	0	0	0	0	271,868
Net	-273,047	530,746	653,215	549,572	595,453	2,055,939

Figure 4.13. Depositional patterns in the floodplain for two single line hysteresis events.

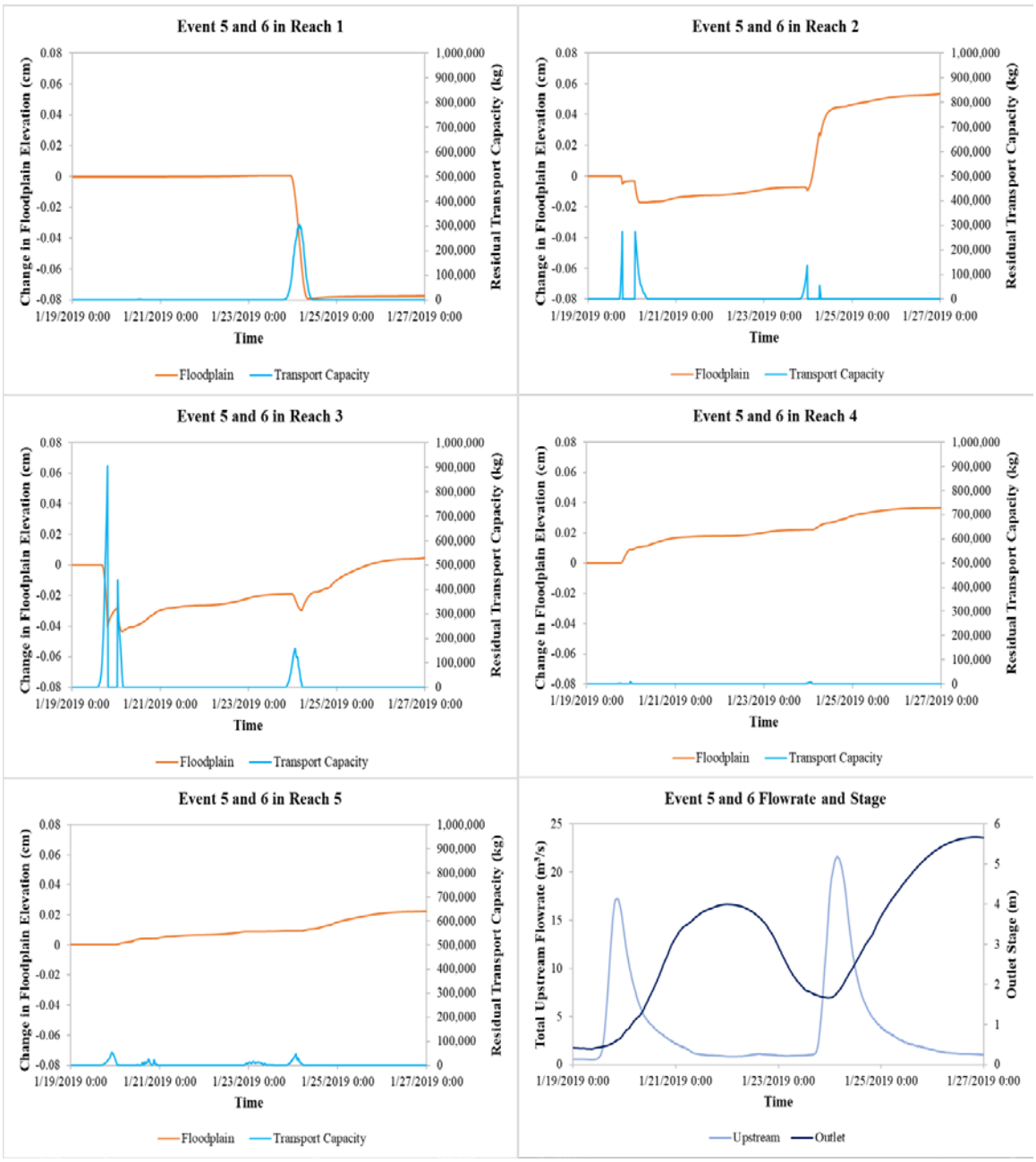

Figure 4.14. Depositional patterns in the floodplain for a counterclockwise figure-8 hysteresis event.

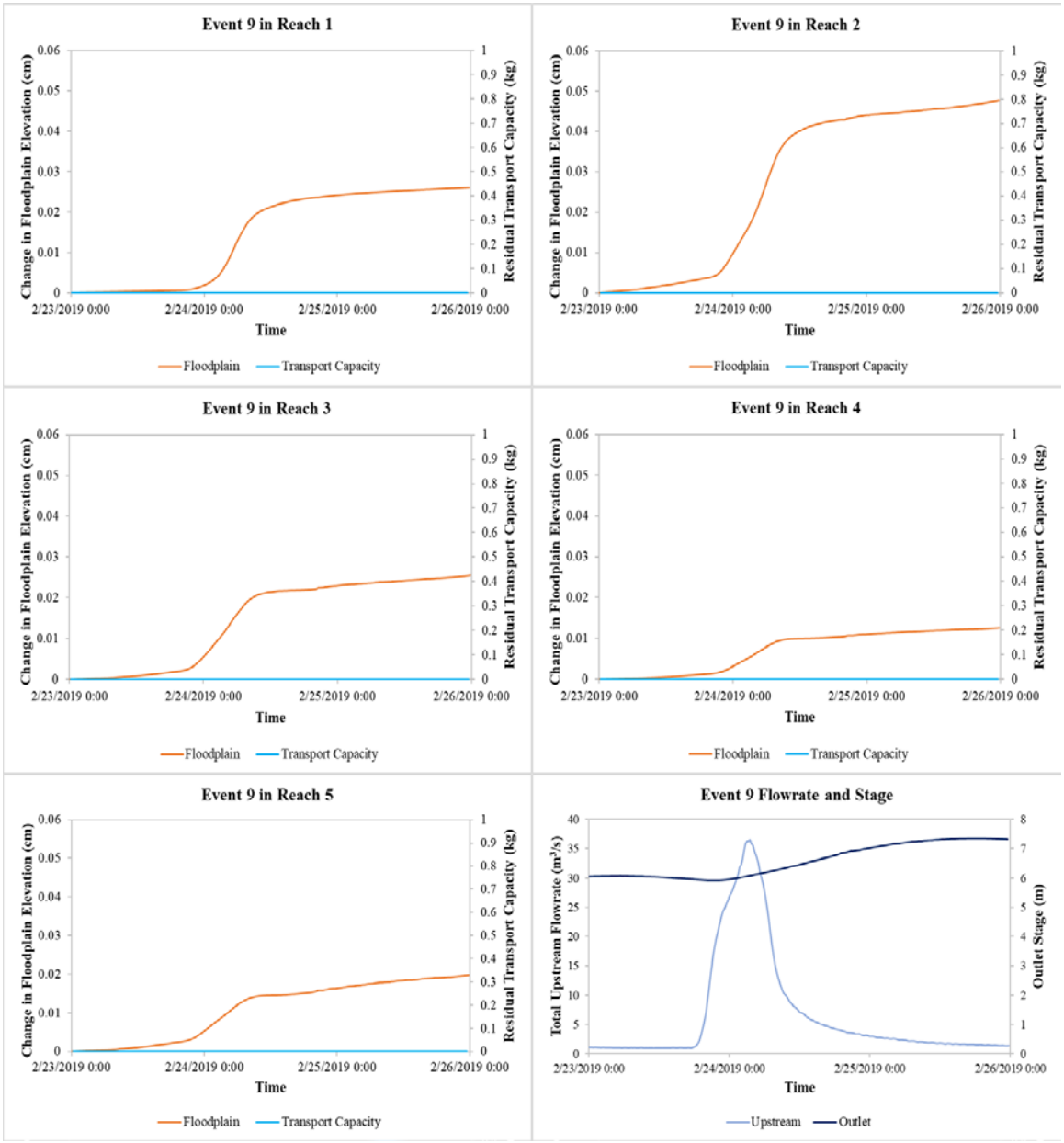

Figure 4.15. Depositional patterns in the floodplain for clockwise hysteresis event.

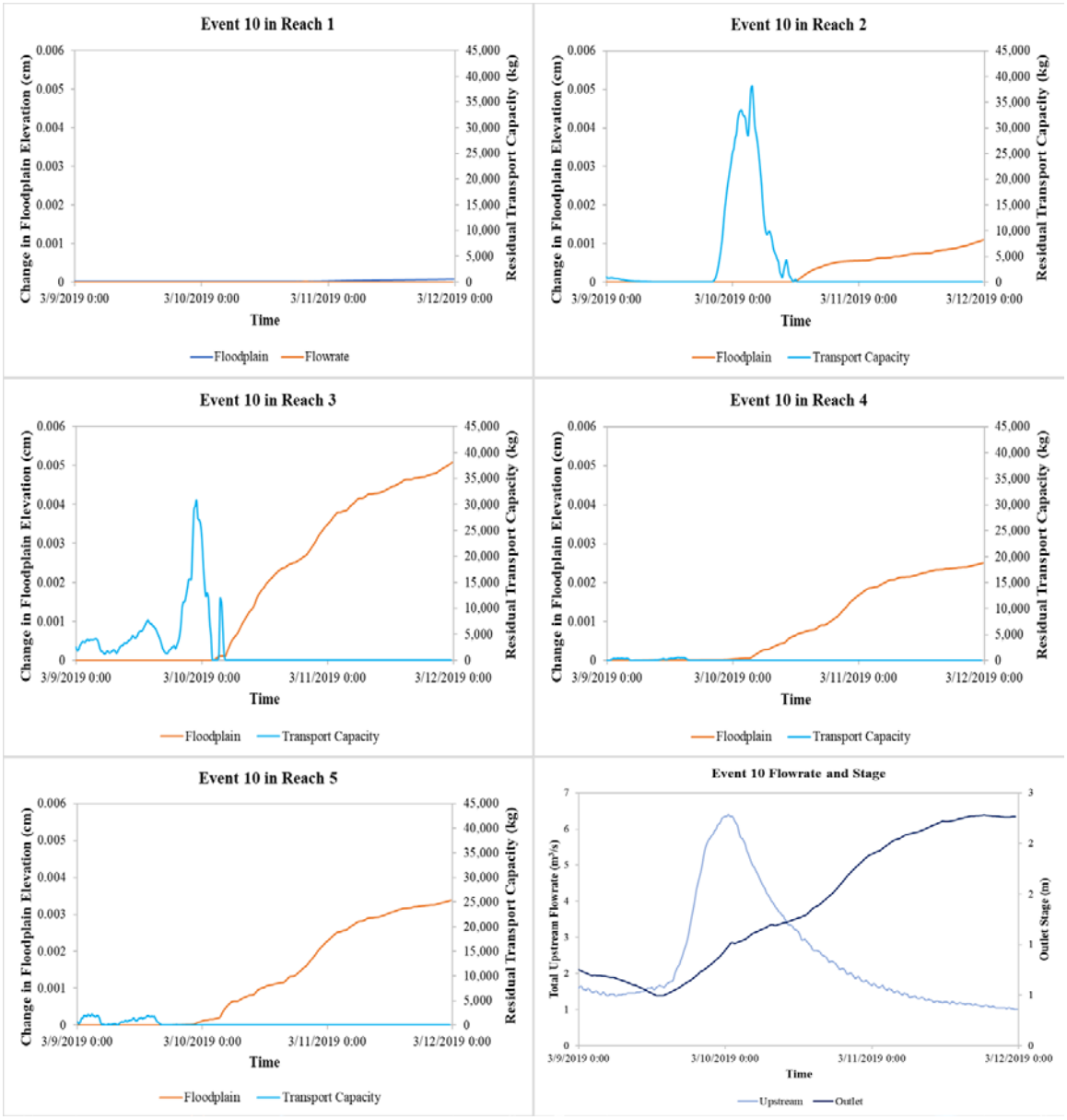

Figure 4.16. Depositional patterns in the floodplain for a counterclockwise figure-8 hysteresis event.

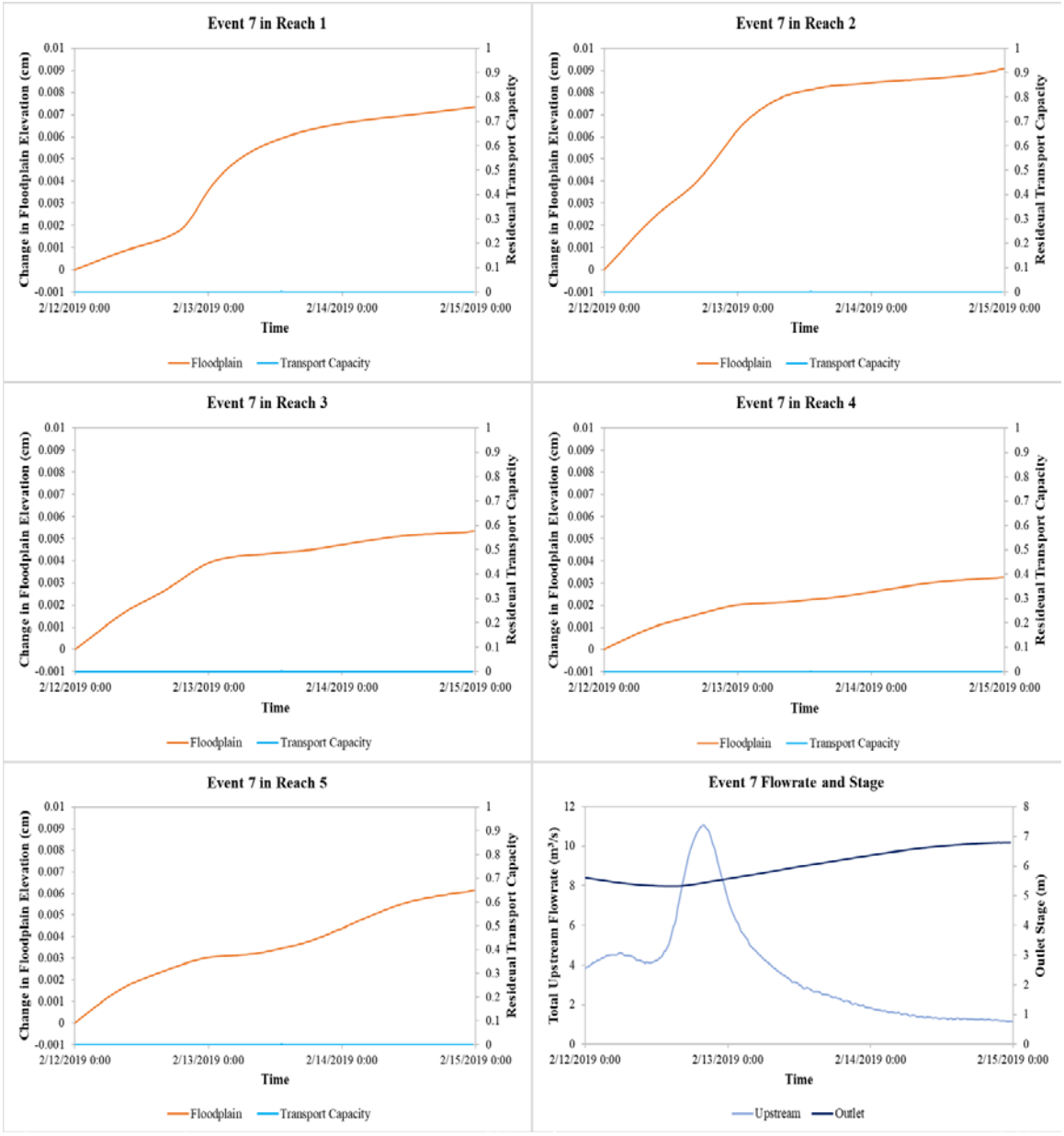

Figure 4.17. Depositional patterns in the floodplain for counterclockwise hysteresis event.

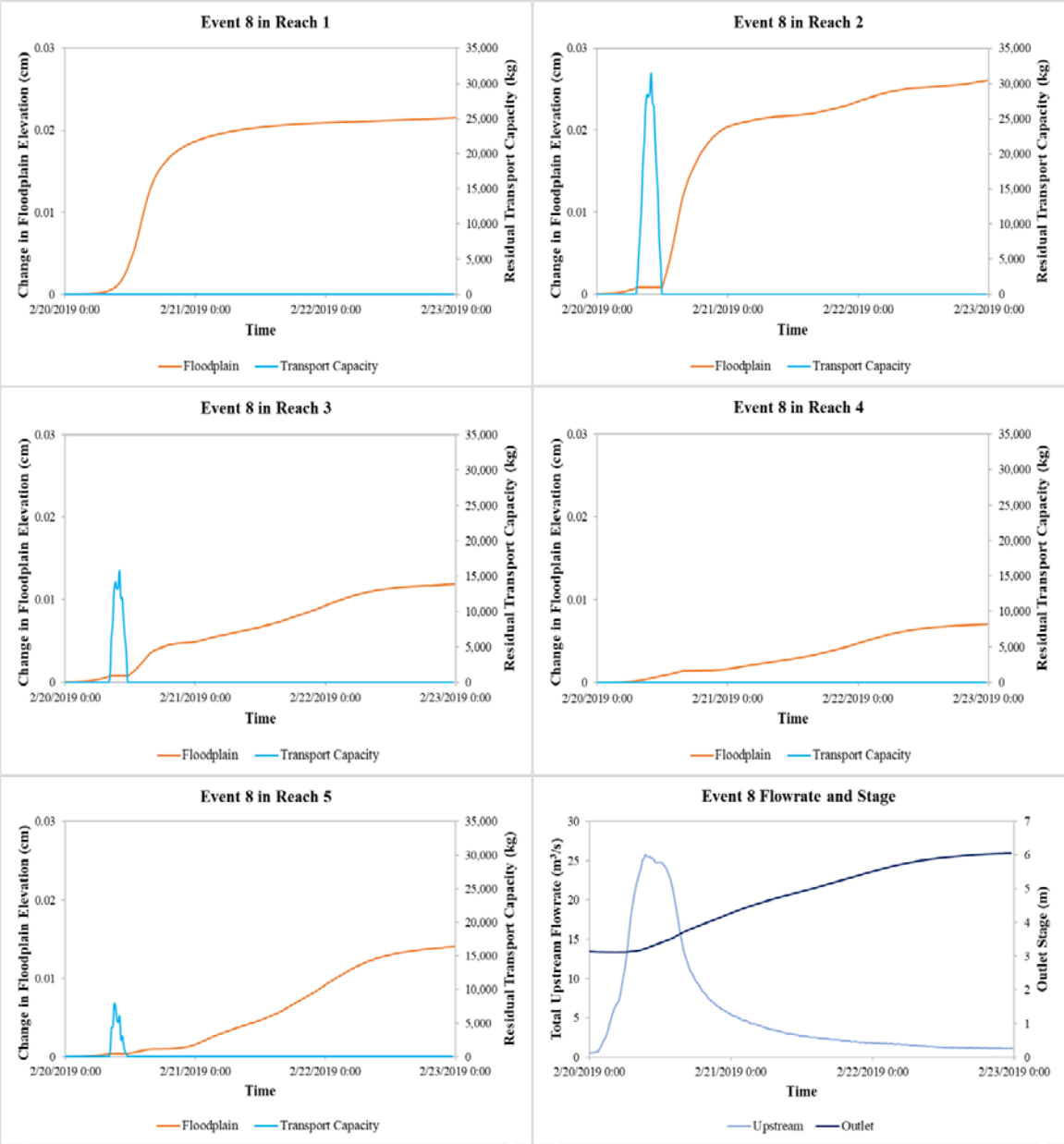

Figure 4.18. Depositional patterns in the floodplain for a counterclockwise figure-8 hysteresis event.

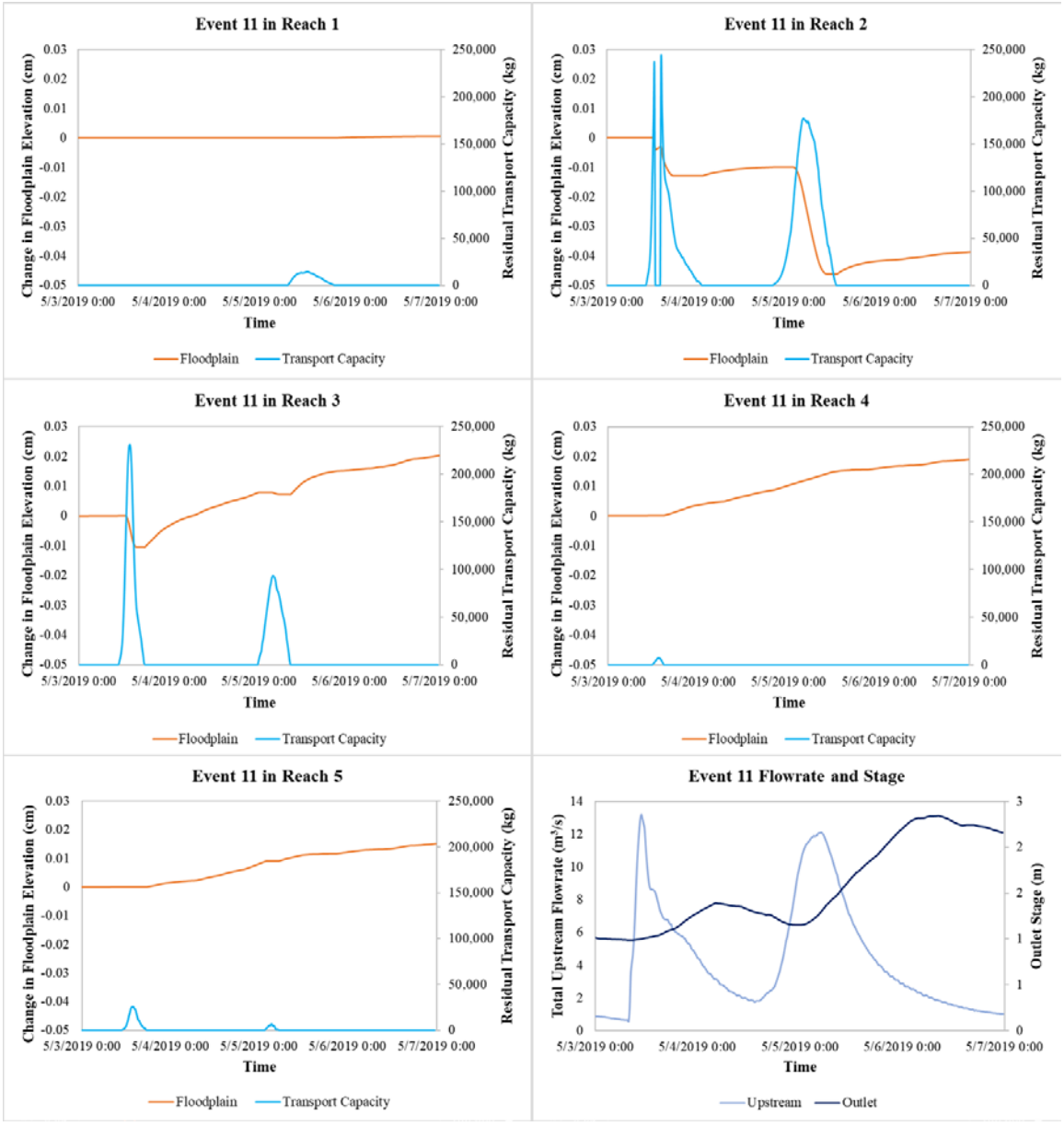

Figure 4.19. Relationship between particulate organic matter (%) vs. turbidity (NTU) from ISCO samples. Four regions were denoted to account for the variability of particulate organic matter content at different turbidity levels.

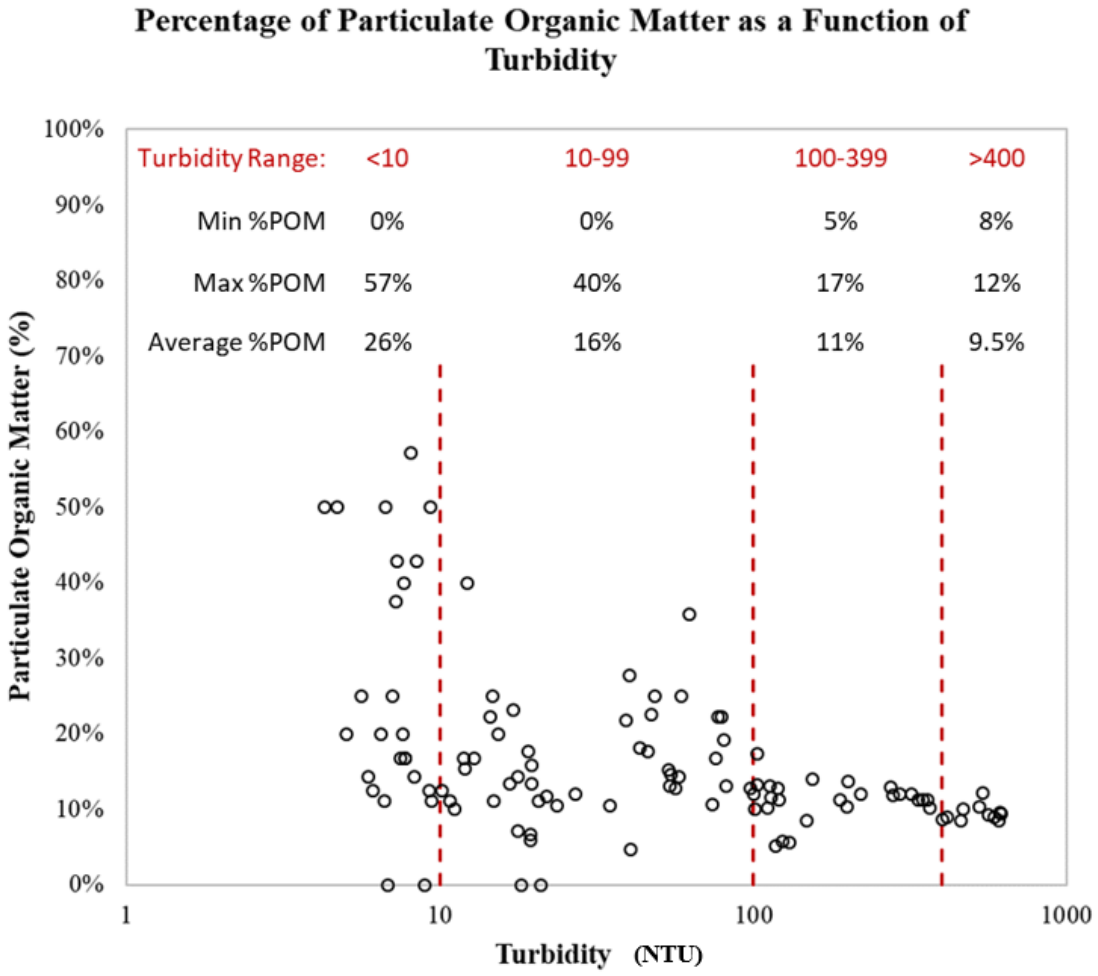

CHAPTER 5. DISCUSSION

5.1 Sediment Yields from Distal Forested Watersheds

Continuous estimates of sediment flux suggest that sediment fluxes from Fourpole Creek are comparable to other regions of Appalachia with watershed disturbances. Reported annual sediment loading estimates throughout Appalachia range from 9.3 t/mi^2-708 t/mi^2, averaging around 135 t/mi^2 (Table 2.1). The continuous sediment model estimated an annual yield of 151 t/mi^2. To validate this, a simple discharge and concentration relationship was used and estimated 194 t/mi^2. This method assumed an average concentration throughout the depth profile, while the Rouse method accounted for the differences in sediment concentration throughout the depth profile. Not accounting for the change in concentration caused a slight over prediction but provided confidence in the continues sediment flux estimations. The annual sediment flux of 151 t/mi^2 is above average, but still within the ranges for sediment yields in the Appalachian region found by other researchers. The studies that reported the highest sediment loadings were influenced by mining disturbances. Watersheds that did not experience mining disturbances had average sediment loadings of 66.4 t/mi^2 (Williams and Reed, 1972; Bolstad et al., 2006; U.S. EPA, 2007; Dun et al., 2013), suggesting that sediment loading in this system is high for a watershed in this region that is not influenced or was previously influenced by mining. This could be attributed to the urban disturbance in this mixed-use watershed. In general, watersheds in this region that have urban disturbances reported larger sediment flux than watersheds that were predominately undisturbed forests (Williams and Reed, 1972; U.S. EPA, 2007). These results suggest that disturbed confluence watersheds of the Western

Allegheny Plateau may be hotspots of sediment to the Ohio River Basin, especially given the limited transit time in the fluvial network before reaching the river.

Results of this study suggest that sediment fluxes may be underestimated using sediment rating curves in mixed-use Appalachian watersheds, stemming from the hysteretic behavior of these systems. Sediment rating curves were found to be a common method for predicting sediment fluxes in Appalachia (Table 2.1), however in this system the sediment rating curve method was found to underpredict annual sediment yields by 77.2%. The sediment rating curves were able to predict similar fluxes to the high-resolution model during lower sediment flux periods. However, the sediment rating curve was never able to accurately predict the event yields, likely due to high variability in the sediment source contributions and the timing of the source activation. Sediment rating curves in disturbed Appalachian watersheds may under-predict sediment flux despite strong regression statistics, which reflects the complex (and variable) hysteretic behavior of sediment transport in these landscapes. This highlights the need of high-resolution sensors to accurately capture sediment dynamics in 'flashy' systems like Fourpole Creek that experience quick increases in discharge and sediment concentrations.

Although this study is likely one of the first to compare sediment flux methodologies in this region, our result corroborates findings that have identified deficiencies in sediment rating curve estimates elsewhere. Lewis and Eads (2009), investigated the performance of the sediment rating curve in a 689mi^2 mountainous watershed that was predominately forested with some agricultural (21%) and urban disturbances (0.2%). In the South Fork Eel River, daily suspended sediment concentrations, when compared to estimates from 10-minute turbidity, poorly represented

the actual patterns and grossly underestimated the daily sediment loads (Lewis and Eads, 2009). Others have suggested that rating curves usually result in poor estimates for three main reasons: 1) suspended sediment concentration is often out of phase with discharge and leads to biases in load estimation, 2) high discharge and sediment concentrations are inadequately represented, and 3) rating curves cannot account for intermittent sediment delivery from erosion events or account for differences between rainfall and snowmelt runoff (Walling and Webb, 1981; Lewis and Eads, 2009). These results suggest caution should be used in sediment rating curves, especially in mixed-use systems considering the potential impacts of temporally varied hysteresis and source activation to influence annual sediment yields.

5.2 Sediment Source Dynamics in Disturbed Appalachian Watersheds

Results of the hysteresis and source unmixing analysis suggest that three important sediment sources in the watershed exert time-varying controls on watershed sediment fluxes throughout the year. Fourpole creek storm events displayed all 5 classes of sediment hysteresis over the monitoring period. The unmixing analysis of the base load and wash load sources found that the contribution of base load and wash load is highly variable from event to event. The base load source contributed 100% for some events while others it only contributed 13%. Antecedent moisture conditions could be a possible factor impacting the contribution of the two types of sources. During the events in summer of 2018 there was some precipitation in the 48 hours prior to the event and the base load sources dominated those three events. However, in the events of summer 2019 there was no precipitation in the 48 hours prior to the events and the wash load sources were the dominant sources for those events. The time between events could also be a factor impacting the contribution of

the two source types. In summer 2018, three events occurred in two and a half weeks. The first event in the series had a high amount of precipitation and very high sediment load. The first storm event likely washed out all the unconsolidated bed material and there was not enough time between the following two events for material to be redeposited, resulting in more erosive processes to occur. While temporal variability of sediment sources is important for watershed managers source origin is also a critical consideration for holistic management strategies. The potential sources of different sediment contributions are discussed in the following paragraphs.

Results of the sediment source unmixing suggest that the baseload (YS1) is likely associated with the in-channel and gully erosion. The contribution of the YS1 component to event sediment yields is highly variable and may be enhanced by the urban portions of the watershed. In-channel erosion has been recognized as the major contributor to long-term sediment yields in urban watersheds, on average accounting for about two-thirds of the annual sediment yield (Trimble, 1997). Initial fluxes runoff quickly from impervious areas and the remainder of the storm runoff has high sediment shear stresses and transport capacities. The erosive power of the channel flow results in sediment production from the channel network through the weathering of bed and bank material (Megnounif, 2013). Additionally, gully erosion has been associated with watersheds that experience anthropogenic activities such as the removal of vegetation and soil disturbance. While gully erosion is most commonly documented in agricultural environments, high erosion rates have also been observed in urban areas especially during construction (Wolman, 1967; Gudino-Elizondo et al., 2018).

The first wash load source (YS2-a) is likely associated with freshly deposited sediments that were deposited throughout the fluvial network on the receding limb of the previous event. The wash load (YS2) represents the supply of new sediment sources that become available such as material from hillslopes, bank caving, and re-suspension of fresh deposits (Megnounif, 2013). YS2-a was shown to correlate well with the antecedent precipitation. The YS2-a component was found to be a higher percentage of the wash load during events with high antecedent precipitation 96 hours prior to the event. This corroborates the idea that YS2-a could be freshly deposited sediments since it contributes a higher portion of sediment during events that occurred closely after another precipitation event. Although high antecedent moisture conditions have also been shown to cause more upland connectivity, this is not a likely source of YS2-a. During these conditions distal sediment sources become connected and typically produce the counterclockwise hysteresis loops, however counterclockwise patterns typically had a higher contribution of the YS2-b source, not the YS2-a source.

The second wash load source (YS2-b) potentially reflects upland hillslope erosion from urban areas or, more likely, subsurface macropore erosion from forested soils. Counterclockwise and counterclockwise figure 8 hysteresis loops were found to be the most common in our watershed. Counterclockwise hysteresis is often found to occur in urbanizing basins with high sediment availability. The stormwater runoff dilutes suspended sediment on the rising limb and upland sediments arrive on the falling limb on the hydrograph. Gellis (2013) compared hysteretic behavior of four watersheds with primary land uses. It was found that an entirely forested watershed experienced clockwise hysteresis loop for about 80% of the storm events and the predominately urban (with forested

disturbances) produced counterclockwise loops for over 50% of the events. Contrary to Gellis (2013), Wymore et al. (2019) showed peak concentrations on receding limbs of the hydrograph in a forested watershed. Their study attributed these peaks to connectivity of macropore channels, and subsurface sediment erosion to the fluvial network (Wymore et al., 2019). Laboratory-scale studies have shown that during warm conditions, macropores develop thin, easily erodible surface crusts along macropore walls that are eroded during subsequent events (Wilson et al., 2018). For the Fourpole Creek watershed, counterclockwise loops and negative HI values often occurred in warm summer months, YS2-b contributions were found to increase with decreasing antecedent moisture, and forested landcover was predominant in the watershed. These lines of evidence would suggest macroporous subsurface erosion in forested areas as the most likely sediment source.

Timing of sediment source delivery have important broader implications for regulated rivers such as the Ohio River. The YS2-b source was the primary sediment source occurring in the dry summer prior to the HAB that occurred on the Ohio River in late September 2019. This is significant given baseflow of the regulated river promotes favorable conditions to retain sediments and sediments have been recently recognized to increase HABs through seeding the river with harmful cyanobacteria, supplying nutrients for HAB growth, and providing a competitive advantage for HAB proliferation by creating adverse conditions for green algae (Kitchens et al., 2018; Paerl and Huisman, 2008; Walsby, 1997; Levy 2017). The source is a critical origin given that urban systems make up a smaller proportion of the Western Allegheny Plateau which is the major source of water for the Upper Ohio River Basin, as compared to forested cover (Omernik, 1987).

Further work is needed to more explicitly investigate source origin of these sediments and to understand their fate in the riverine environment.

5.3 Sediment Retention in Confluence Floodplains

Sediment retention and deposition processes related to wetlands play an important role in regulating downstream water quality. Riparian wetlands located along low order streams have been found to be important sites for sediment retention (Whigham et al., 1988). For Fourpole Creek, 40% of the total inputs into the confluence floodplain were retained. No studies to our knowledge have quantified sediment depositional fluxes in backwater confluence floodplains of Appalachian watersheds, but one study measured sediment deposition in floodplain confluences in tributaries of the Chesapeake Bay. Since only the upstream inputs were measured, the floodplain retention was reported as the proportion of each river's annual load upstream of the floodplain. Sediment accumulation in the floodplains represented from 30% to 690% of the tributaries' sediment loads (Noe and Hupp, 2009). When the results for our system were reported this way, sediment accumulation in the floodplain represented 60% of the tributary's sediment loads, falling within the retention range of other confluence floodplain systems. Sediment retention has been found to be strongly associated with river sediment loads and percent retention of sediments has been found to positively correlate with floodplain inundation (Noe and Hupp, 2009). Our results corroborate this finding. 66% of the annual net retention occurred during the first 3 months of the year when the outlet stage causes long periods of high inundation. Since floodplain deposition can only occur during infrequent high-magnitude storm events, event retention rates were also examined. Of the events in which the floodplain was a sink, retention rates were found to range from 21% to as high as 96%.

The event retention was highest during periods of high inundation and on average 72% of the winter event inputs were retained in the floodplain. These results show that floodplains have a quantitatively large role in intercepting and storing sediment inputs. Therefore, efforts to limit downstream sediment loads should ensure the function of floodplains is maintained or enhanced through floodplain restoration. Watershed management strategies to improve floodplain connectivity can include strategies as simple as sloping back vertically eroded streambanks and planting vegetation. Other times the stream channel needs to be completely restored by adjusting channel dimensions and meander patterns to better accommodate the water it conveys and allowing for better floodplain access. Regardless of the management strategy, the main goal of floodplain restoration is to achieve a well-connected hydrologic system that maintains floodplain function to intercept sediment and improve downstream water quality.

5.4 Numerical Modeling of Sedimentation Dynamics in Confluence Floodplains

The numerical modeling of sedimentation dynamics provided interesting insight into the spatial and temporal patterns associated with the deposition occurring in the floodplain. Although sediment retention in the floodplain is not always indicative of floodplain deposition, typically over long periods of time retention rates can be a good predictor of depositional rates. The model found that 95% of the sediment retained in the floodplain was deposited. However, depositional and erosional rates in the floodplain cannot be inferred from retention rates alone. Although net deposition in the floodplain was 2,055 tons, 3,515 tons was simulated to be deposited, 34% of which were subsequently eroded. Using numerical modeling to simulate sediment transport dynamics provides

valuable insight into the behavior of the floodplain system that would remain unknown if net retention is only examined.

The sediment transport model found unique differences in reach scale sedimentation dynamics. The floodplain in Reach 1 was found to slightly degrade by 0.004mm while Reach 5 was found to aggrade 2.6mm over the year. Reach 2,3, and 4 experienced similar deposition with floodplain depositions of 2.8, 2.3, and 2.9mm respectively. These findings are in line with the accretion rates of 0.4-4.8mm a year that other confluence floodplain systems have reported (Noe and Hupp, 2009). Reach 4 experienced the highest deposition likely due to the lower fluid sheer stresses that occur in this as a result of the opposing flow conditions of Fourpole Creek and the Ohio River during periods of high inundation. These findings suggest confluence floodplains may have 'stagnation zones' stemming from opposing hydraulic controls where erosion is minimal, and deposition is most pronounced.

Hysteresis was found to influence the spatial variability of erosion and deposition mechanisms. Counterclockwise hysteresis patterns upstream of the confluence floodplain were found to deposit more sediment in the upstream reaches while clockwise hysteresis patterns were found to deposit more sediment in the downstream reaches. This is likely a complex result of differences in hydraulic and hydrologic conditions, but the residual transport capacities provided some insight to why this is occurring. The residual transport capacity prior to an event is very low. As the flowrate begins to increase at the upstream site so does the fluid shear stress causing an increase in residual transport capacity. If the fluid shear stresses become higher than the critical shear stress of the floodplain material, erosion occurs. Once the fluid shear stresses begin to decrease so do the transport capacities

causing deposition to occur. This decrease in fluid shear stress typically occurs on the falling limb of the hydrograph, but the downstream reaches can experience this decrease sooner as the outlet stage often buffers the flowrates during periods of high inundation. The clockwise hysteresis loops occurred during lower outlet stages and subsequent higher shear stresses and transport capacities not allowing immediate deposition when the flow is first relieved into the floodplain. In contrast, the counterclockwise hysteresis loops occurred during higher outlet stages and low shear stresses. This resulted in lower transport capacities allowing for immediate deposition as the flow enters the floodplain.

Since hysteresis patterns are indicative of sediment source activation, it is also likely that there is subsequent spatial variability in the sediment source composition of backwater confluence floodplains. Counterclockwise patterns typically indicate a dominance of upland sediments while clockwise patterns indicate a dominance of sediment from instream sources. This would suggest in general that the upland sediments are deposited higher up in the floodplain while in stream sediments are deposited farther downstream. This could have potential implications for HABs on the Ohio River. Recent research has shown that sediment in tributaries can house high levels of phytoplankton, including Microcystis and suggest rivers as a potential source of inocula for summer blooms (Conroy et al., 2014). The annual cycle of Microcystis begins with an overwintering period in the upper layers of bed sediments and do not move into the water column until water temperatures rise in late spring. In 2019, the clockwise events occur in the early spring transporting in-channel sediment and possibly Microcystis into the floodplain where it is deposited near the outlet and discharged to the Ohio River. Several net erosive events occurred in the late spring and summer of 2019, potentially mobilizing

Microcystis living in the floodplain and inoculating the Ohio River bloom in the late summer of 2019.

5.5 Implications for N Budgets

Our results suggest that particulate N fluxes from disturbed forested watersheds near rivers should be considered as a N source for HABs in regulated rivers. The particulate N yield for Fourpole Creek was estimated to be 2.29-4.74 kgN/ha/year which is similar to the nitrate yields of 3.6 kgN/ha/year in this same watershed (Jensen and Ford, 2019). Based on a recent literature review we find that these particulate N fluxes are on the same order of magnitude as nitrate loading in other disturbed forested watersheds (Goodale et al., 2019; Carey et al. 2014; Jensen and Ford, 2019). This flux may be particularly important in confluence watersheds given that much of the flux from these watersheds are delivered directly to the river system (Alexander et al., 2008). While nitrate will advect downstream and have limited residence times in regulated rivers, such as the Ohio River, large proportions of particulate N may deposit to the riverbed (Alexander et al., 2008; Inamdar et al., 2015). Although cyanobacteria typically prefer ammonium, cyanobacteria are able to obtain nutrients from sediment by either dropping to the bottom to acquire sediment bound nutrients or through mineralization and regeneration processes that release nutrients from the sediment back into the water column (Walsby, 1997; Levy 2017). The mineralization of organic matter can significantly increase the ammonium, the highest preference N species, and phosphate in the sediment porewater. These findings suggest study of the fate of particulate N in regulated rivers should be investigated as a potential source of N to fuel HABs.

The PN yields are similar to exports found in temperate forested watersheds. Inamdar et al. (2015) reported very similar PN exports of 4.2kgN/ha/yr in a forested watershed in Maryland. A study in the Wailuku River in Hawaii reported lower PN exports ranging from 0.63-1.27 kgN/ha/yr (Wiegner et al. 2009). Other studies that reported PN exports were found in more tropical climates that experience high intensity storm events and subsequently had high PN exports ranging up to 17 kgN/ha/yr (Lloret et al., 2013). In the future as the climate changes, higher intensity storms with higher peak flow are anticipated, suggesting other regions could be subject to PN exports as high as or maybe even higher than what the tropical systems are currently experiencing (Inamdar et al., 2015). Additionally, given that the sediment fluxes in this system are similar to the sediment fluxes throughout Appalachia, other mixed-use watersheds are likely to experience similar PN fluxes and the combined fluxes could be heavily influencing the nutrient loads in the Ohio River.

The depositional fluxes of particulate nitrogen in the confluence floodplain wetland is estimated to be on the same order of magnitude as the removal of nitrate. The floodplain was found to have removed from 0.5-0.89kgN/ha/yr. A previous study conducted in this watershed, found that the confluence floodplain wetland had a nitrate removal rate of 0.46 kgN/ha/yr which is nearly identical the particulate nitrogen removal in this system (Jensen and Ford, 2019). Olde Venterink et al. (2006) had similar findings in a mixed-use watershed in the Netherlands, suggesting that the N retention through sediment was of a comparable magnitude to denitrification rates in the floodplain system. Identifying the subsequent fate of PN following deposition is an important area of future work and has significant potential implications for N budgets in confluence floodplain wetlands.

CHAPTER 6. CONCLUSIONS AND FUTURE WORK

6.1 Conclusions

The measured sediment yields in this system were found to be comparable to other regions of Appalachia. Different variations of a sediment rating curve were found to be the common methodology for estimating sediment yields in the Appalachian region. Sediment yields estimates from a data driven high-resolution model were compared to estimates using a sediment rating curve. The continuous sediment yield model estimated an annual yield of 151 t/mi^2, while the sediment rating curve estimated a suspended sediment yield of 34.3 t/mi^2 for the same monitoring period. This 77.7% underprediction is likely due to high variability in the sediment source contributions and the timing of the source activation in mixed-use watersheds.

Sediment pathway dynamics were quantified by coupling sediment hysteresis analysis with sediment source unmixing methods. Hysteresis analysis results displayed a variety of hysteresis loop types and magnitudes. Seasonality was found to be an indicator of the hysteresis index with strong negative HI values occurring in the winter and weak to moderate positive HI values occurring in the summer. Results of the hysteresis and source unmixing analysis suggest that the three important sediment sources in the watershed exert time-varying controls on watershed sediment fluxes throughout the year. Source 1 was likely found to be in-channel and gully erosion. Source 2 was likely freshly deposited sediment throughout the fluvial network. Source 3 was likely found to be erosion from upland hillslopes or erosion of the subsurface macropores in the forested soils. The timing and the contribution of these sources was highly variable from event to event. Partitioning of sediment source dynamics have important broader implications for regulated rivers such

as the Ohio River since Source 3 was found to be the primary sediment source during the summer prior to a HAB.

Confluence floodplains were found to have a quantitatively large role in intercepting and storing sediment inputs. In our system, 40% of the total inputs into the confluence floodplain were retained annually and event sediment retention was found to be as high as 96%. During the winter inundation is the highest and 66% of the annual net retention were deposited in these three months demonstrating the ability confluence have to buffer sediment fluxes from small tributaries to large riverine systems.

The numerical modeling of sedimentation dynamics provided more insight into the sedimentation dynamics occurring in the floodplain. Although net deposition in the floodplain was 2,055 tons, 3,515 tons was actually deposited, 34% of which were subsequently eroded. Sediment dynamics were found to be different in each reach of the floodplain. Reach 1 was found to slightly degrade and Reach 4 was found to aggrade the most with a yearly increase of 2.9mm. Hysteresis was found to influence the spatial variability of erosion and deposition mechanisms in the floodplain. Counterclockwise hysteresis patterns upstream of the confluence floodplain were found to deposit more sediment in the upstream reaches while clockwise hysteresis patterns were found to deposit more sediment in the downstream reaches. This would suggest in general that the upland sediments are deposited higher up in the floodplain while in stream sediments are deposited farther downstream, potentially influencing HABs on the Ohio River.

Our results suggest that particulate N fluxes from disturbed forested watersheds near rivers should be considered in watershed N budgets as well as a source for HABs in regulated rivers. The particulate N yield for Fourpole Creek was estimated to be 2.29-4.74

kgN/ha/year which is similar to the nitrate yields reported for this watershed and on the same order of magnitude as nitrate loading in other disturbed forested watersheds. Similarly, the depositional fluxes of particulate nitrogen in the wetland was found to be on the same order of magnitude as the removal of dissolved nitrogen. The floodplain was found to have removed from 0.5-0.9kgN/ha/yr which is very similar to the nitrate removal rate in this system.

6.2 Future Work

While the results of this research provide insights into the sedimentation dynamics occurring in the Fourpole Creek watershed and confluence floodplain, more research is needed to be able to fully understand the sedimentation processes and controls. Some uncertainty still remains in the sources of the three main sediment contributions. Sediment fingerprinting could be used to determine exactly what the three sources are to provide a little more insight to the source unmixing results. Additionally, a watershed model could be developed to determine where in the watershed the three sources are coming from. Although spatial patterns in sediment source deposits were hypothesis in the floodplain, sediment fingerprinting of floodplain sediments could provide more information. Additionally, aerial imagery or DEMs could be used to investigate long term deposition and asses sediment accrual gradients. The sediment transport model was only designed to investigate longitudinal deposition dynamics it could be adapted to also predict lateral deposition in each reach. Deposition in the floodplain was currently modeled as a lumpsum of inputs from both Fourpole Creek and the Ohio River, however unmixing these two inputs could provide interesting spatial variation in the depositional patterns of the two inputs. Lastly, more information is needed to determine exactly how tributaries and

confluence floodplain wetlands influence HABs. Microbial sampling of headwater tributary sediments could be performed to check for the presence of Microcystis and its potential relative abundance to see if it is possible for tributaries to seed HABs in Appalachia.

APPENDIX

APPENDIX A. Field Notes

Field Notes 8/31/2018

Floodwall Station:

- New YSI deployment 8/31- first measurement at 5pm EST
- Water depth: 40cm
- SUNA Reference Spectrum Issue. Austin emailed corrected cal file
- SUNA was removed around 4:45pm and deployed around 7:25pm

Upstream St. Cloud:

- Deployed YSI at 7:55pm- first measurement at 8:00pm
- Cage is 3in above the bed
- Water depth: 55cm
- Sediment depth was too small to measure

Field Notes 9/25/2018

Upstream St. Cloud:

- Austin retrieved the sonde at 11:15am and returned it to the field at 5pm
- pH probe did not calibrate well
- Did not calibrate fDOM because he did not have the sulfuric acid
- Did not calibrate conductivity since it had not drifted
- Water depth 81.3cm
- Water was relatively high and turbid

Field Notes 10/9/2018

Floodwall Station:

- Drift check at 11:45am
- Austin retrieved the sonde at 12pm and returned it to the field at 5:30pm
- Did not calibrate fDOM because he did not have the sulfuric acid
- Did not calibrate conductivity since it had not drifted
- Water depth 86.4cm
- Water was relatively high

Upstream St. Cloud:

- Austin removed the faulty pH probe and replaced the port with a plug
- Pulled the data and redeployed the sonde around 12:30pm
- Water depth: 50.8cm
- Water was low flow and clear

Field Notes 10/12/2018

Floodwall Station:

- SUNA Reference Spectrum was updated
- SUNA was removed around 10am and returned around 11am
- Deployed SonTek- first measurement was at 12:15pm

Upstream St. Cloud:

- Cross section survey taken
- Long profile survey taken
- Water depth: 1.4ft

Field Notes 10/24/2018

Upstream St. Cloud:

- Drift check at 10:15am
- Austin retrieved the sonde around 10:30am and redeployed 10/25 at 2:30pm
- Water depth: 47cm

Field Notes 11/9/2018

Floodwall Station:

- SonTek was unplugged
- Water was too high to update SUNA reference spectrum

Upstream St. Cloud:

- Storm samples were taken from 3:00pm to 5:00pm
- Water was too high to put pH probe in YSI

Field Notes 11/19/2018

Upstream St. Cloud

- Drift check at 2:30pm
- Austin retrieved the sonde at 2:30pm and redeployed 11/20 at 3:45pm
- Conductivity was not calibrated since it was not needed
- Water depth: 56.5cm
- Some debris and log build up on the inside of the culvert

Field Notes 12/3/2018

Upstream St. Cloud:

- Culvert was cleaned out from 10am to 1pm- flag the YSI data during this time
- 6 sediment samples were collected from 2:45-4:00pm

Field Notes 12/10/2018

Floodwall Station:

- Austin retrieved the sonde at 3:30 and redeployed at 4:15pm 12/11
- 3 in of sediment on the cage
- fDOM did not calibrate well
- Water was a greenish tint

Field Notes 12/20/2018

Upstream St. Cloud

- Austin retrieved the sonde at 11am and redeployed 12/27 at 2pm
- About 6 in of sediment deposited on the culvert bed but was gone when redeployed a week later
- Batteries died on 12/10/18
- Water depth 53.3cm

Field Notes 1/16/2019

Floodwall Station:

- Drift Check at 10am
- New YSI deployed at 9am
- Collected ISCO samples
- Set ISCOs to collect new samples

Field Notes 2/4/2019

Floodwall Station:

- Collected ISCO samples
- Set ISCOs to collect new samples

Upstream St. Cloud:

- Drift check at 10:30am
- Sonde was swapped with calibrated sonde at 10:45am

Field Notes 3/13/2019

Floodwall Station:

- Collected ISCO samples
- Set ISCOs to collect new samples
- Pulled SUNA out for Nolan to put in at Woodford

Upstream St. Cloud:

- Drift check at 9:15am
- Sonde was swapped with calibrated sonde at 9:30am

Field Notes 3/20/2019

Floodwall Station:

- Drift check at 9:15am
- Sonde was swapped with calibrated sonde at 10am

Field Notes 4/15/2019

Floodwall Station:

- SUNA reference spectrum was updates
- YSI was collected 9:45am, calibrated at Marshall, and then redeployed at 2:30pm

Upstream St. Cloud:

- YSI was collected at 9am, calibrated at Marshall, and then redeployed at 2pm

Field Notes 5/10/2019

Floodwall Station:

- Collected ISCO samples
- Set ISCOs to collect new samples
- SUNA reference spectrum was updates
- YSI was collected at 11:45, calibrated at Marshall, and then redeployed at 4pm

Upstream St. Cloud:

- YSI was collected at 10:45am, calibrated at Marshall, and then redeployed at 4:30pm

Field Notes 6/17/2019

Floodwall Station:

- Collected ISCO samples
- Set ISCOs to collect new samples: starting 6/17 at 11am on 1 hour intervals
- Drift check at 3pm
- Probes were switched with calibrated one
- Sonde redeployed at 3:30pm

Field Notes 6/27/2019

Floodwall Station:

- Collected ISCO samples
- Set ISCOs to collect new samples: ISCO B set from 1am 7/3 on 2 hour intervals, ISCO A set for 10am 6/27 on 1 hour intervals
- SUNA reference spectrum was updates

Upstream St. Cloud:

- Drift check at 10:45am
- Probes were switched with calibrated one
- Sonde redeployed at 11:30 am

Field Notes 7/3/2019

Floodwall Station:

- Austin retrieved the sonde at 12:15pm and redeployed at 6:30pm

Field Notes 7/12/2019

Floodwall Station:

- Collected ISCO samples
- Set ISCOs to collect new samples: ISCO B set from 12pm 7/15 on 2 hour intervals, ISCO A set immediately set on 2 hour intervals

Field Notes 7/26/2019

Floodwall Station:

- Collected ISCO samples
- Set ISCOs to collect new samples: ISCO B set from 12pm 8/4 on 4 hour intervals, ISCO A set for 12pm on 7/30 on 2 hour intervals
- Water depth: 21.5in
- SUNA reference spectrum was updates
- New YSI was deployed

Upstream St. Cloud:

- Drift check at 11:15am
- Probes were switched with calibrated one
- Sonde redeployed at 11:45 am
- Water depth: 14.4in

Field Notes 8/2/2019

Floodwall Station:

- Drift check at 10am
- Probes were switched with calibrated one
- Sonde redeployed at 10:30 am

Field Notes 8/15/2019

Floodwall Station:

- Collected ISCO samples
- Set ISCOs to collect new samples: ISCO B set from 1pm 8/22 on 7 hour intervals, ISCO A set for 1pm on 8/15 on 7 hour intervals
- SUNA reference spectrum was updates

Field Notes 8/22/2019

Upstream St. Cloud:

- YSI was collected at 10am, calibrated at Marshall, and then redeployed at 2:30pm

Field Notes 9/13/2019

Floodwall Station:

- SUNA reference spectrum was updates
- New YSI was deployed

Upstream St. Cloud:

- New YSI was deployed at 11:30am
- Water depth: 14.5in

Field Notes 10/11/2019

Floodwall Station:

- SUNA reference spectrum was updates
- Drift check at 9:30am
- Probes were switched with calibrated one
- Sonde redeployed at 10am
- Grab sample taken at 9:30am

Upstream St. Cloud:

- Drift check at 10:15am
- Probes were switched with calibrated one
- Sonde redeployed at 10:45 am
- Water depth: 15in
- Upstream grab sample taken at 10:00am

Field Notes 11/12/2019

Upstream St. Cloud:

- Austin retrieved the sonde at 9am and redeployed at 3pm

Upstream St. Cloud:

- Austin retrieved the sonde at 10:30am and redeployed at 3:30pm

Field Notes 12/12/2019

Upstream St. Cloud:

- Austin retrieved the sonde at 12pm and redeployed at 4:45pm

Field Notes 1/10/2020

Floodwall Station:

- Austin retrieved the sonde at 10:12am and redeployed at 3pm

Field Notes 1/12/2020

Upstream St. Cloud:

- Austin retrieved the sonde at 10:30am and redeployed at 2:30pm

APPENDIX B. Site Pictures

Cyanobacteria at the Floodwall Station on September 13th, 2019 prior to the HAB on the Ohio River that began on September 27th, 2019.

Fourpole Creek on June 17th, 2019 right after Event 14

Sediment deposition on a tree near the outlet on July 26th, 2019 after Event 15

Sediment deposition on floodplain vegetation

Sediment deposition at the downstream monitoring station on May 15th, 2020 after an event

Floodplain and stream channel in Reach 2

Floodplain and stream channel in Reach 3

APPENDIX C. Laboratory Procedures

The following is adapted from EPA Method 160.2, ASTM Method D3977-97, and the LISST-Portable User's Guide Version 3.11.

Priming Filters

1. Place GF/C filters onto the filter apparatus. Turn on the vacuum and rinse each filter with approximately 40-50ml of deionized water. Let all the water pass through the filter before turning the vacuum off.
2.
3. Remove each filter using clean tweezers and place onto an individual labeled aluminum drying dish.
4. Place all the aluminum dishes into the drying oven at 105℃ until the filters reach a constant weight (approximately 2 hours).
    a. To determine if constant weight has been achieved, take several filters out of the oven (1 out of every 10), weigh them, and then place them back in the oven for 15-30 more minutes, remove and weigh again. If the weight is less than 0.5mg from the previous weight, constant weight has been achieved.
5. Remove the aluminum dishes from the drying oven and pre-combust the filters in the muffle furnace at 550℃ for approximately 30 minutes. Shouldn't the weight be taken at this point because you may have combusted some organic matter, right?
6. Remove the aluminum dishes and place them into a desiccator until use at a later time or for at least 10 minutes before immediate use.

LISST Particle Size Analysis

1. Acquire a grab sample from the refrigerator and gently shake the sample until all the sediment becomes suspended in water.
2. Immediately pour approximately 50 mL into a clean 150 mL plastic Nalgene bottle. Label the plastic bottle with the sample date, time, and number. Set the bottle aside and return the remainder of the sample to the refrigerator.
3. Turn the LISST on and tap the Measure button from the Main Menu.
4. Step 1: Rinse Chamber will appear on the display window. Ensure the drain lever is in the closed position and remove the lid from the mixing chamber. Fill up the chamber approximately halfway with deionized water. Place the lid back on the mixing chamber. Adjust the mixer speed to 150% using the slider on the display window. Let the water circulate for about 5 seconds and then open the drain lever.

Allow all the water to drain completely out of the chamber (~5-10 seconds) and then return the drain level to the closed position. On the display screen, slide the mixer to 0% to turn it off. It may be necessary to repeat this process if the mixing chamber is still dirty.

5. Once the mixer is clean, tap the green Next checkmark button on the display and Step 2: Get Background will appear on the display window. Fill the mixing chamber with deionized water. Press the Update button on the display. The instrument will take a background reading and display a graph on the screen. The blue bars are the current values and the red line is the factory values. If the blue bars are higher than the red line, the transmission value reported next to the graph will be below 0.95 and chamber will need to be rinsed again. Press the Back button and repeat previous step. Once the background transmission is 0.95 or above press the green Next checkmark to proceed to Step 3a.

6. Step 3a: Add Sample will appear on the display screen. Gently shake the 50mL sample re-suspending the sediment particles in the water. Make sure the drain lever is in the closed position and pour the entire sample into the mixing chamber. Enter sample information such as date, time, and sample number into the grey Field Note box at the bottom of the display screen. Press the Mixer On button turning on the mixer and the press the green Next button. If the mixer is not turned on, a warning will appear staying that the "Mixer is not turned on!" and asks "Do you want to turn it on?" Press the green Yes checkmark and the instrument will begin to take a measurement.

7. Step 4: Acquiring Average will appear on the display screen with the loading bar that will last about 20 seconds. Leave the mixer on and do not open the chamber at this time.

8. Once the measurement is complete, Step 5: Computing Size Distribution will appear on the display screen. It will take about 45 seconds to compute the size distribution from the averaged data. During this time the mixer can be turned off and the mixing chamber can be drained.

9. After the computations are complete, the results will be shown on four tabs labeled Vol Dist, Cum Dist, Table, and Stats. The data can be reviewed on the screen at this time and will automatically save on the instrument. Press the green Return checkmark to return to the Step 1 screen and proceed with the next sample.

<u>Turbidity Measurement</u>

1. Obtain a YSI EXO2 sonde with a calibrated turbidity and fDOM probe and clean the probes using phosphate free soap. Make sure all the sediment is removed from the probes and rinse thoroughly with deionized water.

2. Acquire a grab sample from the refrigerator and gently shake the sample until all the sediment becomes suspended in water.
3. Pour approximately 650 mL into a clean YSI calibration cup and return the remainder of the sample to the refrigerator. It is imperative that the calibration cup is cleaned and free of debris/organic matter prior to analysis.
4. Screw the calibration cup onto the sonde tightly.
5. Open up the KOR software and scan for the sonde. Once the scan is complete, select the sonde to pair the devices.
6. Click the green Deploy arrow and load the Lab Turbidity Template. Deploy the sonde with a 30 second delay.
7. Shake the sonde (with calibration cup attached) for 30 seconds re-suspending any sediment and creating a homogenous mixture.
8. After the 30 seconds of mixing, immediately set the sonde upright and it will begin taking measurements every 5 seconds.
9. After about a minute the deployment can be ended by clicking the Stop Deployment button on the deployment tab within the KOR program.
10. Click the blue Data folder and then the transfer file button. Select the file where the data from the last deployment was saved. The file will begin to download. Once it is downloaded, click the export data button and an excel file will download and open on the computer. Save this file.
11. Unscrew the calibration cup from the YSI and pour about 50 mL into a clean 150 mL plastic Nalgene bottle. Label the plastic bottle with the sample date, time, and number. This sample will need to be run on the LISST to check for sediment particle breakdown. Pour the remainder of the contents in the cup back into the original bottle to be processed for TSS. Return the samples to the refrigerator.
12. Thoroughly clean the YSI probes and calibration cup with phosphate free soap. Ensure that no sediment is left in the cup or on the YSI probes and rinse with deionized water.
13. Once the cup and probes are clean, proceed to the next sample.

<u>Total Suspended Sediment and Particle Organic Matter Measurement</u>

1. Remove a primed filter from the desiccator and use a sharpie to label the aluminum dish with the sample number.
2. Weigh the aluminum dish with the filter and record the mass to an accuracy of 0.1 mg on the data sheet.

3. Setup the filtration apparatus, place filter into position using clean tweezers, and turn on the vacuum.
4. Run approximately 20-30mL of deionized water through the filter.
5. Acquire a grab sample from the refrigerator and gently shake the sample until all the sediment becomes suspended in water.
6. Pour the sample into the 1000 mL graduated cylinder. Record the volume of the sample on the data sheet.
7. Pour sample slowly into the filtration apparatus.
8. Once all the sample has passed through the filter, remove the filter using the tweezers. Place filter back into its aluminum dish.
7. Place the aluminum dish into the drying oven at 105℃ until the filters reach a constant weight (approximately 2 hours).
9. Once sample has reached constant weight remove the aluminum dish from the oven and place in the desiccator to cool off (which avoids moisture adsorption). Then, reweigh the dish and filter. Record this mass as on the data sheet.
10. Place the aluminum dish into the muffle furnace at 550℃ until the filters reach a constant weight (approximately 30 minutes).
11. Once sample has reached constant weight remove the aluminum dish and reweigh the dish and filter. Record this mass as on the data sheet.
12. Repeat this process for each sample.

APPENDIX D. Data QA/QC MATLAB Script

```
%Ciara Pickering
%BAE Graduate Research Assistant
%Upstream St. Cloud and Floodwall Station YSI Datasets
%August 2018 to December 2019


clear;
clc;
close all;

%Import Data
data=xlsread('YSI_1-YSI_12.xlsx','Sheet1','I4:X60146');

% Allocate imported array to column variable names
ODO_sat = data(:,1);
ODO_mgL = data(:,2);
fDOM_RFU = data(:,3);
fDOM_QSU = data(:,4);
Temp = data(:,5);
Cond = data(:,6);
SpCond = data(:,7);
Sal = data(:,8);
nLF_Cond= data(:,9);
TDS_mgL = data(:,10);
Turbidity = data(:,11);
pH = data(:,12);
pH_mV = data(:,13);
Press = data(:,14);
Depth_m = data(:,15);
Ohio_Stage = data(:,16);

%Change any depth reading to below 0.75 ft to NaN
for i=1:length(Ohio_Stage)
    FourpoleCreek_Stage(i)=Ohio_Stage(i)-24.75;
    if FourpoleCreek_Stage(i)<0.75
        FourpoleCreek_Stage(i)=-99999;
    end
end

FourpoleCreek_Stage=FourpoleCreek_Stage';

% Turbidity (FNU)
for i=1:length(Turbidity)
    if Turbidity(i)<10
        Turbidity(i)=-99999; %return error
    elseif Turbidity(i)>5000
```

```
        Turbidity(i)=-99999; %return error
    end
end

% Temp (degC)
for i=1:length(Temp)
    if Temp(i)<10
        Temp(i)=-99999; %return error
    elseif Temp(i)>5000
        Temp(i)=-99999; %return error
    end
end

% Conductivity
for i=1:length(Cond)
    if Cond(i)<10
        Cond(i)=-99999; %return error
    elseif Cond(i)>5000
        Cond(i)=-99999; %return error
    end
end

% Specific Conductivity
for i=1:length(SpCond)
    if SpCond(i)<10
        SpCond(i)=-99999; %return error
    elseif SpCond(i)>5000
        SpCond(i)=-99999; %return error
    end
end

% ODO percent saturated
for i=1:length(ODO_sat)
    if ODO_sat(i)<0
        ODO_sat(i)=-99999; %return error
    elseif ODO_sat(i)>100
        ODO_sat(i)=-99999; %return error
    end
end

% ODO mg/L
for i=1:length(ODO_mgL)
    if ODO_mgL(i)<2
        ODO_mgL(i)=-99999; %return error
    elseif ODO_mgL(i)>14
        ODO_mgL(i)=-99999; %return error
    end
```

```
end

% fDOM (RFU)
for i=1:length(fDOM_RFU)
    if fDOM_RFU(i)<0
        fDOM_RFU(i)=-99999; %return error
    elseif fDOM_RFU(i)>100
        fDOM_RFU(i)=-99999; %return error
    end
end

% pH
for i=1:length(pH)
    if pH(i)<4
        pH(i)=-99999; %return error
    elseif pH(i)>12
        pH(i)=-99999; %return error
    end
end

%Compile Data
Compiled_Data=[ODO_sat,ODO_mgL,fDOM_RFU,fDOM_QSU,Temp,Cond,
SpCond,Sal,nLF_Cond,TDS_mgL,Turbidity,pH,pH_mV,Press,Depth_
m,Ohio_Stage,FourpoleCreek_Stage];

%Export to Excel
T=table(Compiled_Data);
T(:,:);
filename='newtestdata.xlsx';
writetable(T,filename,'Sheet',1,'Range','I1:Y60143')
```

APPENDIX E. Upstream and Downstream Data Driven Sediment Flux Model MATLAB Script

```
%Ciara Pickering
%BAE Graduate Research Assistant
%Upstream St. Cloud Sediment Flux Model
%2019 simulation and event simulation

clear;
clc;
close all;

%Constants
G=32.2;                 %ft/s^2   Gravity
ks=0.01;                %ft   Nikuradse's Sand Roughness
R=1.65;                 %Ratio of fluid to particle densities
g=9.8;                  %m/s^2   acceleration of gravity
D=10*10^(-6);           %m   average particle diameter
c1=18;                  %dimensionless constant
c2=1;                   %dimensionless constant for natural
grains
v=1.235*10^(-6);        %m/s^2@12C kinematic viscosity of
water
K=0.4;                  %von Karmen's constant
a=0.000468;             %the depth at which sediment begins
z=7.5/12;               %depth where TSS sample is taken

%Channel Parameters
W=28;                   %ft   Width
S0=0.004667;            %ft/ft   Bed Slope
n=0.015;                %estimate of mannings roughness for
concrete channel

%Call Depth Data
Data= xlsread("Upstream Data","Sheet1",'A:C');
USC_depth= Data(:,2);
m=size(USC_depth,1);
for i=1:m
    USC_depth(i)=USC_depth(i)+1;
end

%Call Hurricane Creek Flow Data
Fourpole_Q=Data(:,3);

%Flow Plot
figure(1);
plot(Fourpole_Q)
```

```
xlabel('Time');
ylabel('Flow Rate (CFS)');

hold on

%Velocity and Flow Rate
A=W*USC_depth;                                          %ft^2
Area
WP=W+4*USC_depth;                                       %ft
Wetted Perimeter
HR=A./WP;                                               %ft
Hydraulic Radius
Sf=Fourpole_Q.*abs(Fourpole_Q).*n.^2./(2.208.*HR.^(4/3).*A.
^2);
Ustar=(G.*HR.*Sf).^(1/2);                               %ft/s
Shear Velocity

%Velocity Profile
x=50;
%adjustable step size
for i=1:m
    for n=1:x+1
    Di(i)=USC_depth(i)./x;
    Z(n,i)=abs(USC_depth(i)-(n-1)*Di(i));
    U(1,:)=0;
    Z(x+1,:)=0;
    U(n,i)=Ustar(i).*(8.5+2.5.*log(Z(n,i)./ks));  %Chang
Equation 3.24
    U(x+1,:)=0;
    end
end

%Example Velocity Profile Plot
D1=Z(:,10);
V1=U(:,10);
figure(2);
plot(V1,D1)
xlabel('Velocity (ft/s)');
ylabel('Depth (ft)');

%Integration of the Velocity Profile to Find Q
for i=1:m
  flow(i)=trapz(U(:,i),Z(:,i));
  Q(i)=flow(i)*28;
end

figure(1);
```

```
plot(Q)
legend('Area Weighted Flow Rate','Modeled Flow Rate');

%Call Turbidity Data
USC_turbidity=Data(:,1);

%Particle Size as a Function of Turbidity
for i=1:m
    D_m(i)=209.78*(USC_turbidity(i)).^(-0.493);
%Trendline for D50 and Turbidity
    D(i)=D_m(i)*10^(-6);
end

%Average Settling Velocity
for i=1:m
    ws_m(i)=(R*g*D(i)^2)/(c1*v+(0.75*c2*R*g*D(i)^3)^0.5);
%m/s Ferguson & Church Equation 1
    ws(i)=ws_m(i)*3.28;
%m/s to ft/s
end

%Z*
for i=1:m
    Zstar(i)=ws(i)/(K.*Ustar(i));
end

%TSS from Turbidity
for i=1:m
    TSS(i)=1.2501.*USC_turbidity(i).^(0.9465);
end

%Rouse Concentration Profile
for i=1:m
    if Fourpole_Q(i)<30
        for j=2:50
            C(j,i)=TSS(i);
        end
        for n=1:x+1
        C(x+1,:)=0;
        Cft(n,i)=C(n,i)/0.0353147;
        end
    else
        for n=1:x+1
            Ca(i)=TSS(i)/((USC_depth(i)-
z)/z*a/(USC_depth(i)-a))^(Zstar(i));
            C(n,i) = Ca(i)*((USC_depth(i)-
Z(n,i))/Z(n,i)*a/(USC_depth(i)-a))^(Zstar(i));
```

```
            C(x+1,:)=0;
            Cft(n,i)=C(n,i)/0.0353147;
%mg/L to mg/ft^3
        end
    end
end

%Example Concentration Profile Plot
D1=Z(:,25);
Con1=Cft(:,25);
figure(3);
plot(Con1,D1)
xlabel('Concentration (mg/ft^3)');
ylabel('Depth (ft)');

%Einstein's Discharge of Suspended Sediment
for i=1:m
    for n=1:x+1
        q(n,i)=Cft(n,i)*U(n,i);
        q(x+1,:)=0;
    end
end

%Example Sediment Discharge Plot
D1=Z(:,25);
qss1=q(:,25);
figure(4);
plot(qss1,D1)

%Integration

for i=1:m
  Int(i)=trapz(q(:,i),Z(:,i));                    %mg/s per
unit width
  Qss(i)=Int(i)*28;                               %mg/s
  Massflux(i)=Qss(i)/Q(i);                        %mg
  Sed(i)=Int(i)*900;                              %mg per
unit witdth
end

for i=1:m
    POM(i)=0.0955*Sed(i);
end
sed=Sed';

%Total Suspended Sediment Flux
```

```
qss=sum(Sed);                                   %mg per
unit width
Qss_mg=qss*W;                                   %mg
Qss_g=Qss_mg/1000;                              %g
Qss_kg=Qss_g/1000                               %kg

POMT=sum(POM);
POM_mg=POMT*W;
POM_kg=POM_mg/10^6

LowC_kg=POM_kg*0.28
HighC_kg=POM_kg*0.5

LowN_kg=LowC_kg/9.8
HighN_kg=HighC_kg/9.8
```

```
%Ciara Pickering
%BAE Graduate Research Assistant
%Downstream Floodwall Station Sediment Flux Model
%2019 simulation and event simulation

clear;
clc;
close all;

%Constants
G=32.2;                 %Gravity
ks=0.01;                %Nikuradse's Sand Roughness
R=1.65;                 %Ratio of fluid to particle
densities
g=9.8;                  %m/s^2   acceleration of gravity
D=10*10^(-6);           %m   average particle diameter
c1=18;                  %dimensionless constant
c2=1;                   %dimensionless constant for natural
grains
v=1.235*10^(-6);        %m/s^2@12C kinematic viscosity of
water
K=0.4;                  %von Karmen's constant
a=0.000468;             %the depth at which sediment begins
z=7.5/12;               %depth where TSS sample is taken

%Channel Parameters
W=28;                   %Width
S0=0.004667;            %Bed Slope
n=0.015;                %Estimate of mannings roughness for
concrete channel

%Call Depth Data
Data= xlsread("All Downstream Data","Sheet1",'B2:E35041');
FWS_depth= Data(:,4);
m=size(FWS_depth,1);

%Call HEC-RAS Flow Data
FWS_Q=Data(:,1);

%Seperate Positive and Negative Flow Rates
for i=1:m
if FWS_Q(i)>0
    Positive_Flow(i)=FWS_Q(i);
elseif FWS_Q(i)<0
    Negative_Flow(i)=FWS_Q(i);
    ABS_Negative_Flow(i)=abs(Negative_Flow(i));
elseif FWS_Q(i)==0
```

```
    Positive_Flow(i)=FWS_Q(i);
end
Negative_Flow(35033:35040)=0;
ABS_Negative_Flow(35033:35040)=0;
end

for i=1:m
    if Positive_Flow(i)>0
        Pos_Depth(i)=FWS_depth(i);
    elseif Positive_Flow(i)==0
        Pos_Depth(i)=0;
    end
end

for i=1:m
    if ABS_Negative_Flow(i)>0
        Neg_Depth(i)=FWS_depth(i);
    elseif ABS_Negative_Flow(i)==0
        Neg_Depth(i)=0;
    end
end

%Transpose Matrix
Positive_Flow=Positive_Flow';
Negative_Flow=Negative_Flow';
Neg_Depth=Neg_Depth';
Pos_Depth=Pos_Depth';

%Channel Geometry for Positive and Negative Flow
A=W*FWS_depth;                                          %Area
WP=W+4*FWS_depth;                                       %Wetted
Perimeter
HR=A./WP;
%Hydraulic Radius
Sf_Pos=Positive_Flow.*abs(Positive_Flow).*n.^2./(2.208.*HR.
^(4/3).*A.^2);
Sf_Neg=Negative_Flow.*abs(Negative_Flow).*n.^2./(2.208.*HR.
^(4/3).*A.^2);
Sf_Neg_ABS=abs(Sf_Neg);
Sf=Sf_Pos+Sf_Neg;
Ustar_Pos_Adj=(G.*HR.*Sf_Pos).^(1/2);
%Shear Velocity
Ustar_Neg=(G.*HR.*Sf_Neg_ABS).^(1/2);
%Shear Velocity
Ustar=Ustar_Pos_Adj+Ustar_Neg;

%Velocity Profile for Positive Flow
```

```
x=50;
%adjustable step size
for i=1:m
    for n=1:x+1
    Di_Pos(i)=FWS_depth(i)./x;
    Z_Pos(n,i)=abs(FWS_depth(i)-(n-1)*Di_Pos(i));
    U_Pos(1,:)=0;
    Z_Pos(x+1,:)=0;

U_Pos(n,i)=Ustar_Pos_Adj(i).*(8.5+2.5.*log(Z_Pos(n,i)./ks))
;  %Chang Equation 3.24
    U_Pos(x+1,:)=0;
    end
end

%Velocity Profile for Negative Flow
x=50;
%adjustable step size
for i=1:m
    for n=1:x+1
    Di_Neg(i)=FWS_depth(i)./x;
    Z_Neg(n,i)=abs(FWS_depth(i)-(n-1)*Di_Neg(i));
    U_Neg(1,:)=0;
    Z_Neg(x+1,:)=0;

U_Neg(n,i)=Ustar_Neg(i).*(8.5+2.5.*log(Z_Neg(n,i)./ks));
%Chang Equation 3.24
    U_Neg(x+1,:)=0;
    end
end

%Integration of the Velocity Profile to Find Q for Positive
for i=1:m
  flow_Pos(i)=trapz(U_Pos(:,i),Z_Pos(:,i));
%mg/s per unit width
  Q_Pos(i)=flow_Pos(i)*28;                                %mg
per unit witdth
end

%Integration of the Velocity Profile to Find Q for Negative
for i=1:m
  flow_Neg(i)=trapz(U_Neg(:,i),Z_Neg(:,i));
%mg/s per unit width
  Q_Neg_ABS(i)=flow_Neg(i)*28;
%mg per unit witdth
  Q_Neg(i)=Q_Neg_ABS(i)*-1;
end
```

```
Q_Pos=Q_Pos';
Q_Neg=Q_Neg';
Q_Neg_ABS=Q_Neg_ABS';

%Call Turbidity Data
FWS_turbidity=Data(:,2);

%Combine Flow and Turbidity Matrix
Combo_Data_Pos=[Q_Pos,FWS_turbidity,Ustar,FWS_depth];
Combo_Data_Neg=[Q_Neg_ABS,FWS_turbidity,Ustar,FWS_depth];

%Remove Zeros and Create New Index
Combo_Data_Pos_Adj=Combo_Data_Pos(all(Combo_Data_Pos,2),:);
Combo_Data_Neg_Adj=Combo_Data_Neg(all(Combo_Data_Neg,2),:);
b=size(Combo_Data_Pos_Adj,1);
y=size(Combo_Data_Neg_Adj,1);

%Velocity Profile for ONLY Positive Flow
Depth_Pos=Combo_Data_Pos_Adj(:,4);
Ustar_Pos_Adj=Combo_Data_Pos_Adj(:,3);
x=50;                                %adjustable step size
for i=1:b
    for n=1:x+1
    di_Pos(i)=Depth_Pos(i)./x;
    z_Pos(n,i)=abs(Depth_Pos(i)-(n-1)*di_Pos(i));
    u_Pos(1,:)=0;
    z_Pos(x+1,:)=0;

u_Pos(n,i)=Ustar_Pos_Adj(i).*(8.5+2.5.*log(z_Pos(n,i)./ks))
;  %Chang Equation 3.24
    u_Pos(x+1,:)=0;
    end
end

%Velocity Profile for ONLY Negative Flow
Depth_Neg=Combo_Data_Neg_Adj(:,4);
Ustar_Neg_Adj=Combo_Data_Neg_Adj(:,3);
x=50;
%adjustable step size
for i=1:y
    for n=1:x+1
    di_Neg(i)=Depth_Neg(i)./x;
    z_Neg(n,i)=abs(Depth_Neg(i)-(n-1)*di_Neg(i));
    u_Neg(1,:)=0;
    z_Neg(x+1,:)=0;
```

```
u_Neg(n,i)=Ustar_Neg_Adj(i).*(8.5+2.5.*log(z_Neg(n,i)./ks))
;  %Chang Equation 3.24
    u_Neg(x+1,:)=0;
    end
end

%Particle Size as a Function of Turbidity for ONLY Positive
Flow
Turb_Pos=Combo_Data_Pos_Adj(:,2);
for i=1:b
    D_m_pos(i)=209.78*(Turb_Pos(i)).^(-0.493);
%Trendline for D50 and Turbidity
    D_pos(i)=D_m_pos(i)*10.^(-6);
end

%Average Settling Velocity for ONLY Positive Flow
for i=1:b

ws_m_pos(i)=(R*g*D_pos(i)^2)/(c1*v+(0.75*c2*R*g*D_pos(i)^3)
^0.5);   %m/s Ferguson & Church Equation 1
    ws_pos(i)=ws_m_pos(i)*3.28;
%m/s
end

%Particle Size as a Function of Turbidity for ONLY Negative
Flow
Turb_Neg=Combo_Data_Neg_Adj(:,2);
for i=1:y
    D_m_neg(i)=209.78*(Turb_Neg(i)).^(-0.493);
%Trendline for D50 and Turbidity
    D_neg(i)=D_m_neg(i)*10^(-6);
end

%Average Settling Velocity for ONLY Negative Flow
for i=1:y

ws_m_neg(i)=(R*g*D_neg(i)^2)/(c1*v+(0.75*c2*R*g*D_neg(i)^3)
^0.5);  %m/s Ferguson & Church Equation 1
    ws_neg(i)=ws_m_neg(i)*3.28;
%m/s
end

%Z* for Positive Flow
for i=1:b
    Zstar_Pos(i)=ws_pos(i)/(K.*Ustar_Pos_Adj(i));
end
```

```
%Z* for Negative Flow
for i=1:y
    Zstar_Neg(i)=ws_neg(i)/(K.*Ustar_Neg_Adj(i));
end

%TSS from Turbidity for Positive Flow
Turb_Pos=Combo_Data_Pos_Adj(:,2);
for i=1:b
    TSS_Pos(i)=1.2501.*Turb_Pos(i).^(0.9465);
end

%TSS from Turbidity for Negative Flow
Turb_Neg=Combo_Data_Neg_Adj(:,2);
for i=1:y
    TSS_Neg(i)=1.2501.*Turb_Neg(i).^(0.9465);
end

Qadj_Pos=Combo_Data_Pos_Adj(:,1);
Qadj_Neg=Combo_Data_Neg_Adj(:,1);

%Rouse Concentration Profile for Positive Flows
for i=1:b
    if Qadj_Pos(i)<30
        for j=2:50
            C_Pos(j,i)=TSS_Pos(i);
        end
        for n=1:x+1
            C_Pos(x+1,:)=0;
            C_Pos_ft(n,i)=C_Pos(n,i)/0.0353147;
        end
    else
        for n=1:x+1
            Ca_Pos(i)=TSS_Pos(i)/((Depth_Pos(i)-
z)/z*a/(Depth_Pos(i)-a))^(Zstar_Pos(i));
            C_Pos(n,i) = Ca_Pos(i)*((Depth_Pos(i)-
z_Pos(n,i))/z_Pos(n,i)*a/(Depth_Pos(i)-a))^(Zstar_Pos(i));
            C_Pos(x+1,:)=0;
            C_Pos_ft(n,i)=C_Pos(n,i)/0.0353147;
        end
    end
    avg_Pos_ft(i)=mean(C_Pos_ft(2:50,i));
    avg_Pos(i)=avg_Pos_ft(i)/28.31;
end

%Integration for Positive
for i=1:b
```

```
  Concen_Pos(i)=trapz(C_Pos_ft(:,i),Z_Pos(:,i));
%mg/s per unit width ft
end

%Rouse Concentration Profile for Negative Flows
for i=1:y
    if Qadj_Neg(i)>-30
        for j=2:50
            C_Neg(j,i)=TSS_Neg(i);
        end
        for n=1:x+1
            C_Neg(x+1,:)=0;
            C_Neg_ft(n,i)=C_Neg(n,i)/0.0353147;
        end
    else
        for n=1:x+1
            Ca_Neg(i)=TSS_Neg(i)/((Depth_Neg(i)-
z)/z*a/(Depth_Neg(i)-a))^(Zstar_Neg(i));
            C_Neg(n,i) = Ca_Neg(i)*((Depth_Neg(i)-
z_Neg(n,i))/z_Neg(n,i)*a/(Depth_Neg(i)-a))^(Zstar_Neg(i));
            C_Neg(x+1,:)=0;
            C_Neg_ft(n,i)=C_Neg(n,i)/0.0353147;
        end
    end
    avg_Neg_ft(i)=mean(C_Neg_ft(2:50,i));
    avg_Neg(i)=avg_Neg_ft(i)/28.31;
end

%Integration for Negative
for i=1:y
  Concen_Neg(i)=trapz(C_Neg_ft(:,i),Z_Neg(:,i));  %mg/s per
unit width
end

%Einstein's Discharge of Suspended Sediment for Positive
Flows
for i=1:b
    for n=1:x+1
        q(n,i)=C_Pos_ft(n,i)*u_Pos(n,i);
        q(x+1,:)=0;
    end
end

%Integration for Positive
for i=1:b
  Int(i)=trapz(q(:,i),z_Pos(:,i));              %mg/s per
unit width
```

```
  QssP(i)=Int(i)*28;
  Sed(i)=Int(i)*900;                                  %mg per
unit witdth
  New(i)=Int(i)*28/(10^6);
end

%Total Suspended Sediment Flux for Positive
qss1=sum(Sed);                                        %mg per
unit width
Qss1_mg=qss1*W;                                       %mg
Qss1_g=Qss1_mg/1000;                                  %g
Qss1_kg=Qss1_g/1000;                                  %kg

%Einstein's Discharge of Suspended Sediment for Negative
Flows
for i=1:y
    for n=1:x+1
        q2(n,i)=C_Neg_ft(n,i)*u_Neg(n,i);
        q2(x+1,:)=0;
    end
end

%Integration for Negative Flows
for i=1:y
  Int2(i)=trapz(q2(:,i),z_Neg(:,i));                  %mg/s
per unit width
  QssN(i)=Int2(i)*28;
  Sed2(i)=Int2(i)*900;                                %mg per
unit witdth
  New2(i)=Int2(i)*28/(10^6);
end

% Total Suspended Sediment Flux for Negative Flows
qss2=sum(Sed2);                                        %mg per
unit width
Qss2_mg=qss2*W;                                       %mg
Qss2_g=Qss2_mg/1000;                                  %g
Qss2_kg=Qss2_g/1000;                                  %kg

for i=1:b
    if FWS_turbidity(i)<10
        POM(i)=0.2625*Sed(i);
    elseif FWS_turbidity(i)>10 && FWS_turbidity(i)<100
        POM(i)=0.1581*Sed(i);
    elseif FWS_turbidity(i)>100 && FWS_turbidity(i)<400
        POM(i)=0.1116*Sed(i);
    elseif FWS_turbidity(i)>400
```

```
        POM(i)=0.0955*Sed(i);
    end
end

for i=1:y
    if FWS_turbidity(i)<10
        POM2(i)=0.2625*Sed2(i);
    elseif FWS_turbidity(i)>10 && FWS_turbidity(i)<100
        POM2(i)=0.1581*Sed2(i);
    elseif FWS_turbidity(i)>100 && FWS_turbidity(i)<400
        POM2(i)=0.1116*Sed2(i);
    elseif FWS_turbidity(i)>400
        POM2(i)=0.0955*Sed2(i);
    end
end

%POM, PC, and PN for flux out
POMT=sum(POM);
POM_mg=POMT*W;
POM_kg=POM_mg/10^6;

LowC_kg=POM_kg*0.28;
HighC_kg=POM_kg*0.5;

LowN_kg=LowC_kg/9.8
HighN_kg=HighC_kg/9.8

%POM, PC, and PN for flux in
POMT2=sum(POM2);
POM_mg2=POMT2*W;
POM_kg2=POM_mg2/10^6;

LowC_kg2=POM_kg2*0.28;
HighC_kg2=POM_kg2*0.5;

LowN_kg2=LowC_kg2/9.8;
HighN_kg2=HighC_kg2/9.8;
```

APPENDIX F. Sediment Transport Numerical Model MATLAB Script

```
%Ciara Pickering
%BAE Graduate Research Assistant
%Fourpole Creek Wetland Sediment Transport Model
%2019 Simulation

clear;
clc;
close all;

% %Call data
A=xlsread("Area Data 01012019-
12312019","Sheet1",'B2:AF35041');
n=xlsread("Mannings n LRC Data 01012019-
12312019","Sheet1",'B2:AF105121');
nT=xlsread("Mannings n Data 01012019-
12312019","Sheet1",'B2:AF35041');
R=xlsread("Hydraulic Radius Data 01012019-
12312019","Sheet1",'B2:AF35041');
Q=xlsread("Total Flow Rate Data 01012019-
12312019","Test",'B1:AF35040');
Geo_ft=xlsread("Reach Geometry Data","Reach
Averages",'B2:G6');
Geo_m=xlsread("Reach Geometry Data","Reach
Averages",'I2:N6');
Turbidity=xlsread("Turbidity Data 01012019-
12312019","Sheet1",'B2:C35041');

%Global parameters
numsteps=size(A,1);
numsteps3=size(n,1);
numreaches=5;
numxs=31;
deltat=900;     %15 minute timestep in seconds
rho_w=997;      %density of water kg/m3
rho_s=2700;     %density of soil kg/m3
g=9.81;         %m/s^2
K=0.4;

%Source erosion parameters
b_s=1;
b_b=1;
b_f=1;

%Reach parameters
for i=1:numreaches+1
```

```
    w(1:numsteps,i)= Geo_ft(1,i);
    h(1:numsteps,i)=Geo_ft(2,i);
    L(1:numsteps,i)=Geo_ft(3,i);
    sL(1:numsteps,i)=Geo_ft(4,i);
    fL(1:numsteps,i)=Geo_ft(5,i);
end

%Average nT for each Reach
nT_R1=nT(:,1:6);
for i=1:numsteps
   AnT_R1(i)=mean(nT_R1(i,:));
end
AnT_R1=AnT_R1';

nT_R2=nT(:,7:12);
for i=100:numsteps
    AnT_R2(i)=mean(nT_R2(i,:));
end
AnT_R2=AnT_R2';

nT_R3=nT(:,13:18);
for i=100:numsteps
    AnT_R3(i)=mean(nT_R3(i,:));
end
AnT_R3=AnT_R3';

nT_R4=nT(:,19:24);
for i=100:numsteps
    AnT_R4(i)=mean(nT_R4(i,:));
end
AnT_R4=AnT_R4';

nT_R5=nT(:,25:30);
for i=100:numsteps
    AnT_R5(i)=mean(nT_R5(i,:));
end
AnT_R5=AnT_R5';

AnT=[AnT_R1,AnT_R2,AnT_R3,AnT_R4,AnT_R5,nT(:,31)];

%Seperate Mannings n of LOB, ROB, and Channel
nC=n(1,:);
nL=n(2,:);
nR=n(3,:);

for i=1:numsteps
    nC(i,:)=n(3*(i-1)+1,:);
```

```
    nL(i,:)=n(3*(i-1)+2,:);
    nR(i,:)=n(3*(i-1)+3,:);
end

%Average nF for each Reach
n_R1=nC(:,1:6);
for i=1:numsteps
   An_R1(i)=mean(n_R1(i,:));
end
An_R1=An_R1';

n_R2=nC(:,7:12);
for i=100:numsteps
    An_R2(i)=mean(n_R2(i,:));
end
An_R2=An_R2';

n_R3=nC(:,13:18);
for i=100:numsteps
    An_R3(i)=mean(n_R3(i,:));
end
An_R3=An_R3';

n_R4=nC(:,19:24);
for i=100:numsteps
    An_R4(i)=mean(n_R4(i,:));
end
An_R4=An_R4';

n_R5=nC(:,25:30);
for i=100:numsteps
    An_R5(i)=mean(n_R5(i,:));
end
An_R5=An_R5';

AnS=[An_R1,An_R2,An_R3,An_R4,An_R5,nC(:,31)];

%Average Mannings n for Floodplain
for i=100:numsteps
    for j=1:numxs
        if nR(i,j)==0 && nL(i,j)==0
            nF(i,j)=0;
        elseif nR(i,j)==0 && nL(i,j)>0
            nF(i,j)=nL(i,j);
        elseif nR(i,j)>0 && nL(i,j)==0
            nF(i,j)=nR(i,j);
        elseif nR(i,j)>0 && nL(i,j)>0
```

```
            nF(i,j)=(nR(i,j)+nL(i,j))/2;
        end
    end
end

%Average nF for each Reach
nF_R1=nF(:,1:6);
for i=100:numsteps
   AnF_R1(i)=mean(nF_R1(i,:));
end
AnF_R1=AnF_R1';

nF_R2=nF(:,7:12);
for i=100:numsteps
    AnF_R2(i)=mean(nF_R2(i,:));
end
AnF_R2=AnF_R2';

nF_R3=nF(:,13:18);
for i=100:numsteps
    AnF_R3(i)=mean(nF_R3(i,:));
end
AnF_R3=AnF_R3';

nF_R4=nF(:,19:24);
for i=100:numsteps
    AnF_R4(i)=mean(nF_R4(i,:));
end
AnF_R4=AnF_R4';

nF_R5=nF(:,25:30);
for i=100:numsteps
    AnF_R5(i)=mean(nF_R5(i,:));
end
AnF_R5=AnF_R5';

AnF=[AnF_R1,AnF_R2,AnF_R3,AnF_R4,AnF_R5,nF(:,31)];

%Seperate Positive and Negative Flow Rates
for i=100:numsteps
    for j=1:numxs
        if Q(i,j)>0
            Q_P(i,j)=Q(i,j);
        elseif Q(i,j)<0
            Q_N(i,j)=Q(i,j);
            Q_AN(i,j)=abs(Q_N(i,j));
        elseif Q(i,j)==0
```

```
            Q_P(i,j)=Q(i,j);
        end
    end
   Q_AN(35033:35040,:)=0;
   Q_N(35033:35040,:)=0;
end

%Convert Flowrate from cfs to cms
for i=100:numsteps
    for j=1:numxs
        Q_m(i,j)=Q(i,j)*0.028316847;
    end
end

%Reach Boundary Flow Rates
AQ(:,1)=abs(Q_m(:,1));
AQ(:,2)=abs(Q_m(:,7));
AQ(:,3)=abs(Q_m(:,13));
AQ(:,4)=abs(Q_m(:,19));
AQ(:,5)=abs(Q_m(:,25));
AQ(:,6)=abs(Q_m(:,31));

%Calculate Friction Slope
for i=100:numsteps
    for j=1:numxs

Sf_P(i,j)=((Q_P(i,j)*nT(i,j))/(1.49*A(i,j)*(R(i,j)^(2/3))))
^2;

Sf_AN(i,j)=((Q_AN(i,j)*nT(i,j))/(1.49*A(i,j)*(R(i,j)^(2/3))
))^2;    %Sf_AN is the absolute value of the negative
friction slope
        Sf_N(i,j)=(Sf_AN(i,j)*-1);
    end
end

%Combine Positive and Negative Friction Slopes
for i=100:numsteps
    for j=1:numxs
        if Sf_P(i,j)>0
            Sf(i,j)=Sf_P(i,j);
        else
            Sf(i,j)=Sf_N(i,j);
        end
    end
end
```

```
%Reach Boundary Friction Slopes
ASf(:,1)=abs(Sf(:,1));
ASf(:,2)=abs(Sf(:,7));
ASf(:,3)=abs(Sf(:,13));
ASf(:,4)=abs(Sf(:,19));
ASf(:,5)=abs(Sf(:,25));
ASf(:,6)=abs(Sf(:,31));

for i=100:numsteps
    for j=1:numreaches
        AASf(i,j)=(ASf(i,j)+ASf(i,j+1))/2; %AASf=absolute
value of the average friction slope and ASf is the absolute
value of the friction slope
    end
end

%Channel Geometry in meters
for i=1:numreaches+1
    w_m(1,i)= Geo_m(1,i);
    h_m(1,i)=Geo_m(2,i);
    L_m(1,i)=Geo_m(3,i);
    sL_m(1,i)=Geo_m(4,i);
    fL_m(1,i)=Geo_m(5,i);
end

%Initalize Flow and Depth Matrix
for i=100:numsteps
    for j=1:numreaches+1
        Q_s(i,j)=0;
        Q_f(i,j)=0;
        d(i,j)=0.1;
    end
end

%Interative Process to Solve for dg, Qs, Qf
for i=100:numsteps
    for j=1:numreaches+1
        while Q_f(i,j)+Q_s(i,j)<AQ(i,j)
            if d(i,j)<h_m(1,j)

Q_s(i,j)=1/AnS(i,j)*(w_m(1,j)*d(i,j))*((w_m(1,j)*d(i,j))/(w
_m(1,j)+2*d(i,j)))^(2/3)*(ASf(i,j))^(1/2);
                Q_f(i,j)=0;

R_s(i,j)=((w_m(1,j)*d(i,j))/(w_m(1,j)+2*d(i,j)));
                R_f(i,j)=0;
                A_s(i,j)=w_m(1,j)*d(i,j);
```

```
                A_f(i,j)=0;
                d(i,j)=d(i,j)+0.001;
            else

Q_s(i,j)=1/AnS(i,j)*(w_m(1,j)*d(i,j))*((w_m(1,j)*d(i,j))/(w
_m(1,j)+2*h_m(1,j)))^(2/3)*ASf(i,j)^(1/2);
                Q_f(i,j)=1/AnF(i,j)*(2*(L_m(1,j)*(d(i,j)-
h_m(1,j))))*((2*(L_m(1,j)*(d(i,j)-h_m(1,j))))/(2*(d(i,j)-
h_m(1,j))+2*L_m(1,j)))^(2/3)*ASf(i,j)^(1/2);

R_s(i,j)=((w_m(1,j)*d(i,j))/(w_m(1,j)+2*h_m(1,j)));
                R_f(i,j)=((2*(L_m(1,j)*(d(i,j)-
h_m(1,j))))/(2*(d(i,j)-h_m(1,j))+2*L_m(1,j)));
                A_s(i,j)=w_m(1,j)*d(i,j);
                A_f(i,j)=2*(L_m(1,j)*(d(i,j)-h_m(1,j)));
                d(i,j)=d(i,j)+0.001;
            end
        end
    end
end

%Create Negative Flows
for i=100:numsteps
    for j=1:numreaches
        if Sf(i,7+6*(j-1))<0
            Q_s(i,j+1)=Q_s(i,j+1)*-1;
            Q_f(i,j+1)=Q_f(i,j+1)*-1;
        end
    end
end

%Surface Areas
for i=1:numreaches
    SA_s(1,i)=w_m(1,i)*sL_m(1,i);
    SA_f(1,i)=(2*L_m(1,i))*fL_m(1,i);
end

%Initial Reach Volume Estimates
for i=1:5
    V_f(100,i)=0;
end

V_s(100,1)=156000;
V_s(100,2)=230000;
V_s(100,3)=500000;
V_s(100,4)=237000;
V_s(100,5)=228000;
```

```
d_s(100,6)=d(1,6);
d_f(100,6)=0;

for i=1:5
    V_t(100,i)=V_s(100,i)+V_f(100,i);
end

for j=1:numreaches
        V_si(100,j)=V_s(100,j);
        d_s(100,j)=V_s(100,j)/SA_s(1,j);
        d_f(100,j)=V_f(100,j)/SA_f(1,j);
    if d_f(100,j)+h_m(1,j)<d_s(100,j)
            while d_f(100,j)+h_m(1,j)<d_s(100,j)
                d_s(100,j)=d_s(100,j)-0.001;
                V_s(100,j)=d_s(100,j)*SA_s(1,j);
                V_f(100,j)=V_t(100,j)-V_s(100,j);
                d_f(100,j)=V_f(100,j)/SA_f(1,j);
            end
            Exchange(100,j)=V_s(100,j)-V_si(100,j);
    end
end

for i=1:5
    V_t(100,i)=V_s(100,i)+V_f(100,i);
end

Q_t(:,1)=Q_m(:,1);
Q_t(:,2)=Q_m(:,7);
Q_t(:,3)=Q_m(:,13);
Q_t(:,4)=Q_m(:,19);
Q_t(:,5)=Q_m(:,25);
Q_t(:,6)=Q_m(:,31);

for i=101:numsteps
    for j=1:numreaches
        V_t(i,j)=V_t(i-1,j)+Q_t(i,j)*deltat-
Q_t(i,j+1)*deltat;
        V_s(i,j)=V_s(i-1,j)+Q_s(i,j)*deltat-
Q_s(i,j+1)*deltat;
        V_f(i,j)=V_f(i-1,j)+Q_f(i,j)*deltat-
Q_f(i,j+1)*deltat;
    end
end

%Reach Volume Calculations
for i=101:numsteps
    for j=1:numreaches
```

```
    V_si(i,j)=V_s(i-1,j)+Q_s(i,j)*deltat-Q_s(i,j+1)*deltat;
    V_fi(i,j)=V_f(i-1,j)+Q_f(i,j)*deltat-Q_f(i,j+1)*deltat;

        if V_si(i,j)>V_t(i,j)
            V_si(i,j)=V_t(i,j);
        end

        if V_fi(i,j)<0
            V_fi(i,j)=0;
            V_si(i,j)=V_t(i,j);
        end

        d_s(i,j)=V_si(i,j)/SA_s(1,j);
        d_f(i,j)=V_fi(i,j)/SA_f(1,j);

        if d_f(i,j)+h_m(1,j)<d_s(i,j)
            while d_f(i,j)+h_m(1,j)<d_s(i,j)
                d_s(i,j)=d_s(i,j)-0.001;
                V_s(i,j)=d_s(i,j)*SA_s(1,j);
                V_f(i,j)=V_t(i,j)-V_s(i,j);
                d_f(i,j)=V_f(i,j)/SA_f(1,j);
            end
            Exchange(i,j)=V_s(i,j)-V_si(i,j);
        elseif d_f(i,j)>0 && d_f(i,j)+h_m(1,j)>d_s(i,j)
            while d_f(i,j)+h_m(1,j)>d_s(i,j)
                d_f(i,j)=d_f(i,j)-0.001;
                V_f(i,j)=d_f(i,j)*SA_f(1,j);
                V_s(i,j)=V_t(i,j)-V_f(i,j);
                d_s(i,j)=V_s(i,j)/SA_s(1,j);
            end
            Exchange(i,j)=V_s(i,j)-V_si(i,j);
        elseif d_f(i,j)==0
            V_f(i,j)=0;
            V_s(i,j)=V_t(i,j);
            d_s(i,j)=V_s(i,j)/SA_s(1,j);
            Exchange(i,j)=0;
        end

        if V_s(i,j)<0
            V_s(i,j)=0.01;
        end

if d_f(i,j)<0
    d_f(i,j)=0;
end
        Vtcheck(i,j)=V_s(i,j)+V_f(i,j);
```

```
        Vterror(i,j)=Vtcheck(i,j)-V_t(i,j);
    end

end

%HR Calculation with adjusted Depth
for i=101:numsteps
    for j=1:numreaches
        if d_s(i,j)<h_m(1,j)
HR_s(i,j)=((w_m(1,j)*d_s(i,j))/(w_m(1,j)+2*d_s(i,j)));
            HR_f(i,j)=0;
        else
HR_s(i,j)=((w_m(1,j)*d_s(i,j))/(w_m(1,j)+2*h_m(1,j)));
HR_f(i,j)=(2*(L_m(1,j))*(d_f(i,j)))/(2*(d_f(i,j)+2*L_m(1,j)
));
        end
    end
end

%Reach Average Flowrates
for i=101:numsteps
    for j=2:6
        QR_s(i,j)=(Q_s(i,j-1)+Q_s(i,j))/2;
        QR_f(i,j)=(Q_f(i,j-1)+Q_f(i,j))/2;
    end
end

%Reach Average Fricition Slope
for i=1:numsteps
    for j=1:numxs
        Sf(i,j)=abs(Sf(i,j));
    end
end

Sf_R1=Sf(:,1:6);
for i=100:numsteps
   SfR_R1(i)=mean(Sf_R1(i,:));
end
SfR_R1=SfR_R1';

Sf_R2=Sf(:,7:12);
for i=100:numsteps
    SfR_R2(i)=mean(Sf_R2(i,:));
end
SfR_R2=SfR_R2';

Sf_R3=Sf(:,13:18);
```

```
for i=100:numsteps
    SfR_R3(i)=mean(Sf_R3(i,:));
end
SfR_R3=SfR_R3';

Sf_R4=Sf(:,19:24);
for i=100:numsteps
    SfR_R4(i)=mean(Sf_R4(i,:));
end
SfR_R4=SfR_R4';
Sf_R5=Sf(:,25:30);
for i=100:numsteps
    SfR_R5(i)=mean(Sf_R5(i,:));
end
SfR_R5=SfR_R5';

SfR=[SfR_R1,SfR_R2,SfR_R3,SfR_R4,SfR_R5,Sf(:,31)];

for i=1:numsteps
    for j=1:numreaches
        if d_s(i,j)<0.2 && SfR(i,j)>0.004667
            SfR(i,j)=0.004667;
        end
    end
end

BC_SSC=xlsread("Boundary Data","Sheet2",'A1:B35041');

for i=101:numsteps
    Upcon(i,1)=BC_SSC(i,1)/(Q_s(i,1)+Q_f(i,1));
    SS_s(i,1)=Upcon(i,1)*Q_s(i,1);
    SS_f(i,1)=Upcon(i,1)*Q_f(i,1);
    if Q_s(i,6)<0
        SS_s(i-1,7)=-BC_SSC(i,2);
        SS_f(i,7)=0;
    else
        SS_s(i-1,7)=BC_SSC(i,2);
        SS_f(i,7)=0;
    end
end

%Calibration Parameters
Ctc_H_s=7.04*10^-6;      %m^1/2 s^2 kg^-1/2
Ctc_L_s=5.67446;      %m^1/2 s^2 kg^-1/2
Ctc_H_f=7.75*10^-6;      %m^1/2 s^2 kg^-1/2
Ctc_L_f=5.69745;      %m^1/2 s^2 kg^-1/2
alpha=8.08167;
```

```
lambda=0.383364;
w_s=2.42*10^-4;   %meter/second
tcr_s=0.09831;
tcr_f=0.090831;
tcr_b=2.054;
a_s=0.000347;
a_b=9.85*10^-5;
a_f=0.000347;

%Calculate Fluid Shear Stress
for i=101:numsteps
    for j=1:numreaches
        tf_s(i,j)=rho_w*g.*HR_s(i,j)*SfR(i,j);    % average
fluid shear stress in the stream channel in pa
        tf_f(i,j)=rho_w*g.*HR_f(i,j)*SfR(i,j);    % average
fluid shear stress in the floodplain in pa
        tf_b(i,j)=(tf_f(i,j)+tf_s(i,j))/2;
    end
end

for i=100:numsteps
    for j=1:6
        Vel_s(i,j)=abs(Q_s(i,j))/A_s(i,j);
        if A_f(i,j)>0
            Vel_f(i,j)=abs(Q_f(i,j))/A_f(i,j);
        else
            Vel_f(i,j)=0;
        end
    end
    for j=1:5
        AVel_s(i,j)=(Vel_s(i,j)+Vel_s(i,j+1))/2;
        AVel_f(i,j)=(Vel_f(i,j)+Vel_f(i,j+1))/2;
    end
end

%Calculate Transport Capacity
for i=101:numsteps
    for j=1:numreaches
        if j==1
            Vel_s=0.5;
            Vel_f=0.04;
        elseif j==2
            Vel_s=0.2;
            Vel_f=0.04;
        elseif j==3
            Vel_s=0.15;
            Vel_f=0.04;
```

```
        elseif j==4
            Vel_s=0.1;
            Vel_f=0.04;
        elseif j==5
            Vel_s=0.4;
            Vel_f=0.04;
        end

        if AVel_s(i,j)>Vel_s

Tc_s(i,j)=Ctc_H_s*tf_s(i,j)^1.5*sL_m(1,j)*deltat;
        else

Tc_s(i,j)=Ctc_L_s*tf_s(i,j)^1.5*sL_m(1,j)*deltat;
        end
        if AVel_f(i,j)>Vel_f

Tc_f(i,j)=Ctc_H_f*tf_f(i,j)^1.5*fL_m(1,j)*deltat;
        else

Tc_f(i,j)=Ctc_L_f*tf_f(i,j)^1.5*fL_m(1,j)*deltat;
        end
    end
end

%Calculate Surface Area for the Banks
for i=101:numsteps
    for j=1:numreaches
        if d_s(i,j)<h_m(1,j)
            SA_b(i,j)=2*d_s(i,j)*sL_m(1,j);
        else
            SA_b(i,j)=2*h_m(1,j)*sL_m(1,j);
        end
    end
end

%Adjust Matrix Size
for j=5:-1:1
    tf_s(:,j+1)=tf_s(:,j);
    tf_f(:,j+1)=tf_f(:,j);
    tf_b(:,j+1)=tf_b(:,j);
    Tc_s(:,j+1)=Tc_s(:,j);
    Tc_f(:,j+1)=Tc_f(:,j);
    SA_b(:,j+1)=SA_b(:,j);
    V_f(:,j+1)=V_f(:,j);
    V_s(:,j+1)=V_s(:,j);
    Exchange(:,j+1)=Exchange(:,j);
```

```
    SA_s(:,j+1)=SA_s(:,j);
    SA_f(:,j+1)=SA_f(:,j);
    L_m(:,j+1)=L_m(:,j);
    d_s(:,j+1)=d_s(:,j);
end

%Inital Values
tf_s(:,1)=0;
tf_f(:,1)=0;
tf_b(:,1)=0;
Tc_s(:,1)=0;
Tc_f(:,1)=0;
SA_b(:,1)=0;
V_f(:,1)=1;
V_s(:,1)=1;
Exchange(:,1)=0;
SA_s(:,1)=0;
SA_f(:,1)=0;
L_m(:,1)=0;
V_f(:,7)=1;
V_s(:,7)=1;
d_s(:,1)=0;
Q_FWS(:,1)=Q(:,31);
SS_s(100,2)=25;      %Suspended Sediment in Reach 1
SS_f(100,2)=25;       %Suspended Sediment in Reach 1
SS_s(100,3)=25;      %Suspended Sediment in Reach 2
SS_f(100,3)=25;       %Suspended Sediment in Reach 2
SS_s(100,4)=25;      %Suspended Sediment in Reach 3
SS_f(100,4)=25;       %Suspended Sediment in Reach 3
SS_s(100,5)=25;      %Suspended Sediment in Reach 4
SS_f(100,5)=25;       %Suspended Sediment in Reach 4
SS_s(100,6)=25;      %Suspended Sediment in Reach 5
SS_f(100,6)=25;       %Suspended Sediment in Reach 5

S_s(100,1:6)=1000;
S_b(100,1:6)=10000000000000000000000000;
S_f(100,1:6)=10000000000000000000000000;

%Sediment Transport Model
for i=101:numsteps
    if Q_FWS(i)>0
        for j=2:6
            if i==23780
                stop=1;
            end
            if Tc_s(i,j)>SS_s(i-1,j)
                if Tc_s(i,j)>SS_s(i-1,j)
```

```
            E_b(i,j)=min(min(a_b.*(tf_b(i,j)-
            tcr_b).^b_b.*SA_b(i,j).*deltat,Tc_s(i,j
            )-SS_s(i-1,j)),S_b(i-1,j));
            if E_b(i,j)<0
                E_b(i,j)=0;
            end
        else
            E_b(i,j)=0;
        end
    else
        E_b(i,j)=0;
    end
    if Tc_f(i,j)>SS_f(i-1,j)
       E_f(i,j)=min(min(a_f.*(tf_f(i,j)-
       tcr_f).^b_f.*SA_f(1,j).*deltat,Tc_f(i,j)-
       SS_f(i-1,j)),S_f(i-1,j));
        if E_f(i,j)<0
            E_f(i,j)=0;
        end
    else
        E_f(i,j)=0;
    end
    if Tc_f(i,j)<SS_f(i-1,j)
        if V_f(i,j)>0
            D_f(i,j)=(SS_f(i-1,j)/V_f(i-
            1,j)*abs(QR_f(i,j)))/(alpha*(2*L_m(1,j)
            )^2*(1-lambda))*(1-exp(-
            w_s*alpha*(2*L_m(1,j))^2/abs(QR_f(i,j))
            ))*SA_f(1,j)*deltat;
            if D_f(i,j)>SS_f(i-1,j)
                D_f(i,j)=SS_f(i-1,j);
            end
        else
            D_f(i,j)=0;
        end
    else
        D_f(i,j)=0;
    end
    if j==2
        Qssin_s(i,j)=SS_s(i-1,j-1);
        Qssin_f(i,j)=SS_f(i-1,j-1);
    else
       Qssin_s(i,j)=SS_s(i-1,j-1)/V_s(i-1,j-
       1)*Q_s(i,j-1);
        if Qssin_s(i,j)*deltat>SS_s(i-1,j-1)
            Qssin_s(i,j)=SS_s(i-1,j-1)/900;
        else
```

```
                    Qssin_s(i,j)=Qssin_s(i,j);
                end
                if V_f(i-1,j-1)>0
                    Qssin_f(i,j)=SS_f(i-1,j-1)/V_f(i-1,j-
                    1)*Q_f(i,j-1);
                    if Qssin_f(i,j)*deltat>SS_f(i-1,j-1)
                        Qssin_f(i,j)=SS_f(i-1,j-1)/900;
                    else
                        Qssin_f(i,j)=Qssin_f(i,j);
                    end
                else
                    Qssin_f(i,j)=0;
                end
            end
            Qssout_s(i,j)=SS_s(i-1,j)/V_s(i-1,j)*Q_s(i,j);
            if Qssout_s(i,j)*deltat>SS_s(i-1,j)
                Qssout_s(i,j)=SS_s(i-1,j)/900;
            else
                Qssout_s(i,j)=Qssout_s(i,j);
            end
            if V_f(i-1,j)>0
               Qssout_f(i,j)=SS_f(i-1,j)/V_f(i-
               1,j)*Q_f(i,j);
                if Qssout_f(i,j)*deltat>SS_f(i-1,j)
                    Qssout_f(i,j)=SS_f(i-1,j)/900;
                else
                    Qssout_f(i,j)=Qssout_f(i,j);
                end
            else
                Qssout_f(i,j)=0;
            end
          SS_s(i,j)=SS_s(i-
          1,j)+E_b(i,j)+Qssin_s(i,j)*deltat-
          Qssout_s(i,j)*deltat;
          SS_f(i,j)=SS_f(i-1,j)+E_f(i,j)-
          D_f(i,j)+Qssin_f(i,j)*deltat-
          Qssout_f(i,j)*deltat;
            if SS_f(i,j)<0
                D_f(i,j)=D_f(i,j)+SS_f(i,j);
                SS_f(i,j)=0;
            end
            if Exchange(i,j)<0

mix_f(i,j)=SS_s(i,j)/V_s(i,j)*abs(Exchange(i,j));
                if mix_f(i,j)>SS_s(i,j)
                    mix_f(i,j)=SS_s(i,j);
                end
```

```
                mix_s(i,j)=-(mix_f(i,j));
            elseif Exchange(i,j)>0
                if V_f(i,j)>0

mix_s(i,j)=SS_f(i,j)/V_f(i,j)*abs(Exchange(i,j));

                    if mix_s(i,j)>SS_f(i,j)
                        mix_s(i,j)=SS_f(i,j);
                    end
                    mix_f(i,j)=-(mix_s(i,j));
                else
                    mix_s(i,j)=SS_f(i,j);
                    mix_f(i,j)=-(mix_s(i,j));
                end
            else
                mix_s(i,j)=0;
                mix_f(i,j)=0;
            end
            SS_s(i,j)=SS_s(i,j)+mix_s(i,j);
            SS_f(i,j)=SS_f(i,j)+mix_f(i,j);
            S_b(i,j)=S_b(i-1,j)-E_b(i,j);
            S_f(i,j)=S_f(i-1,j)+D_f(i,j)-E_f(i,j);
        end
    elseif Q_FWS(i)<0
        for j=6:-1:2
            if i==23780
                stop=1;
            end
            if Tc_s(i,j)>SS_s(i-1,j)
                if Tc_s(i,j)>SS_s(i-1,j)
                    E_b(i,j)=min(min(a_b.*(tf_b(i,j)-
                    tcr_b).^b_b.*SA_b(i,j).*deltat,Tc_s(i,j
                    )-SS_s(i-1,j)),S_b(i-1,j));
                    if E_b(i,j)<0
                        E_b(i,j)=0;
                    end
                else
                    E_b(i,j)=0;
                end
            else
                E_b(i,j)=0;
            end
            if Tc_f(i,j)>SS_f(i-1,j)
               E_f(i,j)=min(min(a_f.*(tf_f(i,j)-
               tcr_f).^b_f.*SA_f(1,j).*deltat,Tc_f(i,j)-
               SS_f(i-1,j)),S_f(i-1,j));
                if E_f(i,j)<0
```

```
        E_f(i,j)=0;
    end
else
    E_f(i,j)=0;
end
if Tc_f(i,j)<SS_f(i-1,j)
    if V_f(i,j)>0
        D_f(i,j)=(SS_f(i-1,j)/V_f(i-
        1,j)*abs(QR_f(i,j)))/(alpha*(2*L_m(1,j)
        )^2*(1-lambda))*(1-exp(-
        w_s*alpha*(2*L_m(1,j))^2/abs(QR_f(i,j))
        ))*SA_f(1,j)*deltat;
        if D_f(i,j)>SS_f(i-1,j)
            D_f(i,j)=SS_f(i-1,j);
        end
    else
        D_f(i,j)=0;
    end
else
    D_f(i,j)=0;
end
if Q_s(i,j-1)<0 && Q_s(i,j)<0
    if j==6
        Qssout_s(i,j)=SS_s(i-1,j+1);
        Qssout_f(i,j)=SS_f(i-1,j+1);
    else
        Qssout_s(i,j)=SS_s(i-1,j+1)/V_s(i-
        1,j+1)*Q_s(i,j);
        if abs(Qssout_s(i,j))*deltat>SS_s(i-
        1,j+1)
            Qssout_s(i,j)=-SS_s(i-1,j+1)/900;
        else
            Qssout_s(i,j)=Qssout_s(i,j);
        end
        if V_f(i-1,j+1)>0
        Qssout_f(i,j)=SS_f(i-1,j+1)/V_f(i-
        1,j+1)*Q_f(i,j);
             if
             abs(Qssout_f(i,j))*deltat>SS_f(i-
             1,j+1)
                Qssout_f(i,j)=-SS_f(i-
                1,j+1)/900;
            else
                Qssout_f(i,j)=Qssout_f(i,j);
            end
        else
            Qssout_f(i,j)=0;
```

```
            end
        end
            Qssin_s(i,j)=SS_s(i-1,j)/V_s(i-
            1,j)*Q_s(i,j-1);
        if abs(Qssin_s(i,j))*deltat>SS_s(i-1,j)
            Qssin_s(i,j)=-SS_s(i-1,j)/900;
        else
            Qssin_s(i,j)=Qssin_s(i,j);
        end
        if V_f(i-1,j)>0
            Qssin_f(i,j)=SS_f(i-1,j)/V_f(i-
            1,j)*Q_f(i,j-1);
            if abs(Qssin_f(i,j))*deltat>SS_f(i-1,j)
                Qssin_f(i,j)=-SS_f(i-1,j)/900;
            else
                Qssin_f(i,j)=Qssin_f(i,j);
            end
        else
            Qssin_f(i,j)=0;
        end
    elseif Q_s(i,j-1)>0 && Q_s(i,j)<0
        for k=2:j-1
            if k==2
                Qssin_s(i,k)=SS_s(i-1,k-1);
                Qssin_f(i,k)=SS_f(i-1,k-1);
            else
                 Qssin_s(i,k)=SS_s(i-1,k-1)/V_s(i-
                 1,k-1)*Q_s(i,k-1);
                if Qssin_s(i,k)*deltat>SS_s(i-1,k-
                1)
                    Qssin_s(i,k)=SS_s(i-1,k-1)/900;
                else
                    Qssin_s(i,k)=Qssin_s(i,k);
                end
                if V_f(i-1,k-1)>0
                 Qssin_f(i,k)=SS_f(i-1,k-1)/V_f(i-
                 1,k-1)*Q_f(i,k-1);
                      if
                      Qssin_f(i,k)*deltat>SS_f(i-
                      1,k-1)
                      Qssin_f(i,k)=SS_f(i-1,k-
                      1)/900;
                    else
                        Qssin_f(i,k)=Qssin_f(i,k);
                    end
                else
                    Qssin_f(i,k)=0;
```

```
                    end
                end
                Qssout_s(i,k)=SS_s(i-1,k)/V_s(i-
                1,k)*Q_s(i,k);
                if Qssout_s(i,k)*deltat>SS_s(i-1,k)
                    Qssout_s(i,k)=SS_s(i-1,k)/900;
                else
                    Qssout_s(i,k)=Qssout_s(i,k);
                end
                if V_f(i-1,k)>0
                Qssout_f(i,k)=SS_f(i-1,k)/V_f(i-
                1,k)*Q_f(i,k);
                    if Qssout_f(i,k)*deltat>SS_f(i-1,k)
                        Qssout_f(i,k)=SS_f(i-1,k)/900;
                    else
                        Qssout_f(i,k)=Qssout_f(i,k);
                    end
                else
                    Qssout_f(i,k)=0;
                end
                SS_s(i,k)=SS_s(i-
                1,k)+E_b(i,k)+Qssin_s(i,k)*deltat-
                Qssout_s(i,k)*deltat;
                SS_f(i,k)=SS_f(i-1,k)+E_f(i,k)-
                D_f(i,k)+Qssin_f(i,k)*deltat-
                Qssout_f(i,k)*deltat;
                if Exchange(i,k)<0
mix_f(i,k)=SS_s(i,k)/V_s(i,k)*abs(Exchange(i,k));
                    if mix_f(i,k)>SS_s(i,k)
                        mix_f(i,k)=SS_s(i,k);
                    end
                    mix_s(i,k)=-(mix_f(i,k));
                elseif Exchange(i,k)>0
                    if V_f(i,k)>0
mix_s(i,k)=SS_f(i,k)/V_f(i,k)*abs(Exchange(i,k));
                        if mix_s(i,k)>SS_f(i,k)
                            mix_s(i,k)=SS_f(i,k);
                        end
                        mix_f(i,k)=-(mix_s(i,k));
                    else
                        mix_s(i,k)=SS_f(i,k);
                        mix_f(i,k)=-(mix_s(i,k));
                    end
                else
                    mix_s(i,k)=0;
                    mix_f(i,k)=0;
                end
```

```
        SS_s(i,k)=SS_s(i,k)+mix_s(i,k);
        SS_f(i,k)=SS_f(i,k)+mix_f(i,k);
        if SS_f(i,k)<0
            D_f(i,k)=D_f(i,k)+SS_f(i,k);
            SS_f(i,k)=0;
        end
        S_b(i,k)=S_b(i-1,k)-E_b(i,k);
        S_f(i,k)=S_f(i-1,k)+D_f(i,k)-E_f(i,k);
    end
    if j==2
        Qssin_s(i,j)=SS_s(i-1,j-1);
        Qssin_f(i,j)=SS_f(i-1,j-1);
    else
        Qssin_s(i,j)=SS_s(i-1,j-1)/V_s(i-1,j-
        1)*Q_s(i,j-1);
        if Qssin_s(i,j)*deltat>SS_s(i-1,j-1)
            Qssin_s(i,j)=SS_s(i-1,j-1)/900;
        else
            Qssin_s(i,j)=Qssin_s(i,j);
        end
        if V_f(i-1,j-1)>0
        Qssin_f(i,j)=SS_f(i-1,j-1)/V_f(i-1,j-
        1)*Q_f(i,j-1);
            if Qssin_f(i,j)*deltat>SS_f(i-1,j-1)
                Qssin_f(i,j)=SS_f(i-1,j-1)/900;
            else
                Qssin_f(i,j)=Qssin_f(i,j);
            end
        else
            Qssin_f(i,j)=0;
        end
    end
   Qssout_s(i,j)=SS_s(i-1,j+1)/V_s(i-
   1,j+1)*Q_s(i,j);
    if abs(Qssout_s(i,j))*deltat>SS_s(i-1,j+1)
        Qssout_s(i,j)=-SS_s(i-1,j+1)/900;
    else
        Qssout_s(i,j)=Qssout_s(i,j);
    end
    if V_f(i-1,j+1)>0
        Qssout_f(i,j)=SS_f(i-1,j+1)/V_f(i-
        1,j+1)*Q_f(i,j);
        if abs(Qssout_f(i,j))*deltat>SS_f(i-
        1,j+1)
            Qssout_f(i,j)=-SS_f(i-1,j+1)/900;
        else
            Qssout_f(i,j)=Qssout_f(i,j);
```

```
                    end
                else
                    Qssout_f(i,j)=0;
                end
            end
            SS_s(i,j)=SS_s(i-
            1,j)+E_b(i,j)+Qssin_s(i,j)*deltat-
            Qssout_s(i,j)*deltat;
            SS_f(i,j)=SS_f(i-1,j)+E_f(i,j)-
            D_f(i,j)+Qssin_f(i,j)*deltat-
            Qssout_f(i,j)*deltat;
            if SS_f(i,j)<0
                D_f(i,j)=D_f(i,j)+SS_f(i,j);
                SS_f(i,j)=0;
            end
            if Exchange(i,j)<0

mix_f(i,j)=SS_s(i,j)/V_s(i,j)*abs(Exchange(i,j));
                if mix_f(i,j)>SS_s(i,j)
                    mix_f(i,j)=SS_s(i,j);
                end
                mix_s(i,j)=-(mix_f(i,j));
            elseif Exchange(i,j)>0
                if V_f(i,j)>0

mix_s(i,j)=SS_f(i,j)/V_f(i,j)*abs(Exchange(i,j));
                    if mix_s(i,j)>SS_f(i,j)
                        mix_s(i,j)=SS_f(i,j);
                    end
                    mix_f(i,j)=-(mix_s(i,j));
                else
                    mix_s(i,j)=SS_f(i,j);
                    mix_f(i,j)=-(mix_s(i,j));
                end
            else
                mix_s(i,j)=0;
                mix_f(i,j)=0;
            end
            SS_s(i,j)=SS_s(i,j)+mix_s(i,j);
            SS_f(i,j)=SS_f(i,j)+mix_f(i,j);
            S_b(i,j)=S_b(i-1,j)-E_b(i,j);
            S_f(i,j)=S_f(i-1,j)+D_f(i,j)-E_f(i,j);
        end
    end
end
```

```
for i=100:numsteps
    InUpS(i)=Qssin_s(i,2);
    InUpF(i)=Qssin_f(i,2);
    if Q_s(i,6)<0
        InDownS(i)=Qssout_s(i,6);
        OutDownS(i)=0;
    else
        OutDownS(i)=Qssout_s(i,6);
        InDownS(i)=0;
    end
    if Q_f(i,6)<0
        InDownF(i)=Qssout_f(i,6);
        OutDownF(i)=0;
    else
        OutDownF(i)=Qssout_f(i,6);
        InDownF(i)=0;
    end
end

MixF=sum(mix_f,'all');
EroF=sum(E_f,'all');
DepF=sum(D_f,'all');
EroB=sum(E_b,'all');
TSSF=SS_f(35040,2)+SS_f(35040,3)+SS_f(35040,4)+SS_f(35040,5
)+SS_f(35040,6);
NetF=sum(InUpF)*900-sum(InDownF)*900-sum(OutDownF)*900-
TSSF+125+MixF+EroF-DepF;
TSSS=SS_s(35040,2)+SS_s(35040,3)+SS_s(35040,4)+SS_s(35040,5
)+SS_s(35040,6);
NetS=sum(InUpS)*900-sum(InDownS)*900-sum(OutDownS)*900-
TSSS+125-MixF+EroB;
InUp=sum(InUpF)+sum(InUpS);
InDown=sum(InDownF)+sum(InDownS);
OutDown=sum(OutDownF)+sum(OutDownS);
TSS=TSSF+TSSS;
Net=InUp*900-InDown*900-OutDown*900-TSS+250-DepF+EroF+EroB;

Outlet_obs=BC_SSC(:,2);
for i=192:numsteps
    if Q_s(i,6)>0
        Qss_obs(i)=Outlet_obs(i);
        Qss_sim(i)=Qssout_s(i,6);
    else
        Qss_obs(i)=0;
        Qss_sim(i)=0;
    end
end
```

```
Qss_obs=Qss_obs';
Qss_sim=Qss_sim';
X_mat=[Qss_obs,Qss_sim];
Y_obs_day=sum(reshape(Qss_obs,96,365));
Y_sim_day=sum(reshape(Qss_sim,96,365));
Y_obs_day=Y_obs_day';
Y_sim_day=Y_sim_day';
Y_mat=[Y_obs_day,Y_sim_day];
indices=find(Y_mat(:,1)==0);
Y_mat(indices,:)=[];
Y_obs_day=Y_mat(:,1);
Y_sim_day=Y_mat(:,2);

load('rand_days');

%NSE for Calibration Period
count(1)=0;
for i=1:356
    if i==rand_days(i-count(i))
        Cal_Y_obs_day(i)=Y_obs_day(i);
        Cal_Y_sim_day(i)=Y_sim_day(i);
        count(i+1)=count(i);
    else
        Cal_Y_obs_day(i)=0;
        Cal_Y_sim_day(i)=0;
        count(i+1)=count(i)+1;
    end
end
Cal_Y_obs_day=Cal_Y_obs_day';
Cal_Y_sim_day=Cal_Y_sim_day';
Cal_Y_mat=[Cal_Y_obs_day,Cal_Y_sim_day];
indices=find(Cal_Y_mat(:,1)==0);
Cal_Y_mat(indices,:)=[];
Cal_Y_obs_day=Cal_Y_mat(:,1);
Cal_Y_sim_day=Cal_Y_mat(:,2);
Cal_Y_mean=mean(Cal_Y_obs_day);

for i=1:240
    num_NSE(i)=(Cal_Y_obs_day(i)-Cal_Y_sim_day(i))^2;
    den_NSE(i)=(Cal_Y_obs_day(i)-Cal_Y_mean)^2;
end
sum_num_NSE=sum(num_NSE,2);
sum_den_NSE=sum(den_NSE,2);
NSE=1-[sum_num_NSE/sum_den_NSE];

%Pbias for Calibration Period
```

```
for i=1:240
    num_Pbias(i)=(Cal_Y_obs_day(i)-Cal_Y_sim_day(i))*100;
    den_Pbias(i)=Cal_Y_obs_day(i);
end
sum_num_Pbias=sum(num_Pbias,2);
sum_den_Pbias=sum(den_Pbias,2);
Pbias=1-[sum_num_Pbias/sum_den_Pbias];
```

REFERENCES

Alexander, R. B., Smith, R. A., Schwarz, G. E., Boyer, E. W., Nolan, J. V., & Brakebill, J. W. (2008). Differences in Phosphorus and Nitrogen Delivery to The Gulf of Mexico from the Mississippi River Basin. doi:10.1021/es0716103

Arp, C. D., & Cooper, D. J. (2004). Analysis of Sediment Retention in Western Riverine Wetlands: The Yampa River Watershed, Colorado, USA. *Environmental Management*. doi:10.1007/s00267-004-0027-8

ATSM. (2002). Standard test methods for determining sediment concentration in water samples. D3977–97.

Banach, A. M., K. Banach, E. J. W. Visser, Z. Stepniewska, A. J. M. Smits, J. G. M. Roelofs, and L. P. M. Lamers (2009), Effects of summer flooding on floodplain biogeochemistry in Poland: Implications for increased flooding frequency, Biogeochemistry, 92(3), 247–262.

Benda, L., Andras, K., Miller, D., Bigelow, P. (2004). Confluence effects in rivers: Interactions of basin scale, network geometry, and disturbance regimes. WRR, 40:W05402.

Beschta, R.L. (1987). Conceptual models of sediment transport in streams. In: Thorne, C.R., Bathurst, J.C., Hey, R.D. (Eds.), Sediment Transport in Gravel-bed Rivers. Wiley, pp. 387–419.

Best, J. L. (1986), The morphology of river channel confluences, Prog. Phys. Geogr., 10, 157 – 174.

Bolstad, P., Jenks, A., Riedel, M., & Vose, J. M. (2006). Estimating Sediment Yield in the Southern Appalachians using WCS-SED. Retrieved July, 2020, from http://www.srs.fs.fed.us/pubs/ja/ja_vose015.pdf

Bright, C. E., Mager, S. M., & Horton, S. L. (2018). Predicting suspended sediment concentration from nephelometric turbidity in organic-rich waters. *River Research and Applications, 34*(7), 640-648. doi:10.1002/rra.3305

Burns, M., & MacArthur, R. (1996). Sediment Deposition in Jennings Randolph Reservoir, Maryland and West Virginia. Retrieved 2020, from https://acwi.gov/sos/pubs/6thFISC/6Fisc-V2/6Fsc2-10.pdf

Butturini, A., Alvarez, M., Bernal, S., Vazquez, E., & Sabater, F. (2008). Diversity and temporal sequences of forms of DOC and NO3-discharge responses in an intermittent stream: Predictable or random succession? *Journal of Geophysical Research, 113*(G3). doi:10.1029/2008jg000721

Campbell, J. L., Rustad, L. E., Porter, J. H., Taylor, J. R., Dereszynski, E. W., Shanley, J. B., . . . Boose, E. R. (2013). Quantity is Nothing without Quality: Automated QA/QC for Streaming Environmental Sensor Data. *BioScience, 63*(7), 574-585. doi:10.1525/bio.2013.63.7.10

Caraco, N. F., Cole, J. J., & Likens, G. E. (1989). Evidence for sulphate-controlled phosphorus release from sediments of aquatic systems. *Nature, 341*(6240), 316-318. doi:10.1038/341316a0

Carey, R. O., Wollheim, W. M., Mulukutla, G. K., & Mineau, M. M. (2014). Characterizing storm-event nitrate fluxes in a fifthorder suburbanizing watershed using in situ sensors. Environ. Sci. Tech., 48(14), 7756-7765. https://doi.org/10.1021/es500252j

Chaffin, J. D., & Bridgeman, T. B. (2013). Organic and inorganic nitrogen utilization by nitrogen-stressed cyanobacteria during bloom conditions. *Journal of Applied Phycology, 26*(1), 299-309. doi:10.1007/s10811-013-0118-0

Chaffin, J. D., Bridgeman, T. B., & Bade, D. L. (2013). Nitrogen Constrains the Growth of Late Summer Cyanobacterial Blooms in Lake Erie. *Advances in Microbiology, 03*(06), 16-26. doi:10.4236/aim.2013.36a003

Chang, H. H. (1988). *Fluvial processes in river engineering*. New York, NY: Wiley.

Chow, A. T., J. N. Dai, W. H. Conner, D. R. Hitchcock, and J. J. Wang (2013), Dissolved organic matter and nutrient dynamics of a coastal freshwater forested wetland in Winyah Bay, South Carolina, Biogeochemistry, 112(1–3), 571–587

Conroy, J. D., Kane, D. D., Briland, R. D., & Culver, D. A. (2014). Systemic, early-season Microcystis blooms in western Lake Erie and two of its major agricultural tributaries (Maumee and Sandusky rivers). doi:10.1016/j.jglr.2014.04.015

Cottingham, K. L., Ewing, H. A., Greer, M. L., Carey, C. C., & Weathers, K. C. (2015). Cyanobacteria as biological drivers of lake nitrogen and phosphorus cycling. *Ecosphere, 6*(1). doi:10.1890/es14-00174.1

Curtis, J.A., Flint, L.E., Alpers, C.N., Wright, S.A., and Snyder, N.P. (2006). Use of sediment rating curves and optical backscatter data to characterize sediment transport in the upper Yuba River watershed, California, 2001–03: U.S. Geological Survey Scientific Investigations Report 2005– 5246, 74 p.

Devereux, O. H., Prestegaard, K. L., Needelman, B. A., & Gellis, A. C. (2010). Suspended-sediment sources in an urban watershed, Northeast Branch Anacostia River, Maryland. *Hydrological Processes, 24*(11), 1391-1403. doi:10.1002/hyp.7604

Dijkstra, Y. M., Chant, R. J., & Reinfelder, J. R. (2019). Factors Controlling Seasonal Phytoplankton Dynamics in the Delaware River Estuary: An Idealized Model Study. *Estuaries and Coasts, 42*(7), 1839-1857. doi:10.1007/s12237-019-00612-3

Dun, S., Wu, J. Q., Elliot, W. J., Frankenberger, J. R., Flanagan, D. C., & Mccool, D. K. (2013). Applying Online WEPP to Assess Forest Watershed Hydrology. *Transactions of the ASABE, 56*(2), 581-590. doi:10.13031/2013.42689

Edmondson, WT. In: Nutrients and Eutrophication: The Limiting-Nutrient Controversy. Proceedings of a Symposium Held at the W.K. Kellogg Biological Station, Michigan State University, February 11–12, 1971. Likens GE, ed. Lawrence, KS: American Society of Limnology and Oceanography; 1972. Nutrients and phytoplankton in Lake Washington. pp. 172–193.

Elser, J. J., Bracken, M. E., Cleland, E. E., Gruner, D. S., Harpole, W. S., Hillebrand, H., . . . Smith, J. E. (2007). Global analysis of nitrogen and phosphorus limitation of primary producers in freshwater, marine and terrestrial ecosystems. *Ecology Letters, 10*(12), 1135-1142. doi:10.1111/j.1461-0248.2007.01113.x

Emerson, D. G., Vecchia, A. V., & Dahl, A. L. (2005). Evaluation of drainage-area ratio method used to estimate streamflow for the Red River of the North Basin, North Dakota and Minnesota. *Scientific Investigations Report*. doi:10.3133/sir20055017

EPA. Total Maximum Daily Load of Sediment in the Youghiogheny River Watershed, Garrett County, Maryland. (2007, February 21). Retrieved 2020, from https://mde.maryland.gov/programs/Water/TMDL/DocLib_Youghiogheny_05020201/Yough_Sedimets_TMDL_20060928_final.pdf

Evans, D.J., Johnes, P.J., Lawrence, D.S. (2003). Suspended and bed load sediment transport dynamics in two lowland UK streams — storm integrated monitoring. Erosion and Sediment Transport Measurement in Rivers: Technological and Methodological Advances. 283, pp. 103–110.

Ford, W. I., & Fox, J. F. (2017). Stabilization of benthic algal biomass in a temperate stream draining agroecosystems. *Water Research, 108*, 432-443. doi:10.1016/j.watres.2016.11.026

Ford, W., Fox, J., Mahoney, D., Degraves, G., Erhardt, A., & Yost, S. (2020). Backwater Confluences of the Ohio River: Organic and Inorganic Fingerprints Explain

Sediment Dynamics in Wetlands and Marinas. *JAWRA Journal of the American Water Resources Association*. doi:10.1111/1752-1688.12850

Fox, J. F., & Martin, D. K. (2015). Sediment Fingerprinting for Calibrating a Soil Erosion and Sediment-Yield Model in Mixed Land-Use Watersheds. *Journal of Hydrologic Engineering, 20*(6). doi:10.1061/(asce)he.1943-5584.0001011

Galloway, J. N., Townsend, A. R., Erisman, J. W., Bekunda, M., Cai, Z., Freney, J. R., … Sutton, M. A. (2008). Transformation of the Nitrogen Cycle: Recent Trends, Questions, and Potential Solutions. *Science, 320*(5878), 889-892. doi:10.1126/science.1136674

Gellis, A. (2013). Factors influencing storm-generated suspended-sediment concentrations and loads in four basins of contrasting land use, humid-tropical Puerto Rico. *Catena, 104*, 39-57. doi:10.1016/j.catena.2012.10.018

Gibson, S., Brunner, G., Piper, S., & Jensen, M. (2006). Sediment Transport Computations with HEC-RAS. Retrieved 2020, from https://pubs.usgs.gov/misc/FISC_1947-2006/pdf/1st-7thFISCs-CD/8thFISC/Session%203A-1_Gibson.pdf

Glysson, G.D. (1987), Sediment transport curves: U.S. Geological Survey Open-File Report 87–218, 53 p.

Gomi, T., Moore, R. D., & Hassan, M. A. (2005). Suspended Sediment Dynamics In Small Forest Streams Of The Pacific Northwest. *Journal of the American Water Resources Association, 41*(4), 877-898. doi:10.1111/j.1752-1688.2005.tb03775.x

Goodale, C. L., Thomas, S. A., Fredriksen, G., Elliott, E. M., Flinn, K. M., Butler, T. J., & Walter, M. T. (2009). Unusual seasonal patterns and inferred processes of nitrogen retention in forested headwaters of the Upper Susquehanna River. Biogeochem.,

Graham, J. L., Dubrovsky, N. M., & Eberts, S. M. (2017, December). Cyanobacterial Harmful Algal Blooms and U.S. Geological Survey Science Capabilities.

Gudino-Elizondo, N., Biggs, T. W., Castillo, C., Bingner, R. L., Langendoen, E. J., Taniguchi, K. T., . . . Liden, D. (2018). Measuring ephemeral gully erosion rates and topographical thresholds in an urban watershed using unmanned aerial systems and structure from motion photogrammetric techniques. *Land Degradation & Development, 29*(6), 1896-1905. doi:10.1002/ldr.2976

Hoover, D. J., and F. T. Mackenzie (2009), Fluvial fluxes of water, suspended particulate matter, and nutrients and potential impacts on tropical coastal water biogeochemistry: Oahu, Hawai'i, Aquat. Geochem., 15(4), 547–570, doi:10.1007/s10498-009-9067-2.

Hudson, P. F. (2003). Event sequence and sediment exhaustion in the lower Panuco Basin, Mexico. *Catena, 52*(1), 57-76. doi:10.1016/s0341-8162(02)00145-5

Inamdar, S., Dhillon, G., Singh, S., Parr, T., & Qin, Z. (2015). Particulate nitrogen exports in stream runoff exceed dissolved nitrogen forms during large tropical storms in a temperate, headwater, forested watershed. *Journal of Geophysical Research: Biogeosciences, 120*(8), 1548-1566. doi:10.1002/2015jg002909

Jastram, J. D., Zipper, C. E., Zelazny, L. W., & Hyer, K. E. (2010). Increasing Precision of Turbidity-Based Suspended Sediment Concentration and Load Estimates. *Journal of Environmental Quality, 39*(4), 1306-1316. doi:10.2134/jeq2009.0280

Jensen, A. K., & Ford, W. I. (2019). Quantifying Nitrate Dynamics of a Confluence Floodplain Wetland in a Disturbed Appalachian Watershed: High-Resolution Sensing and Modeling. *Transactions of the ASABE, 62*(6), 1545-1565. doi:10.13031/trans.13278

Johnston, C. A. (1991). Sediment and nutrient retention by freshwater wetlands: Effects on surface water quality. *Critical Reviews in Environmental Control, 21*(5-6), 491-565. doi:10.1080/10643389109388425

Jones, C. N., Scott, D. T., Edwards, B. L., & Keim, R. F. (2014). Perirheic mixing and biogeochemical processing in flow-through and backwater floodplain wetlands. *Water Resources Research, 50*(9), 7394-7405. doi:10.1002/2014wr015647

Junk, W. J., P. B. Balyley, and R. E. Sparks (1989), The flood pulse concept in river-floodplain systems, in Proceedings of the International Large River Symposium, Can. Spec. Publ. Fish. Aquat. Sci., 106, edited by D. P. Dodge, pp. 110–127.

Kitchens, C. M., Johengen, T. H., & Davis, T. W. (2018). Establishing spatial and temporal patterns in Microcystis sediment seed stock viability and their relationship to subsequent bloom development in Western Lake Erie. *Plos One, 13*(11). doi:10.1371/journal.pone.0206821

Knighton, A.D. (1980): Longitudinal changes in size and sorting of stream-bed material in four English rivers. Bulletin Geological Society America 91, 55-62. 1982: Longitudinal changes in the size and shape of stream bed material: evidence of variable transport conditions. Catena 9, 25-34.

Langlois, J. L., Johnson, D. W., & Mehuys, G. R. (2005). Suspended sediment dynamics associated with snowmelt runoff in a small mountain stream of Lake Tahoe (Nevada). *Hydrological Processes, 19*(18), 3569-3580. doi:10.1002/hyp.5844

Lauer, J. W., & Parker, G. (2008). Modeling framework for sediment deposition, storage, and evacuation in the floodplain of a meandering river: Theory. *Water Resources Research, 44*(4). doi:10.1029/2006wr005528

Lawler, D., Petts, G., Foster, I., & Harper, S. (2006). Turbidity dynamics during spring storm events in an urban headwater river system: The Upper Tame, West Midlands, UK. *Science of The Total Environment, 360*(1-3), 109-126. doi:10.1016/j.scitotenv.2005.08.032

Leite Ribeiro, M., Blanckaert, K., Roy, A.G., Schleiss, A.J. (2012). Flow and sediment dynamics in channel confluences. J. Geophys. Res. 117:F01035.

Lepesqueur, J., Hostache, R., Martínez-Carreras, N., Montargès-Pelletier, E., & Hissler, C. (2019). Sediment transport modelling in riverine environments: On the importance of grain-size distribution, sediment density, and suspended sediment concentrations at the upstream boundary. *Hydrology and Earth System Sciences, 23*(9), 3901-3915. doi:10.5194/hess-23-3901-2019

Levy, S. (2017). Microcystis Rising: Why Phosphorus Reduction Isn't Enough to Stop CyanoHABs. *Environmental Health Perspectives, 125*(2). doi:10.1289/ehp.125-a34

Lewis, J., & Eads, R. (2009, March). Implementation Guide for Turbidity Threshold Sampling: Principles, Procedures, and Analysis. Retrieved 2020, from https://www.fs.fed.us/psw/publications/4351/Lewis2009.pdf

Lewis, W. M., Wurtsbaugh, W. A., & Paerl, H. W. (2011). Rationale for Control of Anthropogenic Nitrogen and Phosphorus to Reduce Eutrophication of Inland Waters. *Environmental Science & Technology, 45*(24), 10300-10305. doi:10.1021/es202401p

Lloret, E., C. Dessert, L. Pastor, E. Lajeunesse, O. Crispi, J. Gaillardet, and M. F. Benedetti (2013), Dynamic of particulate and dissolved organic carbon in small volcanic mountainous tropical watersheds, Chem. Geol., 351, 229–244, doi:10.1016/j.chemgeo.2013.05.023.

Lloyd, C., Freer, J., Johnes, P., & Collins, A. (2016). Using hysteresis analysis of high-resolution water quality monitoring data, including uncertainty, to infer controls on nutrient and sediment transfer in catchments. *Science of The Total Environment, 543*, 388-404. doi:10.1016/j.scitotenv.2015.11.028

Lloyd, C. E., Freer, J., Johnes, P. J., & Collins, A. L. (2016). Technical Note: Testing an improved index for analysing storm discharge–concentration hysteresis. *Hydrology and Earth System Sciences, 20*(2), 625-632. doi:10.5194/hess-20-625-2016

Marren, P.M., Grove, J.R., Webb, J.A., Stewardson, M.J. (2014). The potential for dams to impact lowland meandering river floodplain geomorphology. The Scientific World Journal. 309673.

Martínez-Carreras, N., Schwab, M. P., Klaus, J., & Hissler, C. (2016). In situand high frequency monitoring of suspended sediment properties using a spectrophotometric sensor. *Hydrological Processes, 30*(19), 3533-3540. doi:10.1002/hyp.10858

Meade, R., Parker, R. (1985). Sediments in Rivers of the United States.

Megnounif, A., Terfous, A., & Ouillon, S. (2013). A graphical method to study suspended sediment dynamics during flood events in the Wadi Sebdou, NW Algeria (1973–2004). *Journal of Hydrology, 497*, 24-36. doi:10.1016/j.jhydrol.2013.05.029

Mertes, L. A. K. (1997), Documentation and significance of the perirheic zone on inundated floodplains, Water Resour. Res., 33, 1749–1762. Mielke, P. W., and K. J. Berry (2001), Permutation Methods: A Distance Function Approach, Springer, N. Y. Misiti, T. M., M. G. Hajaya, and S. G. Pavlostathis (2011), Nitrate reduction in a simulated free-water surface wetland system, Water Res., 45(17), 5587–5598.

Miller, J. P. (1958), High mountain streams: Effects of geology on channel characteristics and bed material, Mem. N. M. Bur. Mines Miner. Resour., 4.

Mitsch, W. J., Day, J. W., Gilliam, J. W., Groffman, P. M., Hey, D. L., Randall, G. W., & Wang, N. (2001). Reducing Nitrogen Loading to the Gulf of Mexico from the Mississippi River Basin: Strategies to Counter a Persistent Ecological Problem. *BioScience, 51*(5), 373. doi:10.1641/0006-3568(2001)051[0373:rnlttg]2.0.co;2

Mitsch, W. J., Dorage, C. L., & Wiemhoff, J. R. (1979). Ecosystem Dynamics and a Phosphorus Budget of an Alluvial Cypress Swamp in Southern Illinois. *Ecology, 60*(6), 1116. doi:10.2307/1936959

Moody, C., Worrall, F., Evans, C., & Jones, T. (2013). The rate of loss of dissolved organic carbon (DOC) through a catchment. *Journal of Hydrology, 492*, 139-150. doi:10.1016/j.jhydrol.2013.03.016

Morgan, B., Rate, A. W., & Burton, E. D. (2012). Water chemistry and nutrient release during the resuspension of FeS-rich sediments in a eutrophic estuarine system. *Science of The Total Environment, 432*, 47-56. doi:10.1016/j.scitotenv.2012.05.065

Moriasi, D. N., Gitau, M. W., & Daggupati, P. (2015). Hydrologic and Water Quality Models: Performance Measures and Evaluation Criteria. *Transactions of the ASABE, 58*(6), 1763-1785. doi:10.13031/trans.58.10715

Mosley, M. P. (1976), An experimental study of channel confluences, J. Geol., 84, 535 – 562.

NCASI Technical Bulletin No. 291, March 1977. National Council of the Paper Industry for Air and Stream Improvement, Inc., 260 Madison Ave., NY.

NOAA, & US Department of Commerce. (2014, August 01). Why do harmful algal blooms occur? Retrieved from https://oceanservice.noaa.gov/facts/why_habs.html

Noe, G. B., & Hupp, C. R. (2009). Retention of Riverine Sediment and Nutrient Loads by Coastal Plain Floodplains. *Ecosystems, 12*(5), 728-746. doi:10.1007/s10021-009-9253-5

Olde Venterink, H., Vermaat, J. E., Pronk, M., Wiegman, F., Lee, G. E., Hoorn, M. W., …Verhoeven, J. T. (2006). Importance of sediment deposition and denitrification for nutrient retention in floodplain wetlands. *Applied Vegetation Science, 9*(2), 163-174. doi:10.1111/j.1654-109x.2006.tb00665.x

Omernik, J. M. (1987). Ecoregions of the Conterminous United States. *Annals of the Association of American Geographers, 77*(1), 118-125. doi:10.1111/j.1467-8306.1987.tb00149.x

Paerl, H. W., & Huisman, J. (2008). CLIMATE: Blooms Like It Hot. *Science, 320*(5872), 57-58. doi:10.1126/science.1155398

Paerl, H. W., Scott, J. T., Mccarthy, M. J., Newell, S. E., Gardner, W. S., Havens, K. E., . . . Wurtsbaugh, W. A. (2016). It Takes Two to Tango: When and Where Dual Nutrient (N & P) Reductions Are Needed to Protect Lakes and Downstream Ecosystems. *Environmental Science & Technology, 50*(20), 10805-10813. doi:10.1021/acs.est.6b02575

Paustian, S.J. and R.L. Beschta. (1979). The Suspended Sediment Regime of a Oregon Coast Range Stream. Water Resources Bulletin 15:144-154.

Peterson, B. J. (2001). Control of Nitrogen Export from Watersheds by Headwater Streams. *Science, 292*(5514), 86-90. doi:10.1126/science.1056874

Phillips, J. M., Russell, M. A., & Walling, D. E. (2000). Time-integrated sampling of fluvial suspended sediment: A simple methodology for small catchments. *Hydrological Processes, 14*(14), 2589-2602. doi:10.1002/1099-1085(20001015)14:143.0.co;2-d

Probst, J. L., & Suchet, P. A. (1992). Fluvial suspended sediment transport and mechanical erosionin the Maghreb (North Africa). *Hydrological Sciences Journal, 37*(6), 621-637. doi:10.1080/02626669209492628

Rasmussen, P. P., Gray, J. R., Glysson, D., & Ziegler, A. C. (2009). Guidelines and Procedures for Computing Time-Series Suspended-Sediment Concentrations and Loads from In-Stream Turbidity-Sensor and Streamflow Data. Retrieved 2020, from https://pubs.usgs.gov/tm/tm3c4/pdf/TM3C4.pdf

Rivenbark, B. L., & Jackson, C. R. (2004). Concentrated Flow Breakthroughs Moving Through Silvicultural Streamside Management Zones: Southeastern Piedmont, Usa. *Journal of the American Water Resources Association, 40*(4), 1043-1052. doi:10.1111/j.1752-1688.2004.tb01065.x

Roberts, R. G., & Church, M. (1986). The sediment budget in severely disturbed watersheds, Queen Charlotte Ranges, British Columbia. *Canadian Journal of Forest Research, 16*(5), 1092-1106. doi:10.1139/x86-189

Rovira, A., Batalla, R.J. (2006). Temporal distribution of suspended sediment transport in a Mediterranean basin: the lower Tordera (NE Spain). Geomorphology 79 (1–2), 58–71.

Russo, J., & Fox, J. (2012). The role of the surface fine-grained laminae in low-gradient streams: A model approach. *Geomorphology, 171-172,* 127-138. doi:10.1016/j.geomorph.2012.05.012

Schilling, K. E., Isenhart, T. M., Palmer, J. A., Wolter, C. F., & Spooner, J. (2011). Impacts of Land-Cover Change on Suspended Sediment Transport in Two Agricultural Watersheds1. *JAWRA Journal of the American Water Resources Association, 47*(4), 672-686. doi:10.1111/j.1752-1688.2011.00533.x

Sidle, R.C. and A.J. Campbell. (1985). Patterns of Suspended Sediment Transport in a Coastal Alaskan Stream. Water Resources Bulletin 21:909-917.

Smith, V. (2003). Eutrophication of freshwater and coastal marine ecosystems a global problem. *Environmental Science and Pollution Research, 10*(2), 126-139.

Snyder, L., Potter, J. D., & Mcdowell, W. H. (2018). An Evaluation of Nitrate, fDOM, and Turbidity Sensors in New Hampshire Streams. *Water Resources Research, 54*(3), 2466-2479. doi:10.1002/2017wr020678

Taylor, P. G., W. R. Wieder, S. R. Weintraub, S. Cohen, C. C. Cleveland, and A. R. Townsend (2015), Organic forms dominate hydrologic nitrogen export from a lowland tropical watershed, Ecology, 96(5), 1229–1241, doi:10.1890/13-1418.1.

Tockner, K., D. Pennetzdorfer, N. Reiner, F. Schiemer, and J. V. Ward (1999), Hydrological connectivity, and the exchange of organic matter and nutrients in a dynamic river-floodplain system (Danube, Austria), Freshwater Biol., 41(3), 521–535

Trimble, S. W. (1997). Contribution of Stream Channel Erosion to Sediment Yield from an Urbanizing Watershed. *Science, 278*(5342), 1442-1444. doi:10.1126/science.278.5342.1442

Vaughan, M. C., Bowden, W. B., Shanley, J. B., Vermilyea, A., Sleeper, R., Gold, A. J., . . . Schroth, A. W. (2017). High-frequency dissolved organic carbon and nitrate measurements reveal differences in storm hysteresis and loading in relation to land cover and seasonality. *Water Resources Research, 53*(7), 5345-5363. doi:10.1002/2017wr020491

Vought, L.B.M., Dahl, J., Lauge Pedersen, C. & Lacousibre, J.O. (1994). Nutrient retention in riparian ecotones. Ambio 23: 342-348.

Walling, D.E., Webb, B.W. (1981). The reliability of suspended load data. Erosion and Sediment Transport Measurement, vol. 133. IAHS Publication, pp. 177–194.

Walling, D.E., Webb, B.W. (1982). Sediment Availability and Prediction of Stormperiod Sediment Yields, vol. 137. IAHS Publication, pp. 327–337.

Walling, D.E., Webb, B.W. (1987). Suspended load in gravel-bed rivers: UK experience. In: Thorne, C.R., Bathurst, J.C., Hey, D.L. (Eds.), Sediment Transport in Gravel-bed Rivers. Wiley, pp. 691–732.

Walsby, A. E., Hayes, P. K., Boje, R., & Stal, L. J. (1997). The selective advantage of buoyancy provided by gas vesicles for planktonic cyanobacteria in the Baltic Sea. *New Phytologist, 136*(3), 407-417. doi:10.1046/j.1469-8137.1997.00754.x

Ward, S. M. (1984, July). Suspended-Sediment Yields in the Taylor Run and Shavers Fork Basins, Randolph County, West Virginia, 1973-80. Retrieved 2020, from https://pubs.usgs.gov/wri/1983/4040/report.pdf

Whigham, D. F., Chitterling, C., & Palmer, B. (1988). Impacts of freshwater wetlands on water quality: A landscape perspective. *Environmental Management, 12*(5), 663-671. doi:10.1007/bf01867544

Wiegner, T. N., R. L. Tubal, and R. A. MacKenzie (2009), Bioavailability and export of dissolved organic matter from a tropical river during baseand stormflow conditions, Limnol. Oceanogr., 54(4), 1233–1242, doi:10.4319/lo.2009.54.4.1233.

Williams, G. P. (1989). Sediment concentration versus water discharge during single hydrologic events in rivers. *Journal of Hydrology, 111*(1-4), 89-106. doi:10.1016/0022-1694(89)90254-0

Williams, K. F., & Reed, L. A. (1972). Appraisal of Stream Sedimentation in the Susquehanna River ... Retrieved July, 2020, from https://pubs.usgs.gov/wsp/1532f/report.pdf

Wilson, G. V., Wells, R., Kuhnle, R., Fox, G., & Nieber, J. (2017). Sediment detachment and transport processes associated with internal erosion of soil pipes. *Earth Surface Processes and Landforms, 43*(1), 45-63. doi:10.1002/esp.4147

Wolman, M. G. (1967). A Cycle of Sedimentation and Erosion in Urban River Channels. *Geografiska Annaler. Series A, Physical Geography, 49*(2/4), 385. doi:10.2307/520904

World Health Organization; 2003; Cyanobacterial Toxins: Microcystin-LR in Drinking Water; Cyanobacterial Toxins: Microcystin-LR in Drinking Water; WHO/SDE/WSH/03.04/57. World Health Organization, Geneva, Switzerland.

Wymore, A. S., Leon, M. C., Shanley, J. B., & Mcdowell, W. H. (2019). Hysteretic Response of Solutes and Turbidity at the Event Scale Across Forested Tropical Montane Watersheds. *Frontiers in Earth Science, 7*. doi:10.3389/feart.2019.00126

VITA

Ciara Pickering was raised in Carmel, Indiana. She has a B.S. from the University of Kentucky from the University of Kentucky in Biosystems and Agricultural Engineering. She continued her education in this department and worked as a Graduate Research Assistant. She was very involved in professional development societies such as the UK ASABE student branch, Society of Women Engineers, and the Alpha Epsilon Honors Society for Agricultural and Biological Engineers. During her graduate tenure, she gave poster and oral presentations at the Kentucky Water Resources Research Institute's (KWRRI) Annual Symposium and the American Society of Agricultural and Biological Engineers' (ASABE) Annual International Meeting respectively. She received the Most Outstanding Graduate Poster Presentation Award for her presentation at the annual KWRRI Symposium and she also received the Most Outstanding M.S. Student departmental award.